Stretchable Strain Sensors Based on Conductive Microspheres

Zur Erlangung des akademischen Grades einer

Doktorin der Ingenieurwissenschaften (Dr.-Ing.)

von der KIT-Fakultät für
Elektrotechnik und Informationstechnik
des Karlsruher Instituts für Technologie (KIT)

angenommene

Dissertation

von

M.Sc. Pariya Nazari
geb. in Tehran

Tag der mündlichen Prüfung: 11.07.2024

Hauptreferent: **Prof. Dr. Uli Lemmer**

Korreferentin: **Prof. Dr. Jasmin Aghassi-Hagmann**

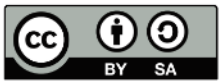

Abstract

Wearable electronics, human-machine interfacing, and soft robotics are among the diverse future applications that will benefit from the development of high-precision stretchable strain sensors. Specifically offering mechanical conformability while allowing for additive manufacturing methods and a high sensing surface make the stretchable strain sensors a complementary technology to the state-of-the-art rigid silicon-based sensors. The stretchable strain sensors owe their deformability to the presence of an elastomer in their structure, a key element that acts as a double-edged sword. As the main advantage, the elastomer allows for conductive network deformation reversibly in ranges unavailable to conventional silicon-based MEMS sensors. However, an unbalance in the elastomer chain mobility and strain distribution in the conductive network engenders electromechanical hysteretic effects hindering the smooth lab-to-fab transition. Moreover, the conductive element's geometry and its interface with the elastomer have proven to be crucial factors in determining the key sensor performance metrics.

In this context, over a decade numerous studies into improving the performance of stretchable strain sensors through novel sensing material and structure engineering have led to constant advancement of sensor concepts. Notwithstanding the body of works, to extend either the stretchability or the sensitivity of the sensor the majority of the reports have focused on incorporating a second conductive or insulating material in between the main sensing elements. To increase the mechanical robustness of the sensor, encapsulating the active sensing material into a second elastomer has been a path commonly taken. Both of these approaches sacrifice the simplicity and cost-effectiveness of the fabrication processes. While high stretchability and mechanical robustness are important performance characteristics, ultimately the application-specific requirements determine the key areas in need of modification. For example except for human-motion detection, an application area that has received extensive attention in recent years, in most smart sensing applications, apart from high reproducibility, small strain sensing with high resolution has a higher priority.

To this end, the primary contribution of this work is extending the limits of sensing by embedding unconventional conductive microspheres into the matrix of an underexplored elastomer, EVA. Employing additive manufacturing techniques such as stencil printing and wet-spinning in this work offers economically viable options with customized fabrication possibilities and low material waste. At the outset, structural studies on both printed and wet-

spun sensors reveal the decisive role of the elastomer type and its interface with conductive microspheres. Although the 35 µm microspheres provide a lower detection limit and a higher sensitivity compared to the 4 µm microspheres, the sensor's stretchability is limited especially due to the onset of electromechanical hysteresis under repetitive cycles. This highlights the importance of particle size on the sensing limit and the sensitivity. Further, using 4 µm microspheres the performance of the printed sensor exhibits promising characteristics such as high reproducibility. Based on the 4 µm microspheres, the printed sensors are then investigated for impact sensing and diaphragm expansion monitoring wherein mechanical durability to overload strain and high sensitivity are demonstrated. In hindsight, one limiting factor for extending the minimum detection limit and resolution is identified as the presence of the stretchable substrate with a higher elastic modulus compared to the composite. This underlines the importance of the mechanical compatibility of the substrate with the elastomer. Therefore, the subsequent part of this work focuses on developing a substrate-free sensor based on the same composite (4 µm microspheres and EVA). This approach yields a record low detection limit and resolution and a fast response time (16 < ms), characteristics particularly attractive for small strain sensing applications. Last but not least, this study led to the first demonstration of employing a piezoresistive stretchable strain sensor for real-time battery expansion monitoring.

Kurzfassung

Tragbare Elektronik, Mensch-Maschine-Schnittstellen und Soft-Robotik gehören zu den vielfältigen zukünftigen Anwendungen, die von der Entwicklung hochpräziser dehnbarer Dehnungssensoren profitieren werden. Insbesondere die mechanische Anpassungsfähigkeit, die additiven Fertigungsmethoden und die große Sensorfläche machen die dehnbaren Dehnungssensoren zu einer komplementären Technologie zu den modernen Sensoren auf Siliziumbasis. Die dehnbaren Dehnungssensoren erhalten ihre Verformbarkeit durch das vorhandene Elastomer in ihrer Struktur, ein Schlüsselelement, das wie ein zweischneidiges Schwert wirkt. Der Hauptvorteil besteht darin, dass das Elastomer eine reversible Verformung des leitfähigen Netzwerks in Bereichen ermöglicht, die für herkömmliche MEMS-Sensoren auf Siliziumbasis nicht zugänglich sind. Ein Ungleichgewicht in der Beweglichkeit der Elastomerkette und der Spannungsverteilung im leitfähigen Netzwerk führt jedoch zu elektromechanischen hysteretischen Effekten, die einen reibungslosen Übergang vom Labor zur Fertigung verhindern. Darüber hinaus haben sich die Geometrie des leitenden Elements und seine Schnittstelle mit dem Elastomer als entscheidende Faktoren für die Bestimmung der wichtigsten Leistungskennzahlen des Sensors erwiesen.

In diesem Zusammenhang haben über ein Jahrzehnt hinweg zahlreiche Studien zur Verbesserung der Leistung von dehnbaren Dehnungssensoren durch neuartige Sensormaterialien und Strukturtechniken zu einer ständigen Weiterentwicklung der Sensorkonzepte geführt. Trotz der zahlreichen Veröffentlichungen konzentrierten sich die meisten Berichte darauf, ein zweites leitfähiges oder isolierendes Material zwischen den Haupterfassungselementen einzubauen, um entweder die Dehnbarkeit oder die Empfindlichkeit des Sensors zu erhöhen. Um die mechanische Robustheit des Sensors zu erhöhen, wird häufig das aktive Sensormaterial in ein zweites Elastomer eingekapselt. Beide Ansätze gehen zu Lasten der Einfachheit und Kosteneffizienz der Herstellungsprozesse. Hohe Dehnbarkeit und mechanische Robustheit sind zwar wichtige Leistungsmerkmale, doch letztlich bestimmen die anwendungsspezifischen Anforderungen die Schlüsselbereiche, die einer Modifizierung bedürfen. Abgesehen von der Erkennung menschlicher Bewegungen, einem Anwendungsbereich, dem in den letzten Jahren große Aufmerksamkeit geschenkt wurde, hat bei den meisten intelligenten Sensoranwendungen neben einer hohen Reproduzierbarkeit die Erkennung kleiner Dehnungen mit hoher Auflösung eine höhere Priorität.

Der Hauptbeitrag dieser Arbeit besteht darin, die Grenzen der Sensorik zu erweitern, indem unkonventionelle leitfähige Mikrokugeln in die Matrix eines bisher wenig erforschten Elastomers, EVA, eingebettet werden. Der Einsatz von additiven Fertigungstechniken wie dem Schablonendruck und dem Nassspinnen in dieser Arbeit bietet wirtschaftlich tragfähige Optionen mit angepassten Fertigungsmöglichkeiten und geringem Materialabfall. Strukturelle Untersuchungen sowohl an gedruckten als auch an nassgesponnenen Sensoren zeigen zunächst die entscheidende Rolle des Elastomertyps und seiner Schnittstelle zu leitfähigen Mikrokugeln. Obwohl die 35-µm-Mikrokugeln im Vergleich zu den 4-µm-Mikrokugeln eine niedrigere Nachweisgrenze und eine höhere Empfindlichkeit bieten, ist die Dehnbarkeit des Sensors insbesondere durch das Auftreten einer elektromechanischen Hysterese bei wiederholten Zyklen begrenzt. Dies unterstreicht die Bedeutung der Partikelgröße für die Nachweisgrenze und die Empfindlichkeit. Darüber hinaus weist der gedruckte Sensor bei Verwendung von 4 µm großen Mikrokugeln vielversprechende Eigenschaften wie eine hohe Reproduzierbarkeit auf. Basierend auf den 4 µm-Mikrokugeln werden die gedruckten Sensoren dann für die Stoßerkennung und die Überwachung der Membranausdehnung untersucht, wobei die mechanische Beständigkeit gegenüber Überlastungen und die hohe Empfindlichkeit nachgewiesen werden. Rückblickend lässt sich feststellen, dass ein limitierender Faktor für die Erweiterung der Mindestdetektionsgrenze und der Auflösung das Vorliegen eines dehnbaren Substrats mit einem höheren Elastizitätsmodul im Vergleich zum Komposit ist. Dies unterstreicht die Bedeutung der mechanischen Kompatibilität des Substrats mit dem Elastomer. Daher konzentriert sich der folgende Teil dieser Arbeit auf die Entwicklung eines substratfreien Sensors auf der Grundlage desselben Komposits (4 µm Mikrokugeln und EVA). Nicht zuletzt führte diese Studie zur ersten Demonstration des Einsatzes eines piezoresistiven dehnbaren Dehnungssensors für die Echtzeitüberwachung der Batterieausdehnung. Dieser Ansatz ermöglicht eine Rekord niedrige Detektionsgrenze und Auflösung sowie eine schnelle Antwortzeit (16 < ms), Eigenschaften, die für kleine Dehnungssensoranwendungen besonders attraktiv sind.

Contents

List of Publications and Contributions to Conferences

Publications in Peer-reviewed Journals

- **P. Nazari**, J. Zimmermann, C. Melzer, W. Kowalsky, J. Aghassi-Hagmann, G. Hernandez-Sosa, and U. Lemmer. *High-Resolution Printed Ethylene Vinyl Acetate Based Strain Sensor for Impact Sensing*. *Adv. Sens. Res. 2024, n/a, 2300189.*

- **P. Nazari**, R. Bäuerle, J. Zimmermann, C. Melzer, C. Schwab, A. Smith, W. Kowalsky, J. Aghassi-Hagmann, G. Hernandez-Sosa, and U. Lemmer. *Piezoresistive Free-standing Microfiber Strain Sensor for High-resolution Battery Thickness Monitoring. Adv. Mater. 2023, 35, 2212189.*

- R. Bäuerle, **P. Nazari**, J. Zimmermann, C. Melzer, G. Hernandez-Sosa, and W. Kowalsky. *Fully printed PTC based heat transfer sensor array as liquid level sensor. 2023, Adv. Sens. Res. 2024.*

Conference Contributions

- P. Nazari, P. Gupta, R. Bäuerle, C. Willig, J. Zimmerman, C. Melzer, W. Kowalsky, G. Hernandes-Sosa, J. Aghassi-Hagmann, U. Bunz, U. Lemmer. *Ethylene-Vinyl Acetate - a Promising Alternative to Polydimethylsiloxane for Stretchable Electronics.* Virtual MRS Spring Meeting 2022, Oral Presentation.

- P. Nazari, J. Zimmermann, C. Melzer, P. Gupta, R. Bäuerle, U. Bunz, W. Kowalsky, G. Hernandez-Sosa, J. Aghassi-Hagmann, and U. Lemmer. *Filamented Network Assembly by Electric Field Induced Percolation for Highly Sensitive Directional Strain Sensing.* SPIE Optics and Optoelectronics 2022, San Diego, CA, USA, Poster Presentation.

- P. Nazari, R. Bäuerle, W. Kowalsky, J. Aghassi-Hagmann, G. Hernandez-Sosa, and U. Lemmer. *Wet-spun microfiber strain sensor for high-resolution strain sensing*. SPIE Optics and Optoelectronics 2023, San Diego, CA, USA, Oral and Poster Presentation.

- P. Nazari, R. Bäuerle, W. Kowalsky, J. Aghassi-Hagmann, G. Hernandez-Sosa, U. Lemmer. *Stretchable Strain Sensor for Li-ion Battery Expansion Monitoring.* EMRS Fall Meeting 2023, Warsaw, Poland, Oral Presentation.

Abbreviations

35MS	35 µm microspheres
35MS-EVA	EVA and 35 µm microspheres
35MS-PDMS	PDMS and 35 µm microspheres
4MS	4 µm microspheres
DC	direct-current
DEP	dielectrophoretic force
EOF	electroosmosis flow
EHD	electrohydrodynamic flow
EP	electrophoretic force
EVA	ethylene vinyl acetate
IoT	Internet of Things
Li-ion	lithium-ion
MEMS	microelectromechanical system
NMC	$LiNi_{1/3}Mn_{1/3}Co_{1/3}O_2$
OM	optical microscope
PDMS	polydimethylsiloxane
PET	polyethylene terephthalate
PMMA	poly(methyl methacrylate)
PU	polyurethane
SEM	scanning electron microscope
SMU	source-measure unit
SPC	stretchable polymer composites
$\Delta R/R_0$	relative change of resistance
vol.%	volume fraction percentage
wt.	weight

1. Introduction

"From the moment you're born to the moment you draw your last breath, your brain is stuck in a dark, silent box called your skull. Day in and day out, it continually receives sense data from the outside world via your eyes, ears, nose, and other sensory organs. This data does not arrive in the form of the meaningful sights, smells, sounds, and other sensations that most of us experience. It's just a barrage of light waves, chemicals, and changes in air pressure with no inherent significance. Face with these ambiguous scraps of sense data, your brain must somehow figure out what to do next."

Lisa Feldman Barrett

Seven And a Half Lessons About the Brain[1]

This excerpt by Lisa Feldman Barrett best describes the significance of sensing as a fundamental part of how our brain perceives ourselves and the world around us. By processing data from our sensory organs, the brain generates models and uses them to understand and interact with the environment. This research is about human-made sensors, driven by the core motivation of developing mechanical sensors with improved sensing capabilities, particularly in terms of resolution and cost-effectiveness. Introducing stretchable strain sensors featuring unconventionally large conductive microspheres, this work aims to push the boundaries of sensing limits prepared by scalable fabrication methods. This chapter outlines the motivations behind this research area, dives into the state-of-the-art, and provides an overview of the thesis structure.

1.1. Motivation

Sensors are an interface between the world we live in, which is neither digital nor electrical (except for the atomic-scale world), and the devices we continue to advance to make our lives easier. Sensors translate the external physical parameters of the environment into the internal electrical signals understandable by our devices.[2] Primarily based on microelectromechanical systems (MEMS) and complementary metal-oxide semiconductor technology, the smart sensor market size reached a value of over 45.4 billion USD in 2022 and is expected to growth with a compound annual grow rate of over 15% until 2032.[3] Modern MEMS sensors are ubiquitous as essential parts of highly integrated smart sensing technologies and excel in compactness. However, their manufacturing process is becoming increasingly complex, demanding intensive investment.[4] Additionally, they struggle when it comes to large-area and mechanical flexibility due to their miniature size and rigid nature. To address the limits of conventional rigid sensing, flexible sensors as innovative solutions have emerged introducing mechanical compliance that can respond to a wide variety of external inputs such as mechanical, chemical, and electromagnetic. More specifically, in addition to flexible sensors, stretchability has become under the spotlight, particularly when it comes to compatibility with soft and pliable applications tailored for interacting with humans.

Stretchable strain sensors are of outstanding importance for the realization of a wide variety of emerging smart applications such as soft robotics,[5] integrated e-Skins,[6–8] biomedical applications,[9–11] wearable electronics,[12,13] and the Internet of Things.[14] The growing interest in flexible and deformable strain sensors, besides reliable stretchability, calls for high resolution, high sensitivity, and cost-effective fabrication methods. In this regard, there have been numerous strategies on how to obtain compliance with complex shape-changing structures unavailable to conventional rigid sensors. The common form factors to achieve deformability without losing performance have been using novel structural approaches for example 3D mechanical buckling,[15,16] bridge-island wavy interconnects,[17,18] 2D or 3D serpentine or fractal structures,[19–22] and Origami and Kirigami designs.[23,24] However, these structures are made of rigid material which inherently suffer from the inevitable emergence of microcracks in the non-stretchable parts resulting in early mechanical failure and electrical disconnection. Hereof, fully stretchable conductive composites provide a

favorable solution based on a conductive part embedded into or on top of a stretchable substrate or fully stand-alone stretchable composite structures.

Despite tremendous efforts in laboratory research, the market reach of stretchable sensors is still restricted. Given the multitude of advantages offered by stretchable sensors, addressing the challenges to their widespread commercialization requires increased attention. There are several efforts made to address the bottlenecks of stretchable sensors by designing innovative materials and devices that are capable of performance levels similar to those of smart microsensors.[25] Inspired by these efforts, the core motivation of this thesis is to contribute to tackling some of the challenges of improving the sensing limits of stretchable composite strain sensors using additive manufacturing methods.

1.2. State of the Art and Problem Definition

In the realm of fully stretchable strain sensors, the mechanical compliance to deformation is commonly realized by using a stretchable elastomer as a housing matrix, that contains the conductive materials. When an input strain is applied to the stretchable polymer composites (SPC), the deformation elongates the elastic polymer. This yields a change in the conductive pathway, hence a change in the total resistance of the device is recorded as an output, that is piezoresistivity. In terms of fabrication techniques, additive manufacturing techniques such as printing allow for large-volume fabrication. Without the need for high temperature and high vacuum, thus being potentially low-cost with the least material waste these techniques are among the most promising approaches.[26] Either printing the active sensing layer on a stretchable substrate or additive manufacturing of a free-standing sensor offers several advantages and disadvantages. The choice between the two ultimately depends on the requirements of the target application. For example, utilizing the same composite of an elastomer and a conductive part, on the one hand, when printed on a substrate, mechanically supports the active layer increasing the durability of the sensor and avoiding damage during application. However, incorporating a substrate means additional material consumption and increased cost of fabrication. Moreover, special attention must be given to the elastomeric compatibility between the substrate and the composite. On the other hand, in the absence of a substrate, the composite has more range of flexibility and stretchability, a higher conformability to irregular and intricate surfaces, and a potentially enhanced sensitivity,

making this option a more versatile one. Nevertheless, the sensor might become more prone to overstretching damages during handling and application. Therefore, corresponding to the key requirements of the application, e.g. range of strain detection, minimum detection limit, and minimum resolution the sensing material is designed.[27]

The conductivity in SPC sensors is achieved by including conductive materials in the matrices of the elastic polymer, for example a conductive polymer,[28,29] liquid metal,[30–33] solid particles in nano or micron scale (e.g. carbon-black,[34–37] carbon nanotubes,[38–41] silver nanowires,[42–45] and graphene[46–48]) or a hybrid combination of different conductive material.[42,49–54] The predominantly used elastomers are polydimethylsiloxane (PDMS),[52,55–58] thermoplastic polyurethane,[38,59–61] or poly styrene-butadiene-styrene polymers[42,62–64]. The electromechanical properties of a composite sensor highly depend on the nature of the elastomers used (as matrix or substrate), the geometry of the conductive part, and the interface between the particle and the elastomer. PDMS is commonly chosen as the elastic polymer because of its high flexibility.[36,65–67] However, apart from being a costly polymer, there are several challenges in processing it such as the onset of cross-linking as the two parts are mixed. Therefore its use is not straightforward for large-scale additive manufacturing techniques.[68] Hence, in the first part of this work, as a promising alternative elastomer, the ethylene vinyl acetate copolymer with 40 wt.% vinyl acetate is compared with PDMS in terms of morphology and microstructure (for simplicity in this thesis hereon EVA refers to EVA with 40 wt.% vinyl acetate). EVA is an economic polymer that is not only used as an elastomer for stretchable sensors,[69–72] but also as an encapsulating material for photovoltaic modules[73–75] and food packaging[76].

There is an extensive amount of work on SPC sensors utilizing nanoparticles as conductive constituents.[34,35,44,45,54,77,78,36–43] However, their fabrication processes are complex and costly. Some examples involve several steps in the preparation of a printable solution, using hazardous chemicals, and the addition of extra material mainly to functionalize the nanoparticles avoiding their agglomerations during processing. The majority of stretchable sensors reported have focused on high stretchability.[38,43,59,77,79] Nevertheless, common smart applications involve small strain range inputs while low detection limit with high signal-to-noise-ratio as well as high resolution (distinguishing small strain changes) carry more weight.[25,26] There are numerous reports with a low limit of detection.[34,62,80–82] However, most smart applications demand reproducible detection of smaller strain values

with an elongation in the micrometer range (comparable to MEMS technology). Overall, there have been some efforts made to increase the sensitivity of the stretchable sensors mainly by introducing microstructures in the active material and by reducing the contact points between the conductive particles. However, these approaches are time-consuming and not cost-efficient as they involve either the addition of a second material for the microstructure or involve controlled introduction of micropatterns for example by photolithography.[27]

In this work, core-shell silver-coated glass microspheres are utilized as the conductive material to leverage the microstructure provided by the core-shell configuration. Achieving a high sensitivity to small composite elongation and straightforward preparation steps are also among the reasons behind the choice of microspheres. In terms of sensing performance, the focus of this work is on developing SPC strain sensors with the lowest detection limit and resolution with an easily detectable signal under various small strain inputs. Moreover, to keep the findings of this study relevant for the industry, we opt for fully additive manufacturing techniques for the fabrication of our sensors.

1.3. Structure of the Thesis

In this thesis, the development of high-precision SPC strain sensors based on conductive microspheres will be discussed that are prepared using scalable techniques and used in three applications. Following the introductory chapter, the scope of this thesis in the subsequent chapters is outlined as listed below:

- Chapter 2 provides the technical background of SPC strain sensors, explaining the working mechanism of piezoresistive strain sensors, and the key sensing properties are summarized, including mechanical considerations. Additionally, the forces involved in dynamic percolation using the direct electric field are introduced.

- Chapter 3 gives an overview of the experimental methods. It introduces the utilized material and explains the fabrication steps involved in the fabrication of the SPC strain sensors. Additionally, the characterization tools as well as prepared test setups for the applications are described in detail.

- Chapter 4 presents the development of a SPC strain sensor having EVA as the elastomer and printed on a stretchable substrate, in three different stages. The first part, using 35 µm conductive microspheres, focuses on comparing the morphology, microstructure, and performance of sensors prepared using PDMS with EVA. Based on the findings of this part, EVA as a promising alternative to PDMS is chosen for the extended electromechanical performance tests under various strain cycles. In the second part, using 4 µm conductive microspheres, the sensor's figures of merit are investigated. Finally, using a direct current electric field and a composite of EVA and 35 µm microspheres, the volume fraction of particles required for achieving conductivity is significantly decreased and studied in situ using optical microscopy.

- Chapter 5 deals with introducing and investigating the performance of a substrate-free stretchable sensor. Using an extrusion method and 4 µm conductive microspheres, a free-standing stretchable microfiber sensor is developed. The fabrication method is described in detail and mechanical figures of merit of the EVA-microfibers are compared with those of microsphere-containing microfibers.

- Chapter 6 presents three real-time strain sensing application examples where the developed strain sensors based on EVA and 4 µm microspheres are employed. The first application revolves around impact sensing using the printed sensor where outstanding resolution and very short response time are demonstrated. The second part explains how the printed sensor is used for monitoring the expansions of an inflating diaphragm where the sensor is subjected to overload strain instances. The scope of the third part is the thickness change monitoring of a Li-ion battery during charging and discharging, for the first time, using the piezoresistive microfiber developed in this work. The response of seven microfibers is compared with a commercially available displacement sensor, showing identical phases of battery expansion and contraction.

- Chapter 7 summarizes the key findings of this work and provides an outlook for future studies on improving the performance of the SPC strain sensors and their implementation in relevant applications.

2. Theoretical Background

This chapter explains the theoretical basis for understanding this work. First, the percolation theory is introduced, followed by covering the basics of piezoresistivity and tunneling effect as the main sensing mechanisms of SPC strain sensors. Then the Hildebrand-Hansen solubility parameters are explained as the underlying reasons behind the choice of solvents for the EVA. Based on the stress-strain diagram the mechanical characteristics of the SPC sensors are summarized. The main figures of merit then are described covering hysteresis in detail. The chapter concludes by introducing the forces acting on direct-current subjected filler-elastomer composites.

2.1. Percolation Theory

Conductivity and Resistivity

Resistivity is defined as a fundamental electrical property of a material, meaning the magnitude of its resistance to current flow, and is defined based on Equation 2.1. Conductivity or specific electrical conductance of a material is the reciprocal of Equation 2.1., and it determines the conducting ability of a material to the electrical current flow, *A* is the cross-section, and *l* is the length of the material.

$$\rho = \frac{1}{\sigma} = R\,\frac{A}{l} \tag{2.1}$$

The electrical characteristics of a material are generally defined by its response under an electric field. In metals, the applied electric field e.g. a constant and small voltage, causes the transport of electrical charges, conducting current through the metal. To obtain electrical conductivity in an insulating polymer, solid conductive particles of different types are

incorporated into the polymer.[83] These blends, depending on the density of conductive content obtain conductivity. Therefore, conductive SPCs provide the merits of polymers that are straightforward processing, lightweight, economical, and mechanical deformability. Within a composite of randomly dispersed conductive particles in an insulating elastomer, based on the percolation theory, there is a minimum ratio of conductive particles needed for a composite to undergo a transition from electrically disconnected to becoming conductive. When the conductivity of a composite filled with conductive particles is measured as a function of the volume fraction of fillers, as the ratio increases above a critical threshold, this transition is observed with an abrupt increase of conductivity, that is characterized by a sigmoidal behavior.[72] As schematically shown in Figure 2.1, the outset of conductivity is characterized by the dramatic increase, by several orders of magnitude, during a small change of conductive particle concentration.

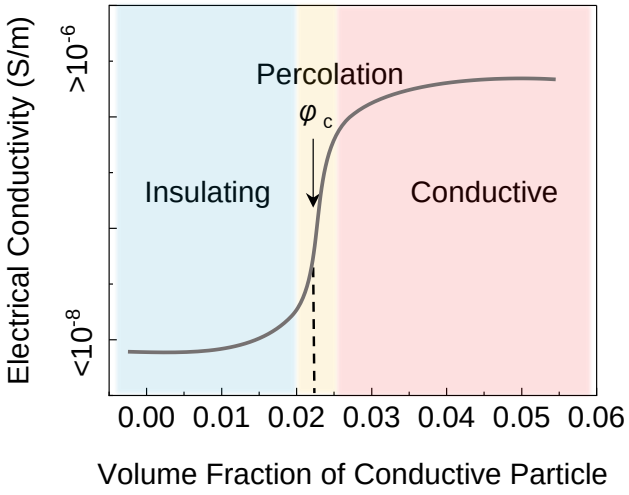

Figure 2.1. Electrical conductivity of a polymer-filler composite as a function of volume fraction of filler.

This phenomenon is explained by the formation of physically connected paths made of clusters of agglomerated conductive particles, hence the electrons can move from one electrode to the other passing and hoping through the formed interconnected network. At low-volume fractions, the mean particle or cluster distances are large enough to inhibit conductance. Close to the transition, the conductivity shows a non-linear behavior. In 1957 Hammersley and Broadbent introduced the percolation theory, in an attempt to model the fluid flow in a porous media. As a mathematical framework to describe this behavior, and to find the critical percolation threshold (φ_c) there are several models mentioned in the

literature. Close to the critical volume fraction, that is the percolation threshold, the percolation equation is described as a power-law as follows.

$$\sigma/\sigma_0 = (\varphi - \varphi_c)^t \quad (2.2)$$

where σ is the composite conductivity at a corresponding volume fraction, σ_0 is the conductivity of a thin film of the filler (comparable to the filler in the composite), φ is the filler volume ratio, and φ_c is the critical volume ratio or percolation threshold, and t is the percolation exponent indicating the power with which conductivity increases above the percolation.

2.2. Piezoresistivity

Piezoresistivity is one of the main transduction mechanisms involved in an SPC strain sensor in detecting a mechanical stimulus and converting it to an electrical signal.[84] It refers to the increase of resistance as a result of applied mechanical deformation, e.g. stretching. Due to the fundamental differences in the morphology and structural properties of the elastic polymer and the conductive particle (e.g. crystallinity, molecular polarity, surface energy), there is no general agreement for predicting the exact mechanism of piezoresistivity at a given composite. Generally, in a conductive SPC made of an insulating polymer and a conductive particle, mainly dependant on the volume ratio and the distribution of the particles within the polymer matrix, as the sensor is elongated, the piezoresistivity may originate from one or a combination of the following:

i) When the piezoresistive SPC is stretched, the overlap area between the connected particles reduces, and the interparticle distances increase. Due to the tunneling effect and the changes in the tunneling distance, as discussed in Section 2.4, the resistance of the sensor increases.

ii) Electrical disconnection in the network structure of the connected particles in the elastic matrix between the two electrodes (changes in the Ohmic contacts) causes an increase in resistance. The main reason behind the disconnection in the conductive network stems from the mismatch in the stiffness of the constituent elements of a stretchable sensor, that is a solid micro or nano filler embedded in a stretchable polymer. Therefore, when subjected to an elongation, the disconnection of the elastomer-particle bonds and particle-particle bonds leads to the disruption of conductive paths.

iii) The change in the geometry of the sensor that is a change in its length and cross-section area increases resistance.[12] According to Equation 2.1, any changes in l and A change the resistance of the composite. This effect will be discussed in the following sections.

2.3. Strain

When a tensile force is applied to a material, the strain as a non-dimensional parameter is defined as the deformation the material undergoes in the direction of the applied force divided by the initial dimension of the material. In other words, it is the normalized deformation of the material under normal stress. If the tensile force applied to the material is in the longitudinal direction, tensile strain, or from here on strain, denoted as ε is described by Equation 2.3, where L_0 is the initial length of the material in the direction of applied tensile force, and ΔL is the change in the length of the material in that direction.

$$\varepsilon = \frac{\Delta L}{L_0} \tag{2.3}$$

In the schematic illustrations in Figure 2.2 (not to scale), the basic mechanism behind the transduction of a mechanical deformation into an increase in electrical resistance in an SPC strain sensor is explained. The SPC composite based on an insulating elastomer and conductive particles sandwiched between the two electrodes has an initial length of L_0. As shown in Figure 2.2a, when a supply voltage is applied to the electrodes, electrical resistance of a contaced pair of particles is ohmic comprising the sum of the resistances of both particles. As the composite is subjected to a tensile force (Figure 2.2b) it elongates, resulting in a change in its length, ΔL. As long as the change in interparticle distances stays in the tunneling range (following section), a tunneling resistance is added to the resistance of the pair. If the applied strain is large enough resulting in a substantial change in the length of the composite, it may undergo complete electrical disconnection.

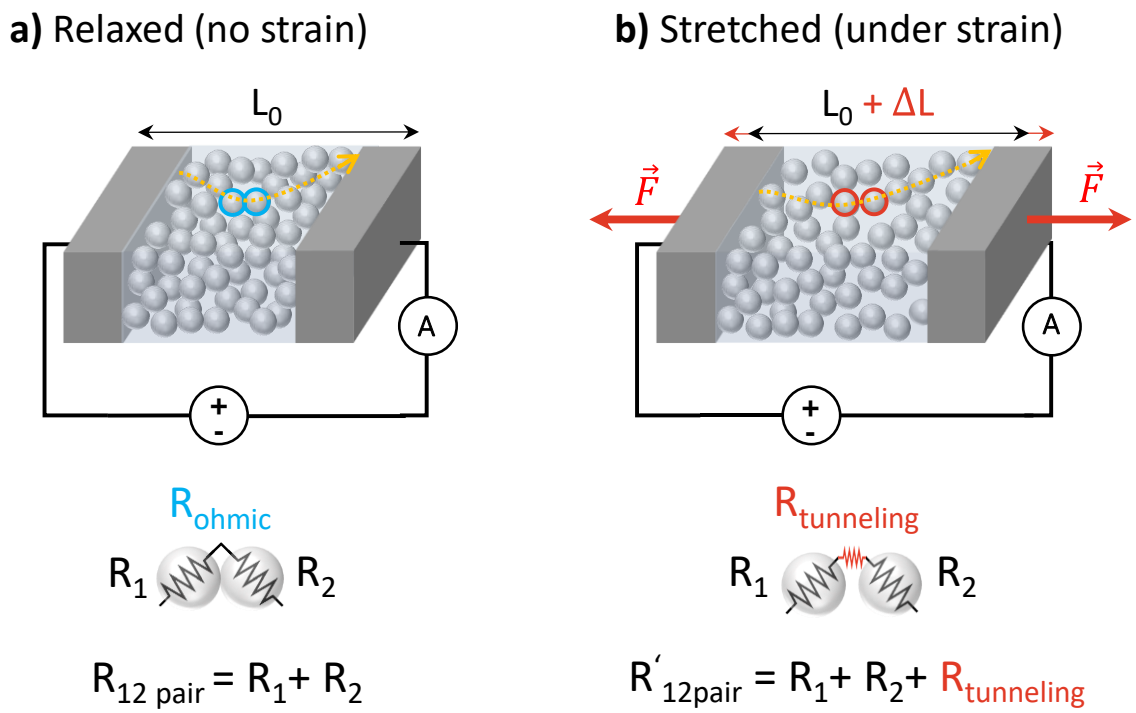

Figure 2.2. Schematic illustration of a percolated network of conductive particles embedded in an elastomer matrix and sandwiched between two electrodes. a) At a mechanically relaxed state, where no strain is applied to the SPC, contacts are mainly Ohmic (marked by blue circles). b) As a tensile force is applied in the longitudinal direction, causing elongation of the composite in the direction of the applied strain, either the overlapping area between particles or the interparticle distances change. Therefore, tunneling resistance comes into play.

2.4. Tunneling Effect

When a percolated composite of particle-elastomer is subjected to strain, it stretches increasing the total resistance of the composite, an effect called piezoresistivity. Provided that the elongation is small enough to keep the cross-sectional area and the length of the composite to almost the same values as before the stretching, the change of resistance due to geometrical changes is negligible. Therefore, the main mechanism behind the conduction in a stretched composite can be explained based on the change in the tunneling distance due to the decrease of the overlap area between the physically connected conductive particles, described as the tunneling effect.[85] Based on quantum mechanics, the tunneling effect refers to the electrons flowing through traverse potential barriers, that is in our composite the insulating polymer layer in between particles. If the thickness of the insulating polymer at the interface of the particles is thin enough, that is comparable to the de Broglie wavelength of the electron (λ_{db}) it exhibits wave-like behavior, passing through the insulating barrier.

Thus, conducting current through the insulating barrier between the conductive particles, where the particles act as an electrode with an opposite charge. In our case, we apply a 50 mV source voltage to the two electrodes of the sensor and measure the resistance in a two-probe setting, while the sensor is static and being stretched. The resistance change, as the response of the sensor to the applied strain, is recorded during strain tests. In this case, the de Broglie wavelength of an electron is estimated to be 5.5 nm ($\lambda_{db} = h/p = 1.227 / V^{1/2}$ nm, where h is the Planck's constant, p is the momentum of the electron, and V is the voltage applied at the two electrodes). The minimum junction distance through which electrons can pass via quantum tunneling is called the cut-off distance and depends on the type of conductive material, the insulating polymer, and the processing parameters.[12,85] Thus, overall conduction is made not only through physically connected particles but also via tunneling between adjacent particles, provided that the interparticle distances are within the cut-off distance.

In the following, the predominant electrical response mechanism of our composite, that is through the tunneling effect, is explained and the total resistance between the electrodes, R_t, and its change during the stretching tests are estimated.[12,85] In a composite based on an insulating polymer and conductive particles, the total resistance depends on the resistance of the conductive particle and the polymer. The insulating polymer is assumed to have a homogenous resistance throughout the composite. The paths created by physically connected particles but in a direction perpendicular to the current flow from one electrode to the next are neglected. Considering these assumptions, a 3-dimensional network of polymer-particles can be simplified to a 2-dimensional matrix, consisting of randomly connected paths to the current flow.[86] Therefore, R_t, the total resistance between two electrodes as defined in Equation 2.4 is dependent on three parameters:

i) The number of particles between the electrodes creates a connected path that is parallel to the current flow between the electrodes, N_p.

ii) In a unit area traverse to the current flow, the number of series of connected paths that create a conductive path, N_L.

iii) The resistance of a chain of conductive particles with a separation, that is related to the tunneling resistance.[87,88]

$$R_t = \frac{N_p}{N_L} R_p \tag{2.4}$$

Based on Simmon's theory, the tunneling resistance and subsequently the R_p is defined as Equation 2.5. [89–92]

$$R_p = \frac{8\pi hs}{3a^2\gamma e^2} \exp(\gamma s) \tag{2.5}$$

where h is Planck's constant, s is the average interparticle distance between the conductive particles, a^2 is the effective cross-section area through which the tunneling current passes, and e is the electron charge. The parameter γ is defined by Equation 2.6.

$$\gamma = \frac{4\pi}{h}\sqrt{2m_e\varphi} \tag{2.6}$$

Where m_e is the electron mass and φ is the height of the potential barrier between adjacent particles. Therefore, the R_t as the total resistance of the composite based on Equations 2.4, 2.5, and 2.6 can be defined as Equation 2.7.

$$R = \frac{N_p}{N_L}\left[\frac{8\pi hs}{3a^2\gamma e^2} \exp(\gamma s)\right] \tag{2.7}$$

If the composite is under tensile strain in the axial direction and parallel to the electrodes, the change of interparticle distances along the connected path is defined as a function of the applied strain as Equation 2.8.

$$s(\varepsilon) = s_0(1 + E\varepsilon) \tag{2.8}$$

Where s_0 is the initial particle distance, ε is the longitudinal tensile strain, and E is a constant dependent on the material and the applied strain.[93] As strain increases, the change in N_L exhibits a non-linear behavior that can be formulated as Equation 2.9.

$$N_L = N_{L,0} \exp[f(\varepsilon)] \tag{2.9}$$

where $f(\varepsilon) = -(A\varepsilon + B\varepsilon^2 + C\varepsilon^3 + D\varepsilon^4)$, N_L is the number of conductive pathways at the applied strain of ε, $N_{L,0}$ is the initial number of conductive pathways before the applied strain, and A, B, C, and D are constants [36]. The relative change of resistance, or $\Delta R/R_0$ can be formulated as Equation 2.10.

$$\frac{\Delta R}{R_0} = \frac{R}{R_0} - 1 = \left(\frac{s(\varepsilon)N_{L,0}}{s_0 N_L(\varepsilon)}\right) exp\left[\gamma\left(s(\varepsilon) - s_0\right)\right] - 1 \tag{2.10}$$

Based on Equations 2.7, 2.8, and 2.9 the $\Delta R/R_0$ can be described by Equation 2.11

$$\frac{\Delta R}{R_0} = (1 + E\varepsilon)\exp[(A + FE)\varepsilon + B\varepsilon^2 + C\varepsilon^3 + D\varepsilon^4] - 1 \quad (2.11)$$

where $F = \gamma s_0$.

2.5. Hildebrand and Hansen Solubility Parameters

The solubility parameters in this work aid the selection of the solvents for solutes or solvents to be exchanged in various applications. These parameters are especially helpful in predicting the compatibility of a polymer for example for coating and paste preparation and the choice of an appropriate solvent for the wet-spinning method and a corresponding non-solvent for the coagulation bath. In essence, liquids having similar solubility parameters are miscible and exchangeable, and polymers dissolve in solvents with close-enough solubility parameters meaning there is physical affinity between the polymer and the solvent. The extent of interaction of the material is determined by the extent of their similarity in the Hildebrand-Hansen solubility parameters. These parameters determine the miscibility of the material in contact together, denoted by δ_i, and are defined as Equation 2.12.[94,95]

$$\delta = (cohesive\ energy\ density\ of\ a\ compound)^{1/2} \quad (2.12)$$

The total cohesion energy is the sum of individual energies. The basic principle is that the total energy of vaporization of a liquid, meaning breaking all the cohesive bonds, consists of several parts. These are three major interactions in common organic materials that are i) the atomic dispersion forces (δ_D), ii) the permanent dipole-dipole forces (δ_P), iii) and the molecular hydrogen bonding or electron exchange (δ_H). The dispersion interactions are derived from the atomic forces, called dispersion, as atoms build molecules, all molecules have these types of attractive forces. The second type of cohesion energy is the permanent dipole-dipole interactions which are molecular interactions based on the dipole moment as the primary parameter. Hydrogen bonding or the electron exchange parameter is the third major interaction, similar to polar interactions, based on attraction between molecules having hydrogen bonds. The Hildebrand-Hansen solubility parameters, as the sum of the squares of the dispersion, polar, and hydrogen bonding are defined as Equation (2.13).[94]

$$\delta^2 = \delta_D^2 + \delta_P^2 + \delta_H^2 \quad (2.13)$$

In investigating the solubility of a solute in different solvents, the Hildebrand-Hansen solubility parameters are considered as the three-dimensional parameters locating the center of the sphere of the solute material in a three-dimensional cartesian space. The interaction distance or radius is the radius of the sphere, r_0, which determines the boundary of good vs bad solvents. The bad or non-solvents for the solute are outside the boundary or the sphere.

To classify the solvents, the relative energy density (RED) is defined in Equation 2.14, a physical affinity parameter determining whether the Hildebrand-Hansen solubility parameters are close-enough.

$$RED = \frac{r_a}{r_0} \tag{2.14}$$

Where r_a is defined in Equation 2.15

$$(r_a)^2 = 4(\delta_{D\ Solvent} - \delta_{D\ Solute})^2 + (\delta_{P\ Solvent} - \delta_{P\ Solute})^2 + (\delta_{H\ Solvent} - \delta_{H\ Solute})^2 \tag{2.15}$$

To determine whether a specific solute is dissolvable in a chosen solvent, the RED of the two is calculated based on Equation 2.15. In the case where the RED has a value larger than or equal to 1, it means that the Hildebrand-Hansen solubility parameters of the two are close enough, or in other words, the solvent is considered a good solvent and is located inside or on the boundary of the solute sphere. If the RED is larger than 1, it means the solvent is bad or non-solvent for the solute.[94,95] In our case, we are interested in calculating the RED for the EVA copolymer. The RED of a copolymer can be calculated based on the Hildebrand-Hansen solubility parameters of the constituent pure homopolymers and their corresponding weight ratio present in the copolymer,[96] that is in our case polyethylene (PE) and polyvinyl acetate (PVA). The EVA copolymer used in this work has 40 wt. % vinyl acetate and therefore its Hildebran-Hansen solubility parameters can be calculated based on Equation 2.16.

$$\delta_{i\ EVA} = \delta_{i\ PVA} W_{PVA} + \delta_{i\ PE} W_{PE} \tag{2.16}$$

Where $\delta_{i\,EVA}$ is the Hildebrand-Hansen solubility parameter of EVA used in this work, W_{PVA} is the weight ratio of polyvinyl acetate in EVA, and the weight ratio of polyethylene is calculated as $W_{PE} = 1 - W_{PVA}$.

2.6. Mechanical Properties of the Strain Sensors

The strain sensing response of a stretchable strain sensor based on a composite of conductive particle and an insulating elastomer, as it is discussed in the following sections, is mainly controlled by the surface interactions between the conductive filler and the elastomer, and the mechanical behavior of the filled elastomer.[85]

2.6.1. Stress-strain Diagram

As depicted in Figure 2.3, to characterize the mechanical behavior of a stretchable sensor, there are various terms and definitions, derived from the stress-vs-strain diagram under a uniaxial tensile strain test. This curve provides descriptive parameters about the material's strength, ductility, stiffness, and failure limits. The stress-vs-curve is obtained as a result of a destructive tensile strain test, in which a gradually increasing normal force is applied to the material until the point of failure. Stress, or to be more specific, engineering stress, is defined as the ratio of the internal force (resisting the applied external force) to the initial cross-sectional area, assuming there is a uniform distribution of the applied external tensile force throughout the material. The strain provides a measure of deformation due to the applied force. The first stage in a stress-strain curve is the linear region. In contrast to brittle materials which undergo fracture as stress increases, stretchable materials such as soft elastomers exhibit elastic behavior following a plastic deformation region avoiding early mechanical breakage as stress increases. The elastic deformation range is generally referred to linearly stress-vs-strain range where deformation is reversible, whereas plastic deformation (in which the material shows ductile behavior) is generally referred to as the range after the linear range as strain is increased.[65]

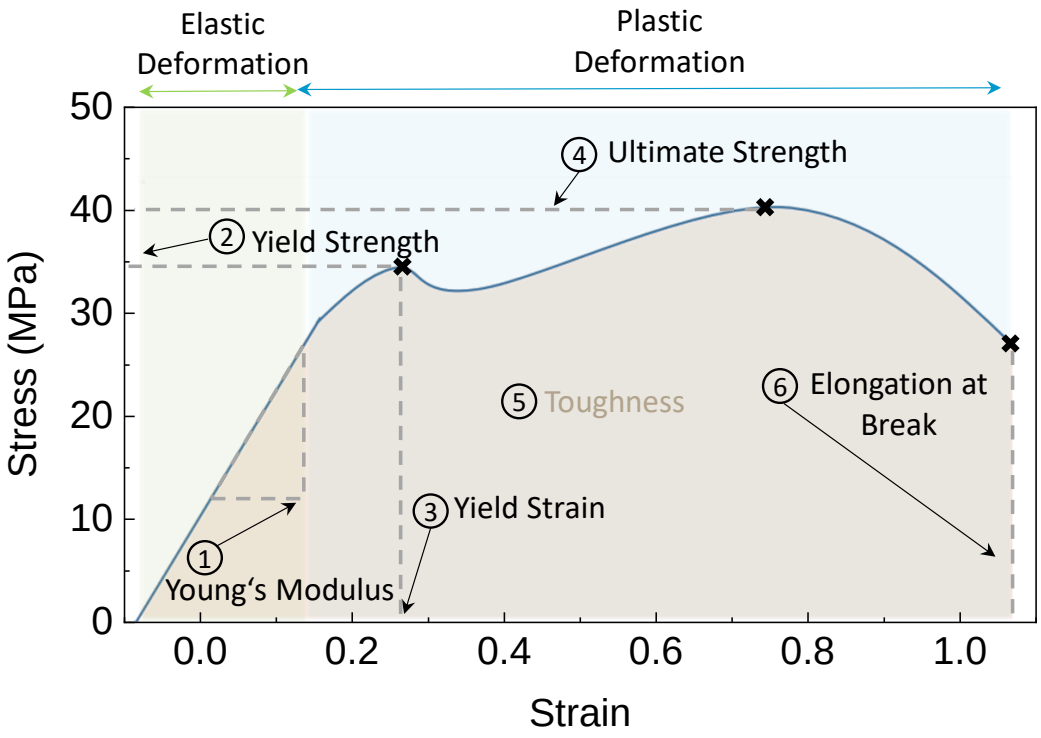

Figure 2.3. Stress-strain curve of a typical stretchable material illustrating the relationship between the (engineering) stress and the measured strain. From this curve, various mechanical characteristics can be extracted, as depicted. 1) Young' modulus is the slope of the linear region indicating the stiffness of the material. 2) Yield strength and 3) yield strain, respectively, are the coordinates of the onset of plastic deformation. 4) Ultimate strength is the maximum stress a material can withstand before the failure point. 5) Toughness is the total energy a material can absorb (integrated area of stress-strain curve) before the failure point. 6) Elongation at break indicates the maximum strain a material can withstand right before the failure point.

Young's Modulus

Young's modulus is a parameter defined as the slope of the stress-strain curve in the linear region which is the ratio of the applied stress to the strain in the elastic (linear) range. It provides a figure indicating the stiffness of a material and the ease of elongation. In this range, the stress is proportional to the strain.

Yield Strength and Yield Strain

As the material is under increasing tensile strain, beyond the stress-strain proportionality limit (where stress-strain change is linear), the rate of strain increase gets faster than the stress. This is reflected in a flattening of the stress-strain curve, the yield point, or elastic limit, is the first peak appearing, before the curve takes a downward turn. However, a stretchable material still demonstrates reversibility in deformation and recovery when the tensile force is removed. Yield strength or yield stress is the corresponding stress at the onset of plastic deformation. After this point, the material enters the plastic deformation region in which upon unloading the force the deformation is not recoverable anymore.

Ultimate Strength

The second stage in the stress-strain curve is the strain hardening region, where strain goes beyond the yield point, until reaching a second peak of stress at the ultimate strength point. This is the maximum sustainable stress by the material under a destructive tensile test.

Elongation at Break

As the material is further elongated above the ultimate strength peak, the elongation at break or the ultimate failure strain point is reached, meaning the material breaks. The extent of the ductility of a stretchable material undergoing plastic deformation, before the failure point, is called elongation at break.

Toughness

Toughness is a property indicating the required energy for the mechanical deformation per unit volume before the rupture of the material. It is the area under the stress-strain curve and can be calculated by integrating the curve.

2.7. Electromechanical Characteristics of the Strain Sensors

The performance metrics of a piezoresistive strain sensor, that is electromechanical characteristics, are determined by the particle-particle interactions inside the composite as well as the polymer chain dynamics. Understanding the key principles involved in the response of the sensor is essential for its performance optimization and future-tailored sensor material and structure designs. In this regard, strain sensitivity (or gauge factor) and hysteresis play a crucial role in classifying the sensor performance and mitigating the potential hindrances for expanding its application.

2.7.1. Gauge Factor

Since the main working principle of a piezoresistive sensor is a change in its resistance upon external strain, a higher resistance change ensures an easily detectable signal even in small strain ranges. However, there is a need for a unified description of the strain sensitivity. The gauge factor (GF) of a reversible piezoresistive sensor is defined as the output response amplification corresponding to a change in the input strain as described in Equation 2.17.[25,88]

$$GF = \frac{\Delta R}{R_0} \cdot \frac{1}{\Delta \varepsilon} \tag{2.17}$$

Where the initial resistance of the sensor is denoted as R_0 in a neutral state ($\varepsilon = 0$), R is the resistance of the sensor at a stretched state ($\varepsilon \neq 0$) and $\Delta R = R - R_0$. The strain sensitivity of a piezoresistive strain sensor depends on various factors such as active sensing elements, particle-polymer interactions, and the microstructure network.[12]

2.7.2. Durability

One of the main applications of the piezoresistive strain sensors is the dynamic (that is over time, in contrast to static) detection of strain under a prolonged repetitive stimulus. Therefore one of the key parameters to be investigated is the durability of the sensor. It is defined as the mechanical robustness as well as dynamic repeatability of the sensor's electrical response to a large number of consecutive cycles of strain-release without failure. One underlying

reason behind the poor dynamic durability in some composites stems from a structural low-fatigue resistance, especially due to the interfacial instability at the particle-(amorphous)polymer interface. However, due to the multi-phase nature of a semi-crystalline and amorphous polymer housing solid conductive particles, predicting mechanical interactions, and improving them, is a major challenge to overcome in SPC strain sensors.[25]

2.7.3. Hysteresis

In SPC strain sensors, hysteresis is defined as the non-repeatable or non-uniform electromechanical response to strain-release cycles. It is the cycle-history-dependent response of the sensor, meaning the electrical response to the current $(n)^{th}$ cycle is not perfectly identical to the next $(n+1)^{th}$ cycle, and it depends on the strain history $(n-1)^{th}$ cycle. Since one major mode of strain detection based on a piezoresistive mechanism is dynamic cycling mode, identifying the source of the hysteresis plays a crucial role in designing efficient and reliable sensors. In stretchable composites of a solid particle embedded in an elastomer, the main sources of the hysteresis are the storage and loss of the elastic energy in the matrix, the viscoelastic nature of the elastomer matrix and the stretchable substrate, the polymer chain interactions with solid particles especially at the interface between the constituent elements, and the interparticle frictional energy in the matrix (as particles and clusters move relative to one another). Although stretchable composites are usually used in their typical linear elastic range (before the yield point), as subjected to repeated cycles of strain-release, the energies generated internally are dissipated as heat, particularly at the soft-hard interfaces, leading to the onset of hysteresis. This is particularly due to the elastic-viscous (viscoelasticity) nature of the polymer as well as a perturbance in the effective strain accommodation by the polymer chains due to the presence of the solid particle network. It is clear that as the stress and the corresponding strain applied to the composite are increased, more heat is generated, and therefore the hysteresis increases. The concentrated stress and heating act as a major source of delamination, void formation, and composite failure. Especially as the microstructure breakdown starts and void spots are generated where there are high concentrations of stress.[25,83] Hysteresis is usually observed as the appearance of a second peak for a single strain-release cycle, indicating a negative piezoresistivity as an inverse response to the strain.[37,97–100] Another typical indication of the presence of hysteresis in a sensor is the extent of its response time to the applied and released strain and

whether there is a difference in the straining compared to the releasing and the magnitude of this difference. A standard response time is defined as the time constant needed for the sensor to reach 90% of the level of the applied or released strain.[12,101,102] It is unambiguous that all sensors based on a polymer exhibit hysteresis to some extent. To be more specific, hysteresis in the response time happens due to, including the above-mentioned points, the unbalance between the microstructure breakdown (as strain is applied) and the re-creation of disconnected paths (as strain is released).[97,103–105] The other origins of hysteresis, especially when a longer relaxing response time is observed, are attributed to a high interfacial area between the conductive particles and the elastomer, poor interfacial adhesion to conductive particles, high friction between the particles and the elastomer molecules (slow slippage of particles against one another or elastomer molecules), and sluggish re-agglomeration of the separated particles (due to the loss of elastomer-filler bonds). These factors result in inhibiting fast recovery of the particle network, which is reflected in a second shoulder in the course of repetitive cycles and a longer time constant for relaxing. The extent of hysteresis and delay is usually directly proportional to the magnitude of strain and the strain rate.[98,100]

Another type of hysteresis is observed as a decline in the peak of the electrical response of the sensor during repetitive cycles of strain-release, which can be explained by the increase in the re-creation of conductive paths.[106] However, there have been cases where the peaks increase over time, indicating a growth of fatigue in the composite, which is caused by the increase of the microstructure breakdown and the inability of the elastomer to recreate conductive paths due to the retarded motion of the molecular chains.[107] One underlying reason behind the above-mentioned hysteresis types can be the Payne effect and the Mullins effect. Payne stress-softening effect is a phenomenon observed in elastomers, and more pronounced in filled-elastomers. It deals with the storage and loss modulus as a means to describe the hysteretic behavior due to the particle-particle network interactions. Under a dynamic mechanical test, a viscoelastic material is under repetitive cycles under stress applied with a certain frequency. In a perfectly elastic material, the stress and the measured strain occur without a phase difference between them, in other words, they occur simultaneously. A viscoelastic material, however, having both viscous and elastic traits, exhibits some phase lag between the applied stress and the measured strain. In a viscoelastic material, storage modulus is the stored energy in the elastic portion of the material. Loss modulus is the energy dissipated as heat in the viscous portion of the material. As strain

increases above a threshold, depending on the microstructure of the particle network, there is a drastic drop in the storage modulus, observed as an overall stress-softening.[108–111] Mullins effect focuses on the changes in the elastomer's structure as its stress-strain response over time changes when the cycling repetition increases. It specifically deals with the irreversible changes as the sources of increased energy dissipation due to the failure of the polymer, and in filled-elastomers due to the debonding of the chains and particles.[109,112–115] More specifically, it explains that the current stress-strain curve is influenced by the maximum strain the composite is previously subjected to. Mainly explained by the irreversible disentanglement of polymer chains, there is softening of the elastomer upon being strained above the previously experienced level, leading to the accumulation of residual strain and anisotropically dissipated energy in the composite.

2.8. Direct-current Electric Field Induced Percolation

It is important to note that, the percolation generally does not only depend on the particle to polymer volumetric ratio but also it is a time and processing-dependent phenomenon. The interfacial interactions between the particle and the polymer change overtime until reaching a thermodynamic equilibrium. Therefore, percolation threshold investigations are a more dynamic rather than static phenomenon.[116] The particle-polymer interface interactions are attributed to the surface charges. The surface of a solid particle dispersed in a liquid medium obtains excess surface charge (static charge).[117] The charge is caused either by the surface adsorption of functional groups present in the medium or by ionization of the surface groups.[118,119] Closest to the surface of the charged particle a dense stationary layer of the counter-charges from adsorbed species is formed which is called the Stern layer. These counterions are considered to be strongly bound to the surface and immobile. Above the Stern layer, close to the particle surface in the liquid medium, a cloud of oppositely charged species appears, called the diffuse layer. This layer is formed by the medium to screen the electrostatic Coulombic attraction force of the Stern layer. In total, a so-called electrical double layer (EDL), is formed, comprising both layers on the surface of the particle. [120] The thickness of the double layer depends on the charged species concentration in the liquid medium and is a measure of how far the electrostatic effect of particle charge persists in the medium. The Debye-Hückel screening length, λ_D or κ^{-1}, is the point at which the surface charge of the particle at the liquid medium is decreased by $1/e$ (where e is the base of the

natural logarithm). The diffuse layer located loosely around the particle in the medium can shear away as an electric field is applied to the particle. The potential of the surface of the diffuse layer called the zeta potential ζ, quantifies the effective surface charge of the dispersed particle.

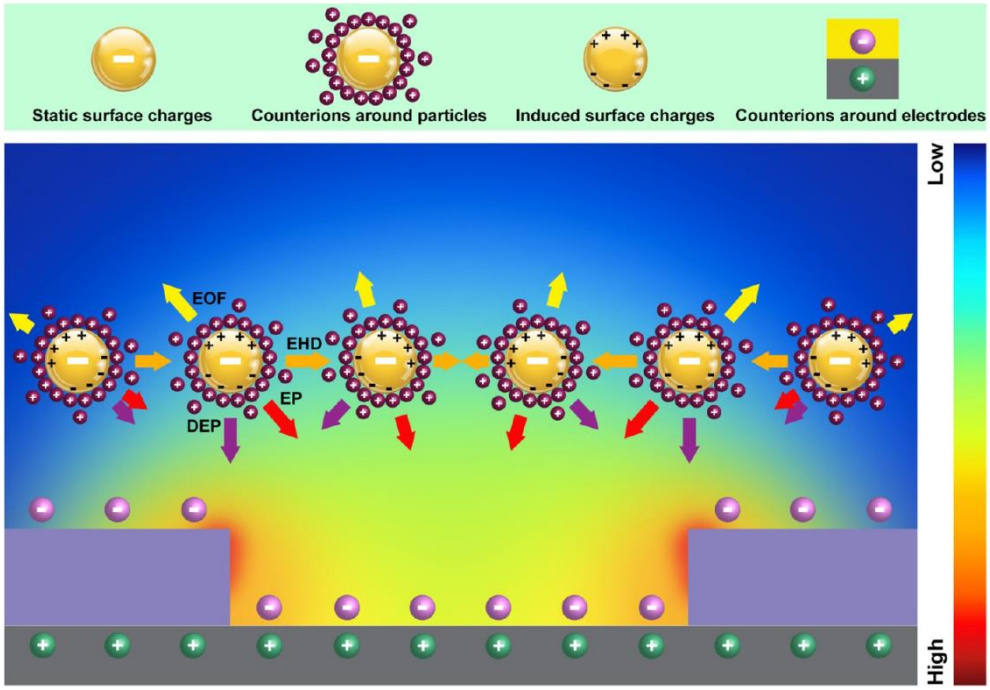

Figure 2.4. Illustration of forces applied to a solid particle-liquid medium composite when an electric field is applied to them. Solid particles inside a liquid medium obtain a surface charge (i.e. static charge). To screen this layer, inside the medium counter-charges accumulate around the surface of the particles and the substrate. Conductive particles polarize in the presence of the electric field, causing induced surface charges. Due to the presence of these charges on the dispersed particles, substrate, and electrodes, and their interactions, several forces act on the constituents, which are electrophoretic force (EP), dielectrophoretic force (DEP), electroosmosis flow or drag force (EOF), electro-hydrodynamic flow (EHD), adapted from [117] American Chemical Society licensed under CC-BY-NC-ND 4.0.

2.8.1. Electrophoretic Force

When a uniform or low-frequency electric field is applied to the two electrodes having a mixture of dispersed charged particles in a liquid medium, the particles move toward the electrodes.[121] The movement of a particle can be under the influence of the Coulomb attraction force between oppositely charged electrodes and the particles' fixed net surface charges. This is known as electrophoresis (EP) shown in Figure 2.4. Electrophoresis force

(F_{ep}) or the electrokinetic force, described in Equation 2.18, [117] is the main responsible for the motion of the charged particles toward oppositely charged electrodes

$$F_{ep} = 6\pi\, \varepsilon_m r \zeta_p E_{dc} \tag{2.18}$$

Where E_{dc} is the magnitude of the electric field, r is the particle radius, ε_m is the medium permittivity (or dielectric constant of the medium), and ζ_p is the Zeta potential of the particle. Electrophoretic deposition is commonly used to fabricate particle-polymer films or to coat colloidal particles onto electrode surfaces.

2.8.2. Electrophoretic Mobility

Another important characteristic of a dispersed particle under an electric field is its electrophoretic mobility, μ. It is defined as the ratio between the particle's velocity v and the electric field strength E as $\mu = v/E$ or via the Henry equation[122]

$$\mu = \frac{2}{3}\frac{\varepsilon_0 \varepsilon_m \zeta_p}{\eta} f(\kappa r) \tag{2.19}$$

Where $f(\kappa r)$ is the Henry function. Equation 2.19 indicates that as the viscosity of the medium (η) increases μ decreases and as ζ_p increases μ also increases. The correlation coefficient between ζ_p and μ depends on the size of the particle. If the particle size (r) is much smaller than the Debye length of the countercharged layer ($\kappa r \ll 1$), the electrophoretic mobility of the particle can be defined by the Hückel equation (which is the simplified form of the Henry equation (Equation 2.19)

$$\mu = \frac{2}{3}\frac{\varepsilon_0 \varepsilon_m \zeta_p}{\eta} \tag{2.20}$$

And if r is much larger than the Debye length ($\kappa r \gg 1$) μ is given by the Helmholtz-Smoluchowski equation

$$\mu = \frac{\varepsilon_0 \varepsilon_m \zeta_p}{\eta} \tag{2.21}$$

2.8.3. Drag Force

Another force affecting the movement of a particle dispersed in a liquid medium under a direct-current (DC) electric field, is hydrodynamic drag force or electrohydrodynamic flow (EHD), shown in Figure 2.4. When a polarizable liquid is exposed to a DC electric field, the same as the charged particle, it obtains electrophoretic mobility. Additionally, the dielectric substrate in between the two electrodes develops a surface charge, corresponding to the double layer formed in the liquid mixture. The mobility of the charged species in the medium, due to the EP and the double layer, can be approximated by the negative sign of Equation 2.21. This moving liquid drags the particles, with a hydrodynamic drag force[123]

$$F_{drag} = 6\pi\eta r v \tag{2.22}$$

Where η is the viscosity of the medium, r is the radius of the particle, and v is the velocity of the particle. The drag force, in the opposite direction of the applied field, generally distorts the assembly of the particles along the electric field.

2.8.4. Chain Force

A conductive particle dispersed in a medium polarizes when subjected to an electric field.[121] Polarization manifests in the adsorption of the medium molecules (i.e. the EDL). If the particle is more polarizable than the surrounding medium, that is due to the difference in their dielectric permittivity (ε), at the interface of the particle and the medium, an induced dipole moment forms in the direction where the electric field density is higher. The induced dipole moments interact with each other with an attractive electrostatic force, called the chain force (F_{chain}).

$$F_{chain} = -C\pi\ \varepsilon_m r^2 K^2 E_{dc}^2 \tag{2.23}$$

Where C is a coefficient ranging from 3 to $>10^3$ (depending on the interparticle distance and the length of the particle chain),[119] r is the particle radius, and K is the Clausius-Mossotti function. K indicates the ratio of the electrical properties of the particle and the medium and their contribution to the chain force being exerted on the particle. For a homogeneously spherical particle, K is defined as [124]

$$K = Re\left[\frac{\widetilde{\varepsilon_p}-\widetilde{\varepsilon_m}}{\widetilde{\varepsilon_p}+2\widetilde{\varepsilon_p}}\right] \quad (2.24)$$

Where $\widetilde{\varepsilon_j} = \varepsilon_j - i\sigma_j / \omega$ is the complex permittivity of the particle or medium, ε_j permittivity of the particle or medium, σ_j is the particle or medium conductivity, and $i = \sqrt{-1}$. In a DC electric field, K is defined as[124]

$$K = \frac{\sigma_p-\sigma_m}{\sigma_p+2\sigma_m} \quad (2.25)$$

As we work with conductive spherical particles dispersed in an insulating medium ($\sigma_p \gg \sigma_m$), K depending on the conductivity of the medium and the particle, takes the maximum value, $K = 1$.

2.8.5. Dielectrophoretic Force

As illustrated in Figure 2.5, as the first and closest polarized conductive particle is attracted to the electrode it modifies the field intensity distribution in the whole material, as if forming a new electrode tip including the surface of the attached conductive particle. Subsequently, a high field intensity region forms in between the particle (attached to the electrode) and the nearest polarized particle floating in the medium. Thus, the nearest particle will move toward the new tip, under the influence of its dipole moment interactions with the new tip. The mutual force of interaction can be attractive or repulsive, depending on the alignment of particles. Particles located parallel to the field direction are always attracted along the field gradient (to the high-intensity regions), forming a chain parallel to the DC field direction. This chain-like structure continues to grow inside the liquid medium until it reaches the other electrode. A single pair of induced dipole moments interact with the dipolar chain energy of u_{dp} [125]

$$u_{dp} = -\frac{p^2}{2\pi\varepsilon_0\varepsilon_m d^4} P_2(cos\theta) \quad (2.26)$$

Where d is the center-to-center distance of the particle pair, P_2 is the second-order Legendre polynomial function, θ is the angular position of the particle pair with regard to the direction of the electric field, and p is the dipole moment of the particle pair

$$p = 3\varepsilon_0\varepsilon_m V_p KE \quad (2.27)$$

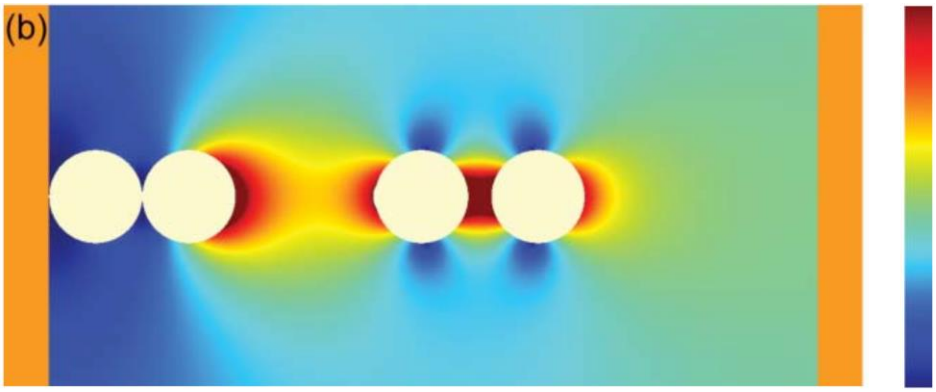

Figure 2.5. Simulation showing the distribution of the electric field applied to conductive particles dispersed in a low permittivity medium (ε = 2). As the first conductive particles attach to the electrode (the bars on the side shown in orange), they alter the electric field distribution throughout the medium, resulting in the formation of a chain of aligned particles, reproduced from [120] with permission from the Royal Society of Chemistry.

The force equivalent of the dipole chain energy, $\vec{F}_d$ is as follows

$$\vec{F}_d = -\frac{p^2}{4\pi\varepsilon_0\varepsilon_m d^4}(15\,cos^2\theta - 3)\hat{\boldsymbol{r}} - (6\cos\theta)\hat{\boldsymbol{z}} \tag{2.28}$$

Where $\hat{r}$ is the unit vector connecting the particle pair and $\hat{z}$ is the unit vector that points toward the direction of the electric field.[125] Provided that there is a gradient of the electric field (under a nonuniform electric field), which happens as the first particle is attached to the electrode, another force emerges acting on the dispersed particles, called dielectrophoretic force (F_{dep}). This force stems from the interaction of the induced dipole moments. Under a non-uniform field, the dielectrophoretic force acting on a polarized particle is defined as

$$\vec{F}_{dep} = \frac{3}{2}\varepsilon_0\varepsilon_m V_p\, K^2\nabla E^2 \tag{2.29}$$

Where V_p is the volume of the particle, ε_0 is the electric permittivity of the free space, and ∇E^2 is the gradient of the field squared. The sign and the strength of this force depend on the effective polarizability of the particle which is defined based on the real part of the Clausius-Mossotti function (in our case it is K = 1).

3. Materials and Methods

In this chapter, the materials used in the fabrication of the stretchable piezoresistive strain sensors are presented. The fabrication methods utilized in this work include additive manufacturing and printing methods. The characterization techniques for the evaluation of the morphology and microstructure of the sensors are described. Then the electromechanical test procedures performed to investigate the sensing properties of the strain sensors are introduced. Lastly, the preparation of the three measurement setups for the application demonstrations is detailed.

3.1. Materials

In this work, the development, microstructure investigation, and performance evaluation of piezoresistive strain sensors prepared with straightforward fabrication methods using uncomplicated and unconventionally large conductive material are discussed. As detailed in the previous chapters, a typical piezoresistive SPC strain sensor involves an insulating elastomer, a conductive part, and electrodes that alow the sensor's resistance measurements. The choice of material used in this thesis is based on enabling high sensitivity, especially in micro-strain ranges, while allowing uncomplicated and cost-effective processability for large-scale fabrication. All materials are used as received without additional preparation.

3.1.1. Substrates and Stencil

For percolation threshold studies (static resistance measurements), as the substrate for Sections 4.2, 4.4, 4.6, 4.7 a flexible polyethylene terephthalate (PET) film with a thickness

of 150 µm is used. The stretchable substrate used in the rest of Chapter 4, and Sections 6.1 and 6.2is the elastic polyurethane (PU) with a thickness of 150 µm (Platilon U 9122 150 Natural, Covestro). For printing the electrodes on top, the PU substrate is cut into 40 × 60 cm pieces using an industrial (blade) cutter in the cleanroom and used as received. As the stencil for stencil printing of the sensor material on a PET or PU substrate, a PET film with a thickness of 170 µm is used. Using a CO_2 laser, an array of rectangulars is cut through the stencil. Then the stencil is cleaned with isopropanol in the ultrasonic bath for 15 minutes and dried at room temperature for 30 minutes.

3.1.2. EVA

Ethylene vinyl acetate copolymer resin with 40 wt.% vinyl acetate (ELVAX™ 40 W, DuPont de Nemours, Inc) is used as the primary elastomer throughout this thesis. A 3D ball-and-stick model of the EVA with the chemical formula $(C_2H_4)_n$ $(C_4H_6O_2)_m$ is shown in Figure 3.1. The optimized EVA solution used in this thesis is prepared by mixing a 1:4 weight ratio with anisole. The solution mixture is stirred on a 55 °C hotplate for three hours to ensure EVA is homogeneously dissolved in anisole. The solution is then kept at room temperature for 15 minutes (to reach ambient temperature) before intermixing microsphere particles.

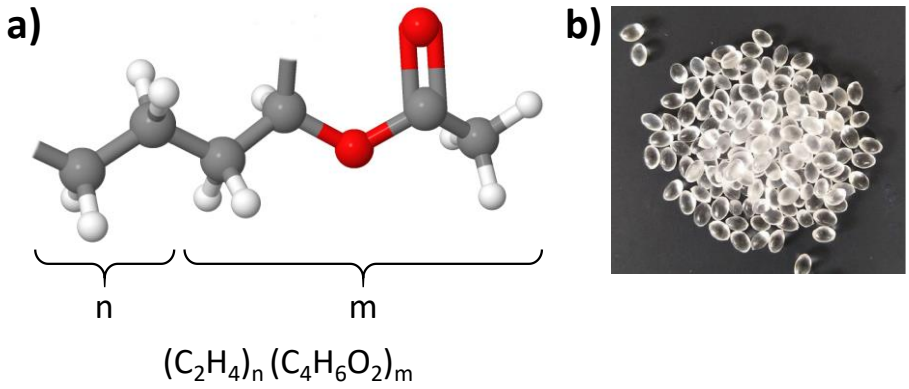

Figure 3.1. Ethylene vinyl acetate (EVA) copolymer as the main elastomer used in this work with a 40 wt.% vinyl acetate ($C_4H_6O_2$). a) Ball-and-stick 3D model.[a] b) EVA resins.[b]

[a] The ball-and-stick 3D chemical structure is drawn using: https://biomodel.uah.es/en/DIY/JSME/draw.en.htm
[b] Image from https://www.guidechem.com/

3.1.3. PDMS

In Chapter 4, the microstructure morphology, percolation threshold, and electromechanical performance of EVA are compared with those of PDMS. Under the trade name of Sylgard® 184 (Dow Corning Corporation), PDMS, as two separate liquid component kit, part A as a base and part B as a curing agent, is used as received.

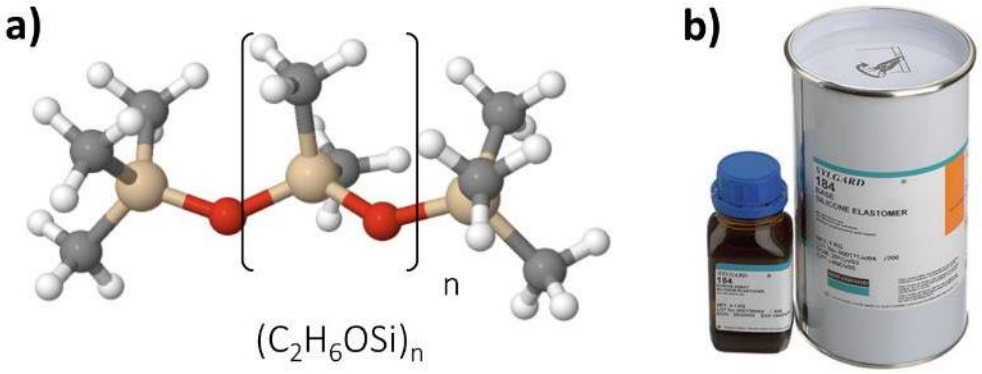

Figure 3.2. Polydimethylsiloxane (PDMS). a) ball-and-stick 3D model.[a] b) The two parts, the base and the curing agent.

Figure 3.2 shows the 3D ball-and-stick model of the PDMS with the chemical formula $(C_2H_6OSi)_n$. The PDMS mixture is prepared by manually mixing a 10:1 weight ratio of the base and the curing agent for three minutes. To remove the air bubbles created during manual mixing, the mixture is degassed by three quick pump-vent cycles in a low-vacuum oven. Immediately after degassing, the prepared PDMS is used for microsphere intermixing.

3.1.4. Core-shell Silver-glass Microspheres

The active sensing elements of this work are conductive core-shell silver-coated glass microspheres. With an average diameter of either 4 µm (SLGMS-AG-3.3 1-7 um) or 35 µm (SLGMS-AG-2.58 32-38um) both from Cospheric LLC the microspheres are received as dry powders, as shown in Figure 3.3. To avoid particles flying during handling, due to the electrostatic charges, a static remover gun (Milty Zerostat 3 Anti-static remover gun,

Analogue Seduction) is shot three times on the hands wearing gloves and the glass vials containing the dry powders.

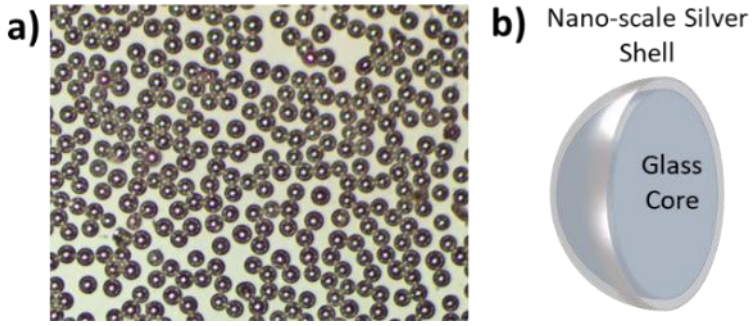

Figure 3.3. Conductive core-shell silver-glass microspheres as the active sensing elements used in this work. a) The silver-coated glass microspheres image.[c] b) Structure of the conductive particles. A nano-scale silver layer is coated on a core of glass.

3.1.5. Anisole

Anisole (anhydrous, 99.7%, Sigma Aldrich) as the main solvent in this work with the chemical formula C_7H_8O is used to dissolve the EVA. It is also called methoxybenzene and is considered a non-toxic solvent. Its 3D ball-and-stick model is shown in Figure 3.4.

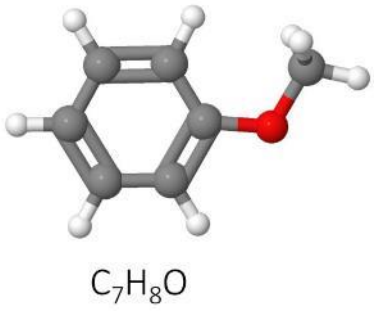

Figure 3.4. Anisole's ball-and-stick 3D model[a] as the main solvent used in this work to dissolve the EVA copolymer resins.

3.2. Fabrication Methods

The focus of this work is to fabricate strain sensors with high-throughput and scalable methods that are industrially relevant. In doing so, all material preparation steps are done in

[c] Image from: https://www.cospheric.com/SLGMSAG_silver_coated_solid_glass_spheres_beads.htm.

a straightforward and minimalistic approach, avoiding the addition of extra chemicals or various post-processing steps. In the following, the fabrication methods employed to prepare the strain sensors are described.

3.2.1. Electrode Printing

To keep all the fabrication steps scalable and reproducible, the screen printing method is used for the deposition of the silver electrodes on the stretchable PU and flexible PET substrates. In this work, an industrial high-throughput screen printing machine (Thieme) is used for the cost-effective deposition of silver electrodes onto PET and PU substrates. For the electrode material, screen-printing silver paste (DUPONT™ PE873, DuPont) is mixed for five minutes manually and then screen-printed on the substrate. Then the substrate having the paste printed on top is dried on a 100°C hotplate for 30 minutes. Afterward, the substrate is cut into 30 × 50 mm pieces. Using vinyl tape (3M™ VINYL TAPE 471) it is fixed on a glass slide to prepare it for the following stencil printing of the sensing material.

3.2.2. MS-EVA Composite Paste Preparation

To prepare the main sensing composite, the dry powder of solid conductive microspheres is added to the prepared EVA solution or the degassed PDMS mixture. The mixing is done manually with a spatula for 30 seconds at room temperature to obtain a uniform dispersion of the particles. The mixing ratio of the microsphere to the elastomer depends on the respective study. For electromechanical tests and for the application demonstrations a stated ratio above the respective percolation threshold is chosen. The pastes are used for the fabrication of the sensors immediately after being prepared.

Laser Cutting

To cut the stencil out of the PET films (Chapter 4, and Sections 6.1 and 6.2) and cut the poly(methyl methacrylate) sheets (PMMA) for battery expansion monitoring setup (Section 6.3 in this work, we utilize a Laserman Speedy 300 laser cutter from Trotec. According to the digital layout designed by the Inkscape software and transferring it to the Laserman user

interface, either cutting or engraving on various substrates is feasible. A carbon dioxide laser with adjustable laser power (up to 200 watts), laser speed, lasing frequency, and laser distance to the substrate allows for cutting various intricate structures on a substrate with mm to cm thicknesses.

3.2.3. Stencil Printing of MS-EVA Composite

As an additive manufacturing technique, for deposition of the main sensing material, in Chapter 4, and Sections 6.1 and 6.2, the EVA-microsphere or PDMS-microsphere solution mixture is deposited on the substrate using the stencil printing in the cleanroom. As the stencil, a PET film with a thickness of 170 µm and a rectangular negative mask in the middle is used. As shown in Figure 3.5, the stencil is brought in contact with the substrate that has silver electrodes on top. The prepared paste is then manually deposited onto the electrodes and the substrate, through the mask, using a blade. The stencil is then removed. For the preparation of both the PDMSs and EVA-containing sensors (discussed in Sections 4.2 to 4.6), to avoid stressing the particle agglomeration and allow contact formation at relatively lower ratios the printed composite is kept at ambient temperature (at cleanroom temperature, 20° C) for one hour. However, throughout Sections 4.7 and 4.8, to have similar sample preparation procedures in the absence of an electric field compared to when an electric field is applied, the prepared layers are dried immediately after being printed. This is the main reason behind an increase in the percolation threshold from 20% in Section 4.2.1 to 33% in Section 4.8 indicating the time-dependent nature of the percolation. Drying the printed layers (to evaporate the residual solvent) is performed by placing the substrate having the printed material placed in a 100 mbar vacuum oven at 40°C for one hour. For the case of PDMS-containing material, after resting at room temperature for one hour, the substrate is placed in the oven at 80°C for 12 hours. At this point, the sensors are prepared and ready for the subsequent investigations.

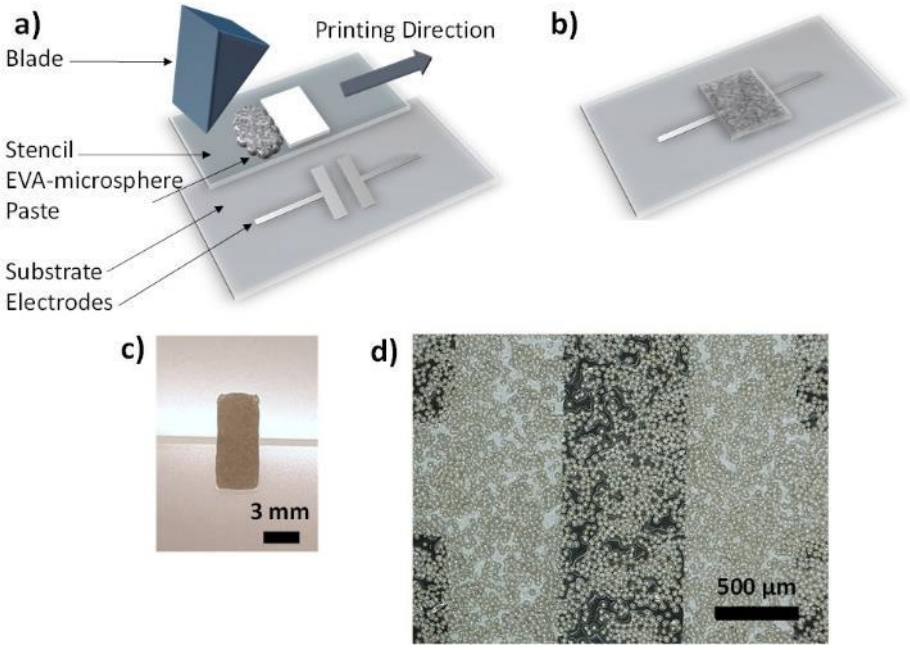

Figure 3.5. Stencil printing and the structure of the printed sensor (the electrodes shown in this figure are used for percolation threshold investigations). a) Schematic illustration of the stencil printing method for the deposition of the sensing material discussed in Chapter 4, and Sections 6.1 and 6.2. b) Schematic illustration of the sensor (composed of the printed composite on the substrate). c) Digital photo of the sensor. d) Optical microscope image of the sensor using 35 µm microspheres.

3.2.4. Wet-Spinning of MS-EVA Composite

For the preparation of the free-standing microfiber strain sensor, the microsphere EVA solution mixture is prepared as explained in Section 3.2.2 and loaded into a 3 ml spinning syringe. The extrusion (wet-spinning) is performed, as shown in Figure 3.6, in the cleanroom using a dispenser pump (Smart Dispense 06, Martin). Via a tube, the pump is connected to the syringe filled with the mixture. A needle with a gauge of 18 and 25 mm length with an optimized spinning rate of 50 mm s^{-1} is used to extrude the mixture into the acetone bath as the nonsolvent. During wet-spinning the coagulation takes place. To allow for the solvent exchange process to complete, the coagulated two-meter-long microfiber is kept in the non-solvent bath for three minutes at room temperature. Afterward, the microfiber is collected around a 20 mm diameter spool. To ensure complete evaporation of the acetone, the microfiber is dried under a 100 mbar vacuum at room temperature for one hour.

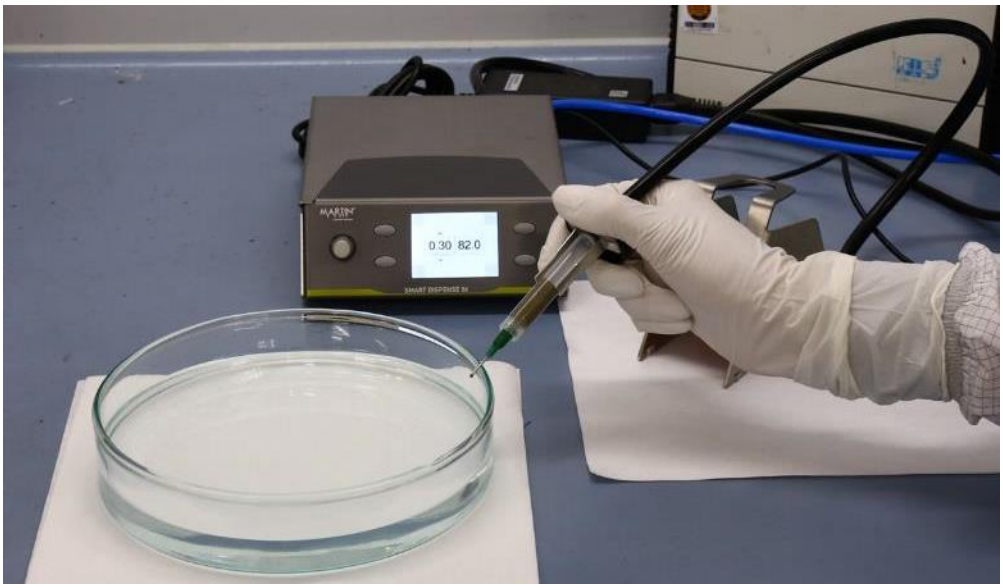

Figure 3.6. The wet-spinning method is used for the fabrication of the free-standing microfiber sensor. A dispenser pump, connected to a tube, controls the pressure at the back of the dispensing nozzle.

3.3. Characterization Techniques

This section describes the characterization techniques used for investigating the morphological, mechanical, and electrical characteristics of the sensors in this work.

3.3.1. Optical Microscopy

The optical microscope (OM) in this work is used for a detailed investigation of macroscopic-level microstructure morphology. Additionally, in-situ microsphere network formation of a wet state under a DC electric field is performed using OM. In this work, a Nikon Eclipse 80i microscope is used to capture optical images of the printed sensors or the stand-alone microfibers. As the light source, a halogen lamp is used. Using a variety of objectives, different magnifications are employed, ranging from 5x to 100x. Various filters on the beam path enable different modes of illumination and investigation of the sample. The modes of microscope used in this work are the dark field, bright field, and differential interference contrast. The sample is illuminated using the broadband light source, passed a semi-transparent mirror, and mode-corresponding filters (if activated via the nose-piece). The reflected light from the sample is magnified and directed at the adjustable eyepiece and

or the digital camera (5 megapixels). The microscope images, with the help of the connected camera, can be transferred to a computer using the manufacturer's user interface software, Nikon Basic Research, providing detailed images and videos for further structural analysis.

3.3.2. Scanning Electron Microscopy

In this work, to obtain high-resolution images of the sensing material for morphology and interface investigation, the ZEISS Supra60 VP scanning electron microscope (SEM) is used. A typical SEM uses high-energy electrons to image specimens at the nanometer scale. The electrons are generated thermionically from a filament, then accelerated to high energies (0.2 – 40 KeV) using electrostatic condenser lenses and focused on a spot on the sample to about 0.4 to 5 nm spot. The beam is then deflected to raster-scan over a rectangular area of the sample. As the beam is incident on a material, upon its interaction with atoms at different depths of the material, it can be either transmitted, reflected, scattered, or absorbed, overall loosing its initial energy. Therefore, different types of signals are generated such as back-scattered electrons, secondary electrons, X-ray, Auger electrons, and cathodoluminescence emission. These signals provide information about the elemental composition of the sample its crystalline structure and morphology. To produce the SEM images with topological details of the surface of the sample with a resolution down to 1 nm, the intensity of the secondary electrons is used to create an image of the surface. In this work top-view and cross-sectional images are taken. For the cross-sectional imaging, the printed sensors and the microfibers are frozen using liquid nitrogen and broken to have a neat look.

3.3.3. Profilometry

To determine the thickness of the deposited layers on the substrate tactile profilometry is performed. In this work, a Veeco Dektak 150 profilometer from Bruker is used. A diamond needle tip with a diameter of 12.5 µm is brought in contact with the surface of the sample (in z-direction) applying a set pressure to the surface (the force applied is equivalent to 1 to 15 mg). The stage, with the sample fixed on top of it, moves in one direction under the needle covering distances from 50 µm to 55000 µm ranges, with a set scanning rate. The probe maps the surface in one dimension providing z-direction data of the specimen with down to

10 nm resolution. In this work, we use profilometry to measure the thickness of the printed composites on the substrate or the screen-printed silver electrodes.

3.3.4. Tensile Tests

In this thesis, various tensile tests are applied to the sensors to determine the mechanical characteristics of the stretchable sensors, and foremost, to investigate their electrical properties. As shown in Figure 3.7a, the tensile tests are applied via a universal test instrument (FMT-310BU) from Alluris with a 500 N force and displacement transducer head (FMT-310FUC5) with 0.1 N precision. Applied force and displacement are in the longitudinal direction of the sensor, using two pairs of clamps on the two sides, as shown in Figure 3.7b, with a displacement rate of 900 mm min^{-1} (unless otherwise specified). For the simultaneous electrical resistance measurement during a tensile test, using a grounded source measure unit (Keithley 2612B) in a two-probe mode, the sensor is sourced a DC voltage of 50 mV while its real-time resistance readings are recorded. The sensor under test is connected to the Keithley using two crocodile clamps. For the printed sensor on the PU substrate, the crocodile clamps are connected to the screen-printed electrodes. For the microfibers, they are connected to the copper tapes adhered to the microfibers. During mechanical characterizations, a monotonically increasing tensile strain is applied to the sensors until the rupture point is reached.

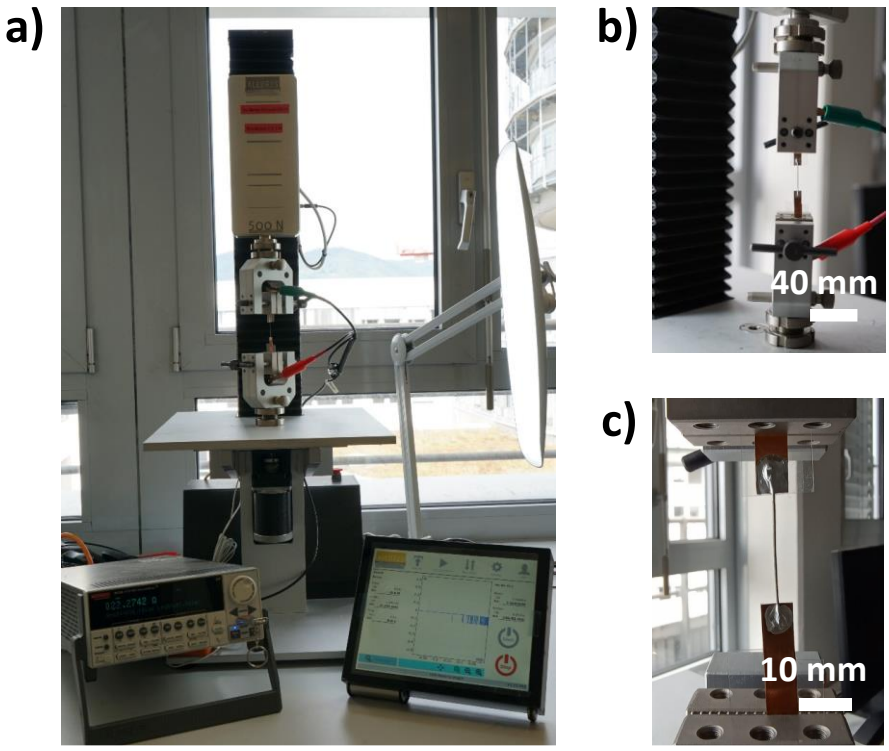

Figure 3.7. Electromechanical test apparatus utilized in this work. a) Photograph of force and displacement apparatus (Alluris) and the connected source-measure unit (Keithley) during a typical electromechanical or mechanical measurement.

4. Printed Strain Sensors Based on EVA and Microspheres

In this chapter, using an elastomer and conductive core-shell microspheres, a printable and deformable paste is developed. The stencil printing method is used for the fabrication of the strain sensors. As the elastic polymer, EVA as a cost-effective alternative material is compared to PDMS, a widely used elastomer. We compare the elastomers concerning the microstructure and the electromechanical characteristics of the printed sensors using 35 µm microspheres. The primary observed difference between the two elastomers is in the interface formation with conductive microspheres, which is reflected in the electrical percolations of the sensors and better performance of the EVA-based sensors. EVA is chosen over PDMS due to a lower percolation threshold and less electromechanical hysteresis. To further improve the electrical properties of the sensor, we utilize 4 µm microspheres and analyze the electromechanical performance of the 4 µm containing strain sensors. Lastly, by applying a DC electric field to the printed composites, we study the parameters affecting the percolation threshold and modify these parameters to further lower the percolation threshold. Parts of the results presented in this chapter have been previously published as a journal article in Advanced Sensor Research.[126]

4.1. Introduction

The growing interest in high-resolution and conformable strain sensors is fuelled especially by the Industry 4.0 revolution, the booming of the Internet of Things (IoT), and digitalizing society.[25] Printing methods are most favorable in this regard as cost-effective approaches

for the industrialization of these sensors. Out of different sensing ideas explored so far in stretchable sensors, a composite of an elastic polymer having conductive particles provides a straightforward sensing approach and a highly affordable manufacturing option.[127] Additive manufacturing of an SPC of randomly dispersed conductive particles is a promising approach for cost-effective large-scale fabrication of the strain sensors.[125] Conductive pathways start to emerge within these composites as soon as the critical percolation threshold is reached.[128] When subjected to an external tensile force, the material internally undergoes deformations to accommodate the force, resulting in a change in the electrical resistance. The capability to sense very small strains with a detectable resistance change, and to detect the smallest differences in the input strain by providing an easily measurable resistance change are of crucial importance for a variety of applications. The characteristic responses of a piezoresistive sensor are dictated by the choice and manipulation of the elastomer and conductive particles and their interface and their interaction with regards to the applied strain. Although PDMS is a highly utilized elastomer in a large body of studies on stretchable composite sensors,[36,65–67] it is not cost-effective and it poses difficulties primarily because the cross-linking process starts spontaneously at room temperature.[68] Most works reported so far, employ nanofillers as conductive fillers[12,25] however in most cases, they lack high sensitivity at small strain regimes (small strain is defined as $\varepsilon < 1\%$).

To enhance the sensitivity under small strain, a practical strategy is to minimize contact points among conductive fillers through the utilization of spherical particles. One recent report on polyacrylamide hydrogel microsphere-based strain sensors demonstrates a 0.05% strain as the lowest detection limit and a minimum strain resolution of 0.1%. However, their fabrication process is complex, involving several steps, various solvents, and the addition of an extra encapsulation layer. It includes processes like inverse emulsion polymerization, filtration, and immersion in multiple solvent mixtures.[129] Another work demonstrates that utilizing a monolayer of conductive microspheres embedded in PDMS yields a 0.3% strain as the minimum sensing limit and no information is reported on the resolution limit of such sensors.[130] Another work reports an increase in sensitivity, up to 10 times, and a minimum strain sensitivity of 0.01% by incorporating insulating nano-scale spherical fillers as an additional post-processing step in the network of graphene-flake and polyurethane.[131] However, their method involved several fabrication process steps and the addition of extra

material as their sensing elements. Nonetheless, the majority of the existing literature has been solely on strain detection in large strain ranges, using multiple steps for fabrication, or a variety of conductive or insulating materials are used as the sensing elements.[44,66,67,130,132] Overall, the path of high-resolution small strain sensing using conductive microspheres produced through straightforward printing techniques is left overlooked.[56,133]

In this chapter using a scalable printing method, with particular attention to small strain sensing, we introduce a stretchable strain sensor based on conductive core-shell microspheres and an elastomer. Manufactured using the stencil printing method, we showcase EVA as a more cost-effective substitute for the typically employed and costly PDMS, considering both morphological and electromechanical characteristics. Strain sensors prepared with EVA demonstrate significantly decreased electrical percolation compared to PDMS sensors. Employing EVA, we explore how the size of the conductive microsphere impacts the performance of the stretchable sensors. Our experiments yield a highly sensitive and linear response, exhibiting a very low detection limit and resolution. Additionally, we analyze the electromechanical robustness of the sensor response to consecutive overload strain-release cycles and 1000 cycles of strain-release. Finally, we examine further decreasing the percolation threshold in the EVA matrix by applying a DC electric field to the printed sensors. These findings open up numerous potential applications for these sensors. Parts of the results presented in this chapter are published in the Wiley journal of Advanced Sensor Research.[126]

4.2. EVA vs PDMS Comparison

As PDMS is a commonly selected elastomer in creating piezoresistive SPC sensors, we conducted a comparison investigation between sensors based on PDMS as the elastomer and those made with EVA. The morphological differences between the microsphere-polymer interface are explored using OM and SEM images. The electrical percolation threshold for both composites of PDMS and 35 µm microspheres (35MS-PDMS), and EVA and 35 µm microspheres (35MS-EVA) are estimated and proposed as a possible explanation for the observed differences. Furthermore, an electromechanical test is carried out to see how the sensors respond to identical strain-release cycles and their performances are compared. As

presented in Figure 4.1a, sensors are fabricated by stencil printing of the developed paste onto and in between the screen-printed silver electrodes on a stretchable PU substrate. Figure 4.1b is a photograph of the printed layer onto the electrodes which are used for percolation threshold investigations throughout Chapter 4. Figure 4.1c presents the OM image of the printed layer (here using 35 µm microspheres and EVA). Figure 4.1d is a schematic illustration of the cross-section of the printed composite in the relaxed state where a conductive path is formed. By reaching the critical percolation threshold, agglomerated conductive microspheres form conductive paths inside the elastomer. The schematic illustration in Figure 4.1e shows as a tensile force is applied to the two sides of the substrate, the applied force causes a strain resulting in the slight displacement of the microspheres in the elastomer, hence disconnecting some of the conductive paths.

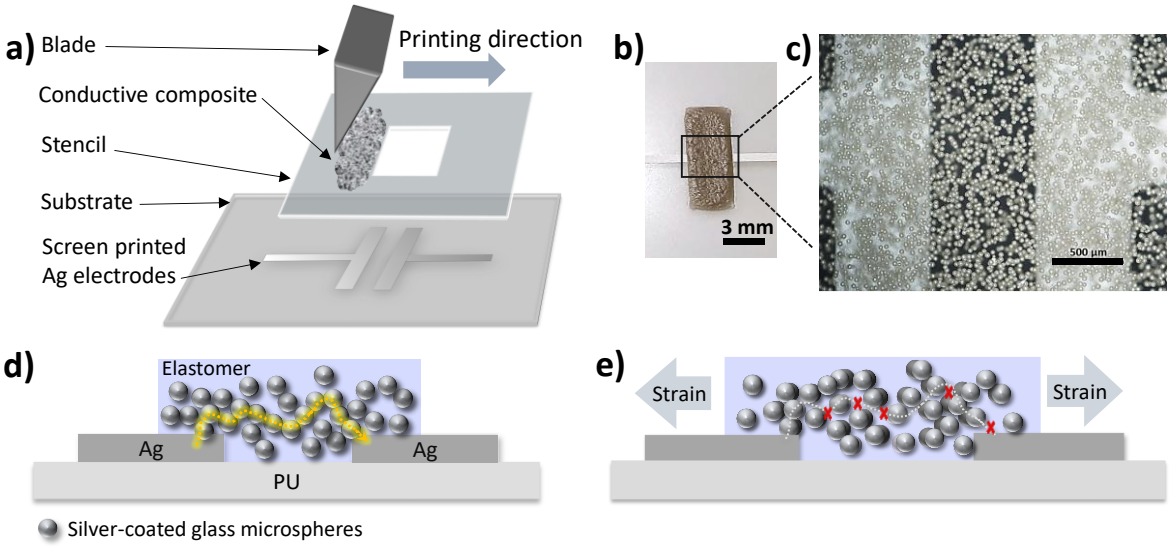

Figure 4.1. Building blocks of a stretchable strain sensor fabricated by printing. a) Silver electrodes are screen-printed onto the PU substrate, before the stencil printing of the sensing material. Then the substrate having the stencil on top is fixed while a blade having printing paste in front of it is driven on the stencil surface. The paste deposited on the electrodes has an inverse shape of the stencil. b) Photograph of the printed sensor composite (scale bar 3mm). c) OM image of the printed composite (scale bar 500 µm). d) Schematic illustration of the cross-section view of the stretchable composite sensor (schematic not to scale). e) Schematic illustration of the stretched composite under a uniaxial tensile strain which might disconnect some of the conductive paths,

4.2.1. Percolation Threshold Investigations

The measured conductivity data obtained for the 35MS-PDMS (represented in red color) and 35MS-EVA (represented in blue color) are shown in Figure 4.2. These data are fitted to the percolation equation

$$\sigma/\sigma_0 = (\varphi - \varphi_c)^t \quad (4.1)$$

which is a power law relationship between conductivity (σ) and volume fraction (φ) (Section 2).[134] It is important to note that the printed layers (both EVA- and PDMS-based ones) are rested at room temperature for one hour, before drying on the hotplate or in the vacuum oven. As the formation of a percolated network of particles means reaching a thermodynamic equilibrium,[116] we notice an improvement in microsphere distribution when the printed layers are rested for one hour at room temperature before drying the solvent.

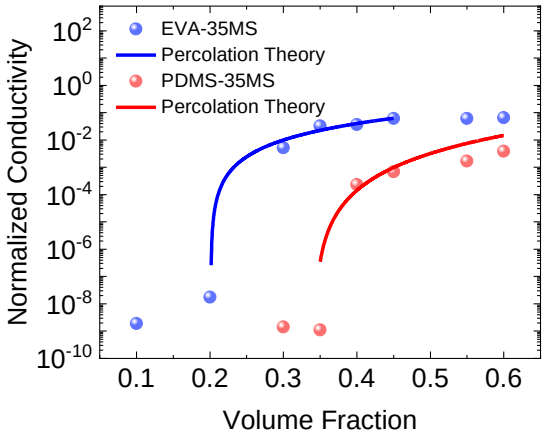

Figure 4.2. Percolation threshold comparison of 35MS-EVA with 35MS-PDMS composites. The normalized mean conductivity as a function of volume fraction is fitted to the percolation theory (Kirkpatrick model). For the 35MS-EVA a percolation threshold of 20% is estimated, whereas for the 35MS-PDMS a percolation threshold of 34%.

Based on the above-mentioned model, the percolation threshold for 35MS-PDMS is calculated to be 34%, whereas for the 35MS-EVA it is determined to be 20%. This points out a significant reduction (-41%) in the percolation threshold when EVA is employed in comparison to PDMS.[135] This finding suggests that conductive paths form at a notably

lower volume fraction of microspheres when EVA is the chosen elastomer. The percolation exponent (*t*) is found to be 3.12 for 35MS-PDMS and 1.99 for 35MS-EVA.

4.2.2. Microstructure Morphology Investigation

To understand the cause behind the variations in percolation thresholds, we investigated the microstructure of the composites produced using both PDMS and EVA each at 40 vol.%. The OM image of 35MS-EVA (Figure 4.3a) displays clusters of closely packed microspheres. Examining the microsphere-EVA interface in greater detail via the cross-sectional SEM image in Figure 4.3b, we observe the development of a loosely structured layer surrounding the particles, which promotes the creation of a percolation network.

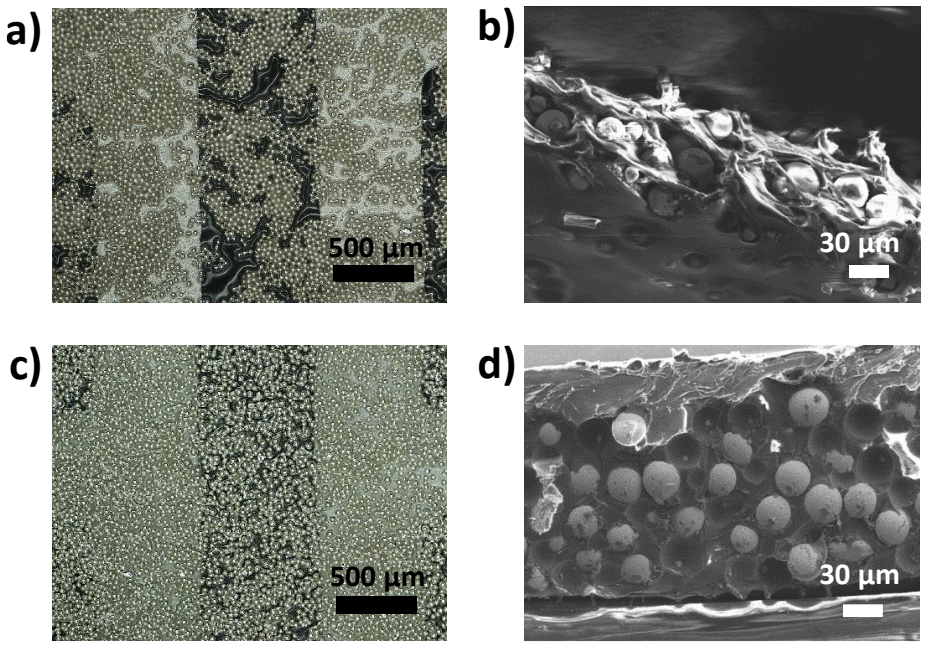

Figure 4.3. Microstructural characteristics of the 35MS-EVA composite compared with 35MS-PDMS. a) OM image of the 35MS-EVA composite. b) Cross-sectional SEM image of 35MS-EVA composite. d) OM image of 35MS-PDMS composite. e) Cross-sectional SEM image of 35MS-PDMS composite.

A closer look at the OM image of 35MS-PDMS, as depicted in Figure 4.3c, reveals a uniform dispersing of microspheres without any apparent clumping together. Examining the cross-sectional SEM image of 35MS-PDMS in Figure 4.3d, a tightly packed interface envelopes

the microspheres is observed. This arrangement effectively hinders the formation of agglomerations for establishing conductive paths. In diagrams in Figure 4.4a and Figure 4.4b, a proposed mechanism involved in the interface formation for the differences observed is illustrated. It is proposed that within the EVA matrix, the interface is created mainly under the influence of the relatively weak Van der Waals forces acting between the EVA chains and the silver on the surface. In this way, with the least polymer obstructing particle agglomeration, conductive paths form within clusters of microspheres. In the case of PDMS, it is hypothesized that during the mixing of microspheres, before the full polymerization of the chains, the formation of hydrogen bonds with silver coating occurs. The formation of this compact layer around the microspheres separates them from one another. This accounts for the uniform dispersion and isolation of microspheres within the PDMS matrix.

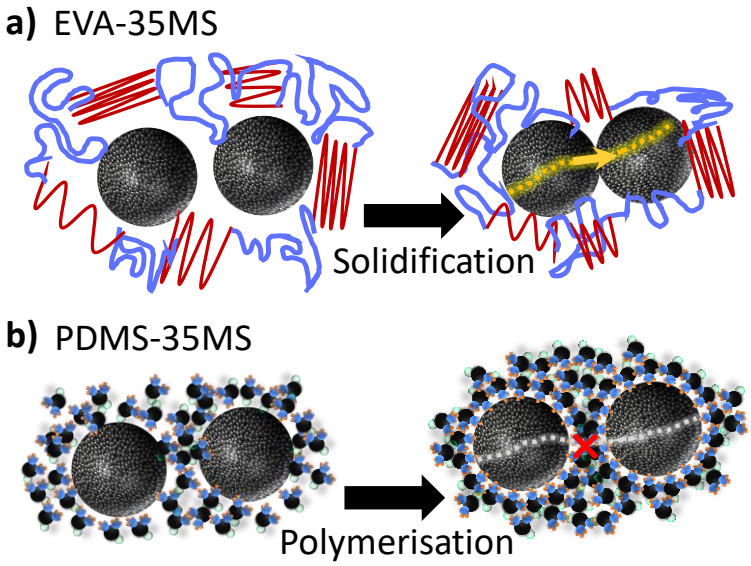

Figure 4.4. A probable explanation for the observed difference in the microstructure of 35MS-EVA and 35MS-PDMS. a) Schematic diagram depicting the proposed process for interface formation in 35MS-EVA composite (diagram not drawn to scale). b) Schematic diagram depicting the proposed process for interface formation in 35MS-PDMS composite (diagram not drawn to scale).

4.2.3. Sensors Prepartion for Electromechanical Tests

The printed sensors investigated in this work have an active sensing length of 20 mm. As shown in Figure 4.5, to investigate the electromechanical characteristics of the sensors they are placed between the clamps of a displacement and force-applying instrument (Section 3.3.4), while the contact electrodes are electrically isolated with a PET foil. The printed sensors are used right after drying and reaching ambient temperature.

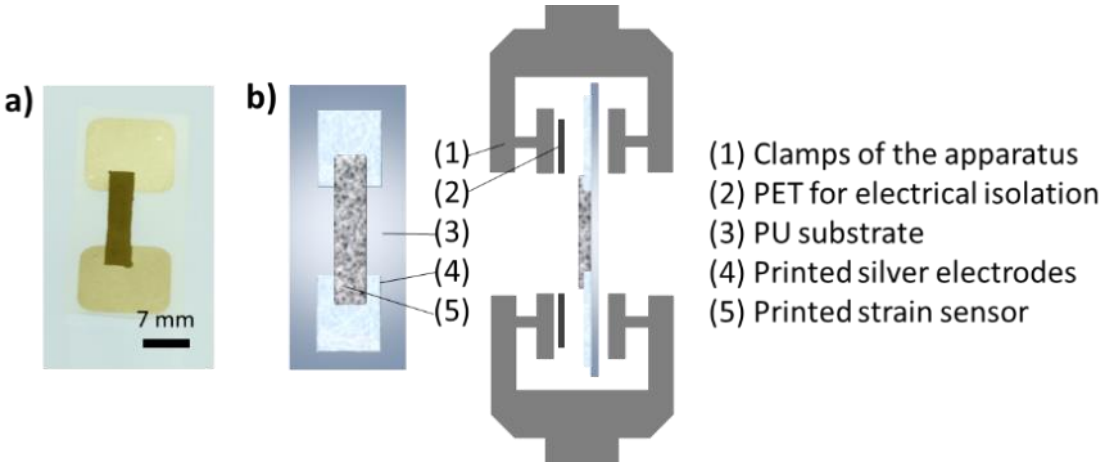

Figure 4.5. Electrode connections of the sensors for electromechanical measurements. a) Photo of the printed sensor as it is used right after being dried and without further processing. b) Schematic illustration of the front and side view of the printed sensor during the electromechanical measurements using the force and displacement apparatus.

4.2.4. Electromechanical Characteristics

The performance of both 35MS-EVA and 35MS-PDMS sensors is explored by subjecting them to cyclic tensile strain while monitoring changes in sensor resistance throughout the test. Figure 4.6a presents a photo of a 35MS-EVA sensor and its silver electrodes screen-printed for the electromechanical evaluation. As depicted in Figure 4.6b, tensile strain is applied along the longitudinal axis. To maintain a consistent electrical response against tensile strain, we selected filler-to-elastomer volume ratios that exceed the percolation thresholds of the composites, which are 35 vol.% for the 35MS-EVA sensor and 45 vol.% for the 35MS-PDMS sensor. The response of the sensors as the relative change of resistance ($\Delta R/R_0$) is illustrated in Figure 4.6c and Figure 4.6d, in response to an applied strain of 0.2%.

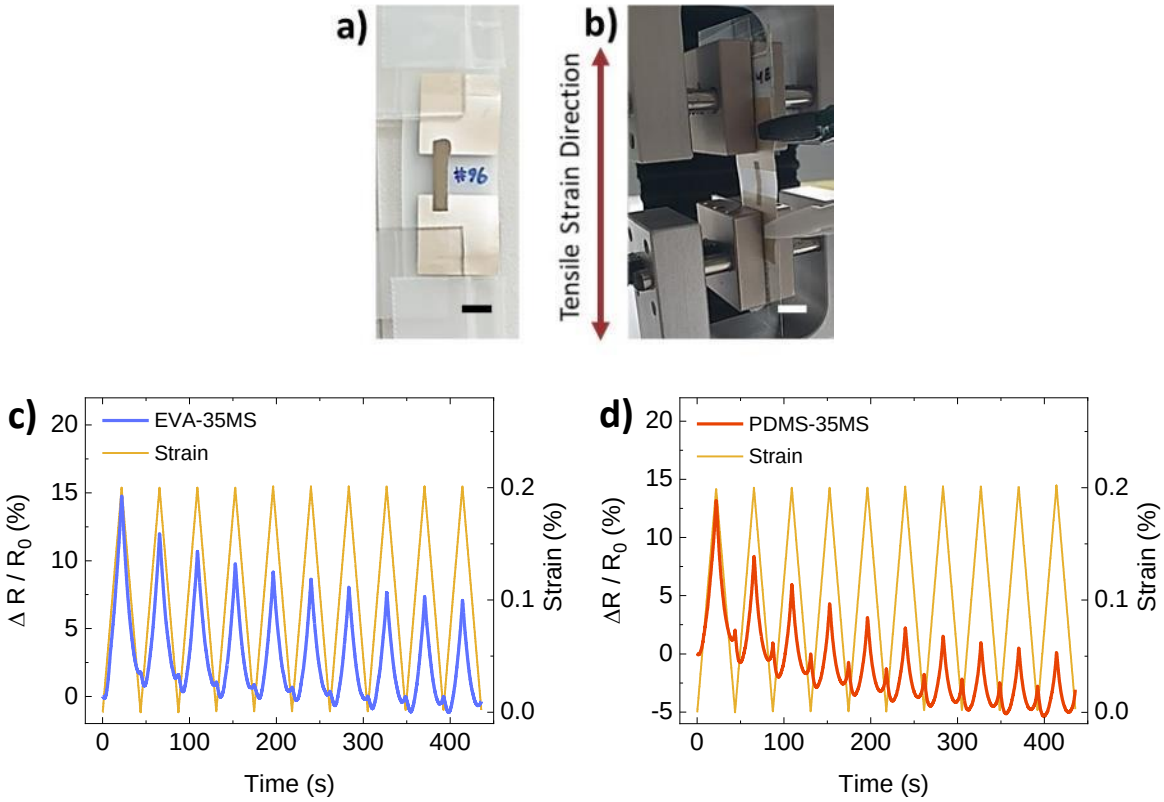

Figure 4.6. Analyzing dynamic cyclic strain tests conducted on 35MS-EVA and 35MS-PDMS sensors. Both sensors undergo ten cycles of 0.2% strain, with a strain rate of 0.5% min^{-1}. a) Photo of the strain sensor for electromechanical measurements (scale bar 6 mm). b) The strain sensor is stretched in the force and displacement apparatus while two-probe resistance measurement is conducted using a source-measure unit. c) The real-time variation in resistance of the 35MS-EVA sensor with a 35 vol.% microsphere content. d) The real-time variation in resistance of the 35MS-PDMS sensor with a 45 vol.% microsphere content.

Analyzing the results of the electromechanical cyclic strain shows the initial cycles in both sensors yield a greater $\Delta R/R_0$ compared to the following cycles. In the 35MS-PDMS sensor, this phenomenon appears to be more pronounced. This type of response which depends on the strain history, is commonly observed in piezoresistive composites of solid fillers embedded in elastic polymers.[106,136] The Payne effect and the Mullins stress-softening effect (Section 2.7.3),[109,110] explain the root cause of this behavior. Based on these two phenomena, the gradual reduction in $\Delta R/R_0$ is caused by the rupture of particle-polymer and particle-particle connecting chains and the fracture of the glassy polymer layer surrounding the particles. In the unstrained state, both sensors exhibit a shoulder peak in their $\Delta R/R_0$,

which is another type of electromechanical hysteresis. The reformation of disconnected conductive paths during releasing of strain is ascribed to account for the increase of resistance as strain is reduced.[98] This type of reverse response to strain is called in the literature as the negative piezoresistivity.[137] It is important to note that for 35MS-PDMS, the shoulder peaks have a larger magnitude compared to the 35MS-EVA. In PDMS, the distinct shoulder peak is likely attributed to the dense interface it creates with the microspheres and the commonly observed delayed relaxation of polymer chains in crystalline polymers.[68,104] However, it is important to highlight that one contributing factor to the poor electromechanical response of the PDMS, might be the necessity to include a relatively large ratio of conductive fillers, compared to EVA.

Concluding Remarks

These insights into the material behavior are valuable for the proper design of stretchable composite sensors and for understanding and optimizing the performance of the sensors. The capability of EVA to effectively minimize the percolation threshold, compared to PDMS, is an advantage. A smaller hysteresis in EVA-based sensor, compared to PDMS, suggests it is promising for further strain tests potentially having a better performance over repeated cycles. Overall, these findings mean EVA is a more favorable elastomer for designing reliable piezoresistive sensors. Hence, we opted for EVA instead of PDMS for our printed sensors due to its cost-effectiveness, ability to significantly reduce the percolation threshold, and its minimal electromechanical hysteresis.

4.3. Electromechanical Characteristics of 35MS-EVA Sensor

Figure 4.7a depicts the ability of the 35MS-EVA sensor to detect a strain as small as 0.01%. In such a small strain range (0.0001 strain) the sensor exhibits a reproducible and easily detectable response with an increase of 0.41% in $\Delta R/R_0$ at the peak. In Figure 4.7b the 35MS-EVA sensor is subjected to cyclic strain of 0.025%, 0.035%, and 0.055%, respectively. Comparing the response of the sensor at 0.035% strain with 0.025% strain, the sensor provides a remarkable +100% increase in $\Delta R/R_0$, highlighting its high resolution to distinguish such small strain differences (+0.01%).

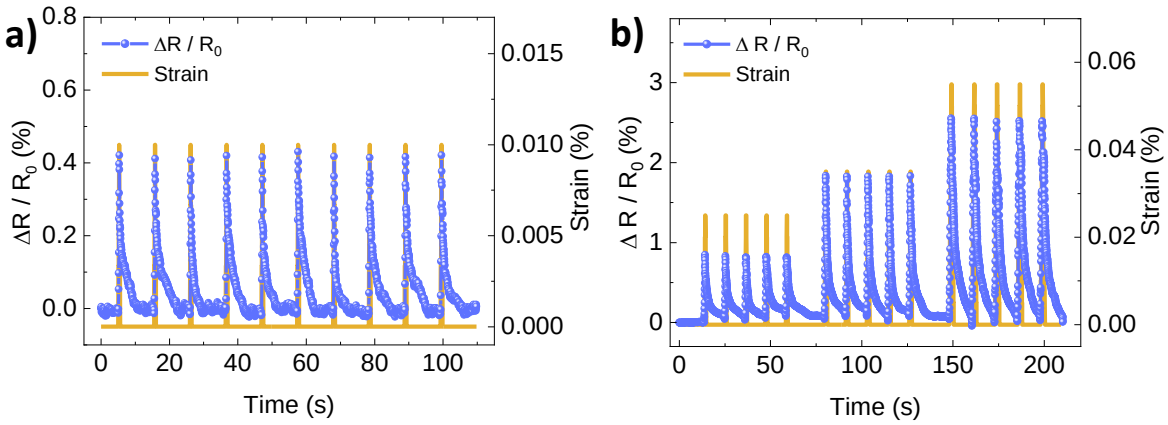

Figure 4.7. Response of the 35MS-EVA sensor to cyclic small strain tests. a) High reproducibility of the sensor response in detecting a repetitive strain as small as 0.01%. b) The capability to distinguish small strain differences with high resolution under consecutive cycles of 0.025%, 0.035%, and 0.055% strain, respectively.

4.3.1. Durability of 35MS-EVA Sensor to Overload Strain

Although employing 35 µm microspheres (35MS) as filler is very beneficial for very small strain sensing, as the deformation increases to strain magnitudes ≥ 0.215%, the sensor shows negative piezoresistivity, as an unwanted effect. For example, as shown in Figure 4.8a, sequentially increasing strain from 0.205% to 0.255% reveals that starting from the peak of 0.215% strain and larger, an unwanted negative piezoresistive effect is observed (reduction in resistance while the strain is increased). This effect is followed by the appearance of a strong shoulder peak when strain is decreased. This worsening of response to strain continues (Figure 4.8b) to the extent that as shown in Figure 4.8c when a strain of 1.2% is

applied, the $\Delta R/R_0$ at the maximum strain shows a value of -40% (meaning $R_{\varepsilon\,max} < R_0$), with a remarkable surge of the shoulder peak up to complete disconnection.

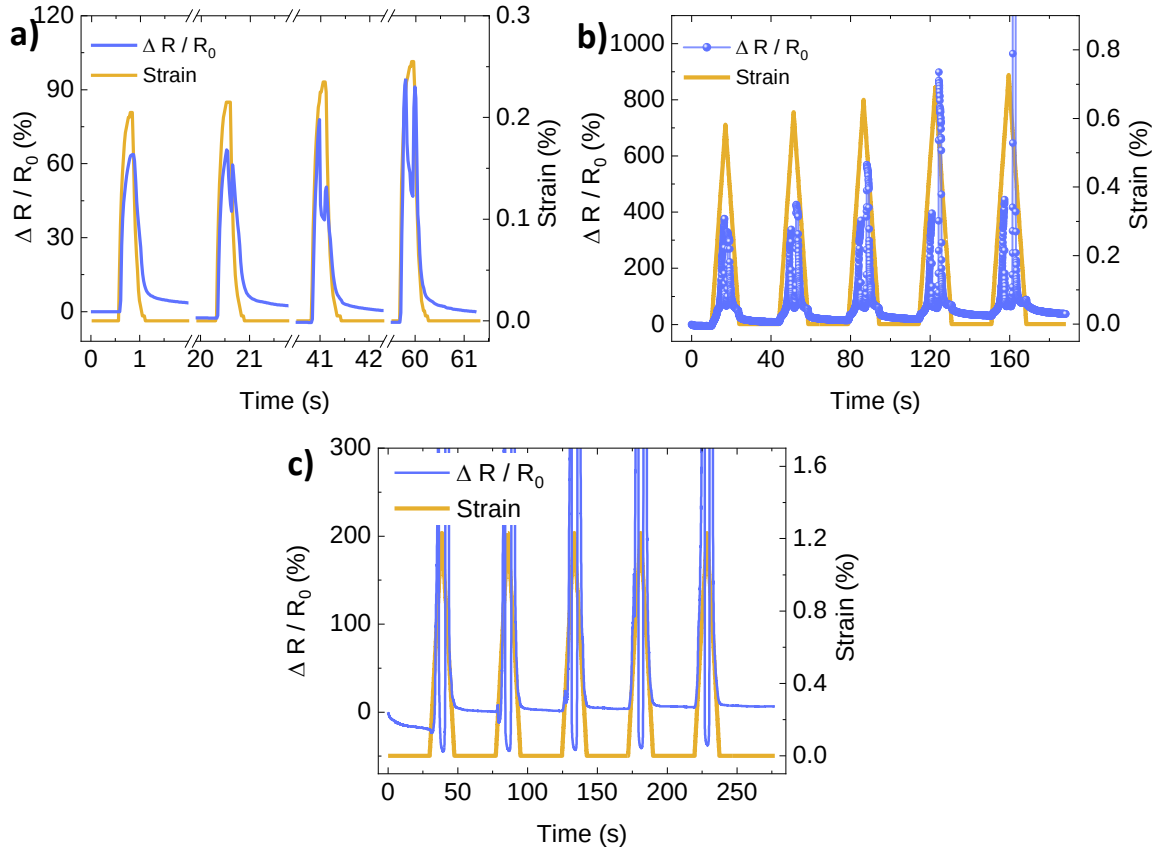

Figure 4.8. Appearance of negative piezoresistivity in the 35MS-EVA sensor under strain values ≥ 0.215% (strain rate here is 100 mm min^{-1}). a) Strain is increased from 0.205% in the first cycle up to 0.255% in the last cycle. A negative strain response appears as the strain peaks to values ≥ 0.215%. b) A negative piezoresistivity is observed clearly both at the peak of strain and when strain decreases. Especially, as strain increases in small steps in the subsequent cycles, the shoulder peak ascends dramatically (the first strain-release is 0-0.55%, and the last one is 0.73%). c) The applied cyclic strain here is 1.2%. Apart from the observed robust behavior, which is retrieved conductivity, both before and after the strain maxima, a strong surge of resistance is observed.

Therefore, although it is noteworthy that the 35MS-EVA sensor is capable of retrieving conductivity after complete disconnection, the overall maximum workable range of this sensor, before negative piezoresistivity is observed, is $\varepsilon < 0.2\%$. We hypothesize that the cause behind the reduced resistance at the strain maxima when the strain is decreased, is the

very large dimension of the conductive particles. From a certain threshold above, sustaining deformation in the elastomer is impeded by the large microspheres and the sensor response to strain eventually goes out of sync.[37,138]

This is why to improve the performance of the sensor, attain less hysteresis effects, and consistent signal in a larger strain range, in the subsequent sections of this chapter, 4 µm conductive microspheres (4MS) as the main sensing elements are explored. In Section 4.6, lowering the percolation threshold of 35MS containing composites is examined in detail.

4.4. Microstructure Morphology and Percolation Threshold Investigations of 4MS-EVA Sensors

The OM images of 4 µm microspheres and EVA-based (4MS-EVA) sensors are shown in Figure 4.9a and Figure 4.9b and the SEM images are shown in Figure 4.9c and Figure 4.9d. Microstructure investigations suggest in 4MS-EVA similar microsphere agglomerations are formed as in 35MS-EVA (Figure 4.3d), which are covered by the EVA matrix.

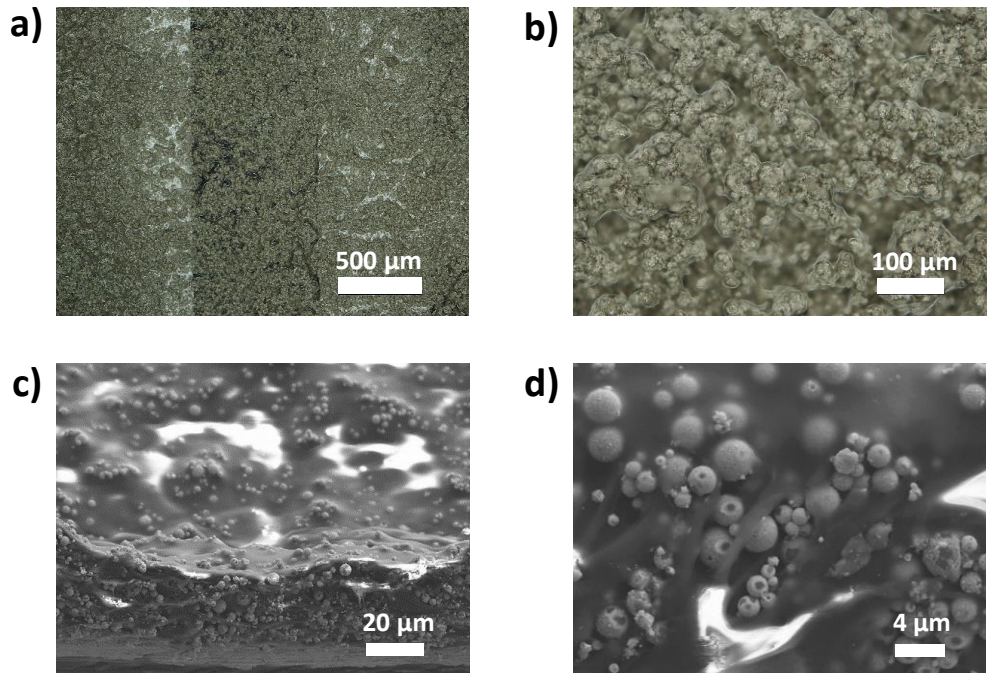

Figure 4.9. Microstructure study of 4MS-EVA sensor material. a) and b) OM images of 4MS-EVA, showing the agglomerated network of microspheres. c) and d) Cross-sectional SEM images of 4MS-EVA, indicating a similar structure to Figure 4.3b is formed when 4 µm microspheres are embedded in the EVA matrix.

The conductivity data obtained for the 4MS-EVA sensor, shown in Figure 4.9, is fitted to the percolation theory, $\sigma/\sigma_0 = (\varphi - \varphi_c)^t$, a power (Section 2.1).[134] Based on this model, the percolation threshold is calculated to be 16%. The lower percolation threshold of 4MS-EVA compared to the 20% percolation threshold of 35MS-EVA (discussed in Section 4.2.1) is attributed to an increase in the surface area of 4MS, meaning increased interfaces with the elastomer and particle-elastomer interactions.[83] Overall, a lower percolation threshold as well as a smaller size of particle suggests that the mechanical performance of the elastomer (accommodation of strain) is less likely impeded by the solid particles embedded in it (compared to the case of 35MS). The critical exponent (t) is found to be 0.6. It is important to note that, the 4MS-EVA printed layers are also rested for 1 hour at room temperature before drying the solvent.

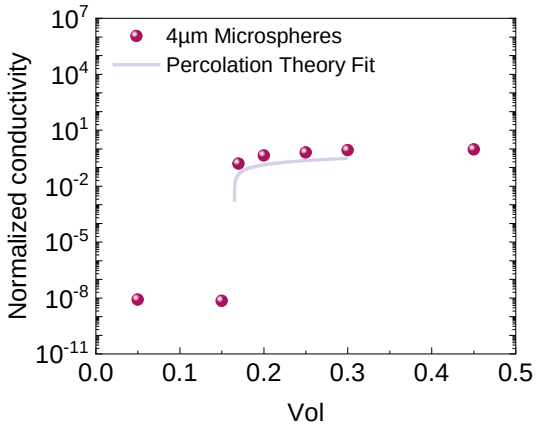

Figure 4.10. Percolation threshold investigation for 4MS-EVA sensors. Fitting the normalized mean conductivity as a function of volume fraction to the percolation theory (Kirkpatrick) model, a percolation threshold of 16% is estimated.

4.5. Electromechanical Characteristics of 4MS-EVA Sensor

The strain sensor composed of 4MS-EVA, as shown in Figure 4.11a, is capable of reliably detecting a strain of 0.015% with a reproducible increase of 0.1% in its response ($\Delta R/R_0$). Figure 11b reveals the resolution of the 4MS-EVA in detecting a strain change of 0.025% (from 0.075% to 0.1%) by an $\Delta R/R_0$ of 67%. This significant change in resistance indicates the high sensitivity of the 4MS-EVA sensor to very small input strain changes.

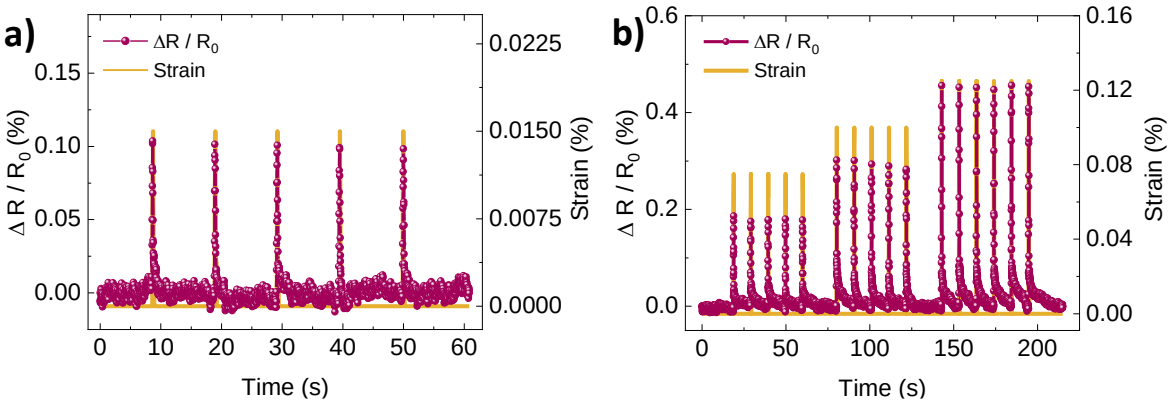

Figure 4.11. Dynamic response of 4MS-EVA sensor to very small cyclic strain tests. a) 4MS-EVA is capable of clearly and reliably detecting a cyclic strain of 0.015%. b) Strain change from 0.075% to 0.1% and 0.125% respectively, showing high resolution of 4MS-EVA sensor in detecting changes of input strain.

Apart from sensitivity to small strain ($\varepsilon \leq 0.1\%$), we examine the response of the 4MS-EVA to larger strain ranges ($\varepsilon > 0.1\%$). Figure 4.12 shows a reproducible $\Delta R/R_0$ against cyclic strain tests of 0.5%, 1%, 2%, and 3%, respectively.

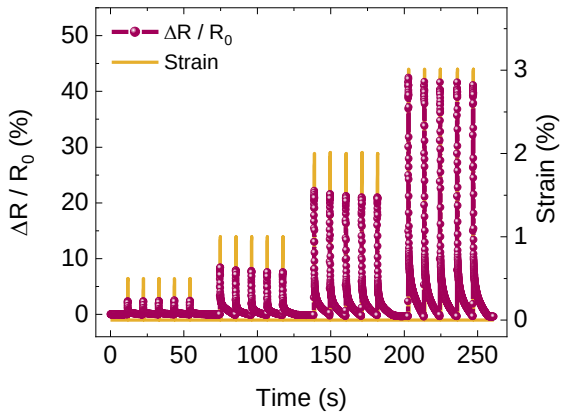

Figure 4.12. Dynamic 4MS-EVA response against large strain tests. Cyclic strain values applied are 0.5%, 1%, 2%, and 3%.

Response Time Evaluation

The response time of the 4MS-EVA sensor is evaluated when a strain of 0.1% is applied to it and released with a rate of 900 mm min^{-1}. As shown in Figure 4.13, the equation $y_i = y_{0i} + A_i * exp^{-x/\tau_i}$ is fitted to the instrument data and the sensor response. The extra time constant it takes (in comparison to the time constant of input strain) to respond to applying strain is estimated to be 69 ms. Relaxing back from the peak of strain takes 84 ms (in comparison to input strain). These values are calculated based on the time constant difference ($\Delta\tau$) between the applied or released strain by the instrument and sensor in responding to the input strain. The short response times of the 4MS-EVA sensor enable real-time monitoring of strain in an employed application.

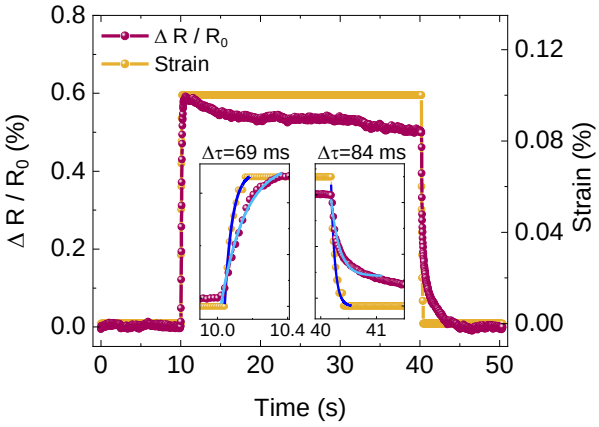

Figure 4.13. Response time evaluation of 4MS-EVA sensor under applying and releasing a 0.1% strain. Insets: a closer look at the fit to the experimental data of instrument and sensor based on $y_i = y_{0i} + A_i * exp^{-x/\tau_i}$.

Since the elastic modulus of EVA is lower relative to the PU substrate, it is important to note that the response time obtained here is largely determined by the elastic modulus of the PU substrate. The elastic modulus of EVA is 2.5 MPa[139] whereas it is 9.6 MPa for our PU substrate. The stress vs strain graph of the PU substrate is shown in Figure 4.14.

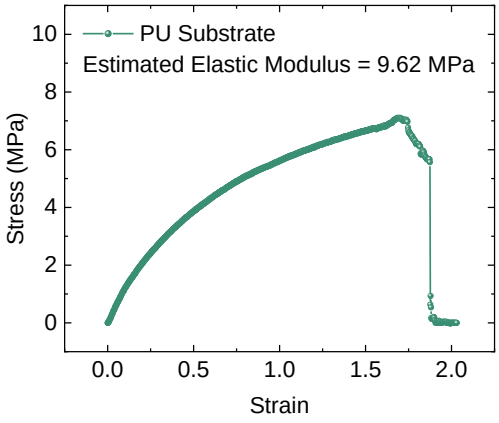

Figure 4.14. Stress vs strain behavior of PU substrate. The estimated elastic modulus of the substrate is 9.6 MPa in the elastic region.

Sensing Mechanism Based on Tunneling Theory

The response mechanism of the 4MS-EVA sensor is evaluated under applying strain up to electrical disconnection when measured resistances reached >10^9 Ohm. Response characteristics of a piezoresistive composite made of nonconductive polymer including a percolated network of conductive particles can be explained using the tunneling theory.[134] Based on this theory (Section 2.1) the experimentally measured $\Delta R/R_0$ is fitted with Equation (4.2). Figure 4.15 shows that the tunneling theory model fits the experimental data and is in good agreement. Table 4.1 lists the fitting parameters.

$$\frac{\Delta R}{R_0} = (1 + A\varepsilon)\exp[(B + AH)\varepsilon + C\varepsilon^2 + D\varepsilon^3 + E\varepsilon^4] - 1 \quad (4.2)$$

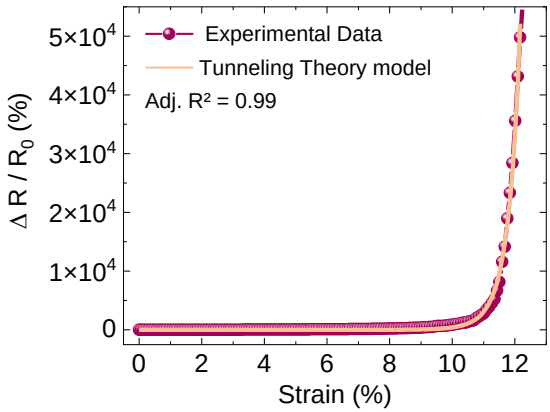

Figure 4.15. 4MS-EVA sensor response mechanism investigation. Experimentally measured relative resistance change of 4MS-EVA sensor, in the electrically

conductive range ($R_{\varepsilon\ max}$ >10^9 Ohm) as a function of strain is fit to the tunneling theory model (Table 4.1).

Table 4.1. Fitting Equation (4.2) to the experimental data in Figure 4.15.

Fitting Parameters	B	C	D	E	A	H
Fitted Values	0.3429	-0.08605	0.02612	-9.66191E-4	0.01261	10.89348

Strain Sensitivity and Working Factor

The strain sensitivity of a piezoresistive stretchable composite, in small strain ranges (in which the cross-section of the active sensing material and its length is not substantially changed)[140], i.e., the gauge factor (*GF*), is defined as Equation (4.3)

$$GF = \frac{\Delta R}{R_0} \cdot \frac{1}{\Delta \varepsilon} \tag{4.3}$$

However, based on Equation (2.11) the piezoresistive response of a stretchable percolative composite to strain has an exponential characteristic. Therefore a more general term to define strain sensitivity is the following Equation.[141,142]

$$\frac{R}{R_0} = \exp(G\varepsilon) \tag{4.4}$$

The strain sensitivity (*G*) of the 4MS-EVA sensor is estimated to be 7 by fitting Equation (4.4) to the linear range of R/R_0 (in the semilogarithmic plot). This indicates a high sensitivity and calibratable response over this range. The working factor of the 4MS-EVA sensor, that is the threshold of linear resistance change,[140,141] is estimated to be 0.067.

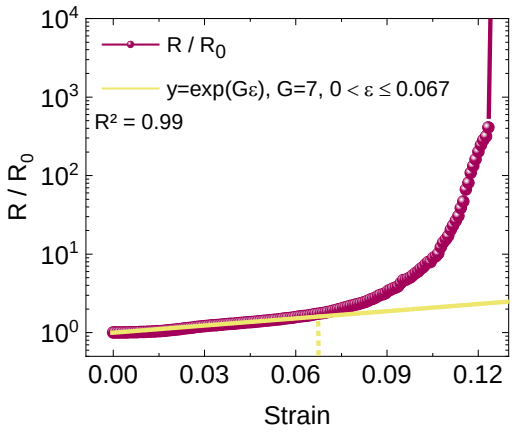

Figure 4.16. Strain sensitivity and the working factor evaluation for 4MS-EVA sensor as a function of applied strain. A strain sensitivity (G) of 7 is estimated by fitting the relative resistance of the sensor to Equation (4.4), in the linear range (in semilogarithmic scale, i.e. $\varepsilon \leq 6.7\%$). The estimated working factor is 0.067.

Durability of Sensor to Large Number of Cycles

The durability and reproducibility of the 4MS-EVA sensor response against 1000 cycles of 1% strain are examined in Figure 4.17. The insets in Figure 4.17 show zoomed-in during three snapshots at the beginning, in the middle, and at the end of these 1000 cycles. A highly repeatable behavior of $\Delta R/R_0$ is observed over the whole range. In the first snapshot, $\Delta R/R_0$ exhibits an ≈8% increase at the peak of strain, and in the last one, it shows a $\Delta R/R_0$ of ≈5%. Overall comparing these three time windows, there is a gradual decrease of $\Delta R/R_0$ over time. The main reason for this behavior can be attributed to the Mullins effect[106] which explains why there is a typical stress reduction in elastomers housing solid conductive particles (Section 2.7.3).

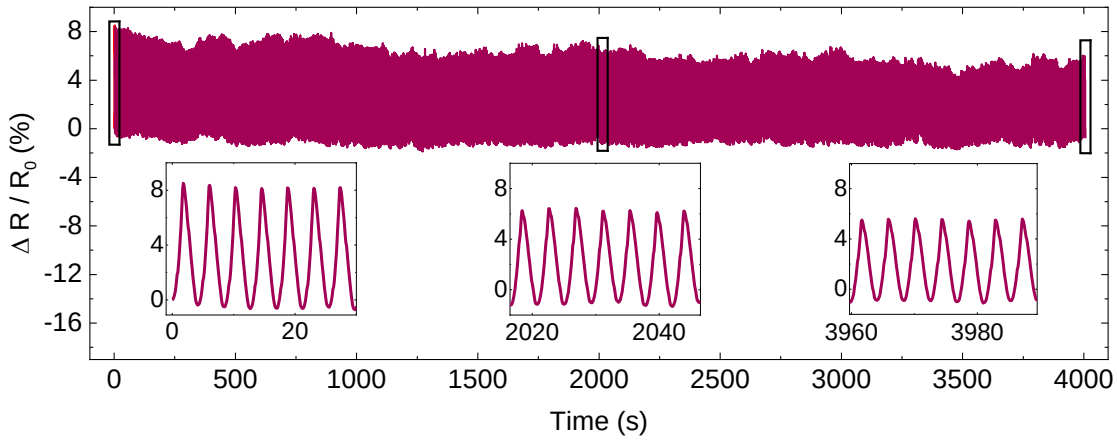

Figure 4.17. Electromechanical durability of 4MS-EVA sensor against 1000 consecutive cycles of 1% strain at a rate of 5% min^{-1}. The inset shows three snapshots that are zoomed in during three spans of the test.

4.6. Sensing Limits Comparison to Literature

As shown in Figure 4.18 the strain sensing characteristics of EVA-microsphere sensors detailed in this chapter (Section 6.1) outperform compared to those of piezoresistive sensors reported in the literature. The detection resolution, minimum detection limit, and response time (Section 6.1) are compared and details are provided in Appendix A4.1, Table A4.1.

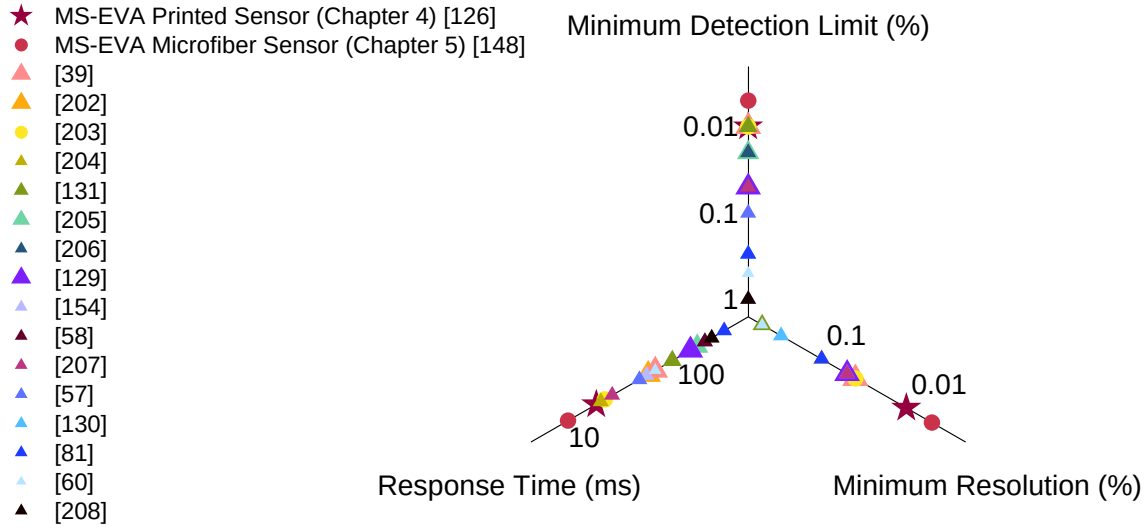

Figure 4.18. The strain sensing properties of the MS-EVA sensors developed in this chapter compared with piezoresistive strain sensors reported in the literature (Appendix A4.1, Table A4.1)

4.7. DC Electric Field-Induced Percolation

4.7.1. Introduction

As discussed earlier in this chapter, the 35MS-EVA sensor compared to the 4MS-EVA sensor, while having a larger percolation threshold ($\varphi_{c\ 35\mu}$ = 20 %, $\varphi_{c\ 4\mu}$ = 16 %), provides a lower minium detection limit ($\Delta\varepsilon_{min\ 35\mu}$ = 0.01%, $\Delta\varepsilon_{min\ 4\mu}$ = 0.015%) and a higher strain sensing resolution ($\varepsilon_{min\ 35\mu}$ = 0.01%, $\varepsilon_{min\ 4\mu}$ = 0.02%). However, these superior sensing properties of 35MS-EVA are achieved at the cost of decreased responsive stretchability (Figure 4.8a). The reduced stretchability in 35MS-EVA is mainly ascribed to the large size of the solid particles and the relatively high volume ratio required to reach the percolation threshold, interrupting effective polymer chain rearrangement under strain. One effective approach to further lower the percolation threshold, or in other words, the amount of particles required to create conductive paths, is to direct the assembly and agglomeration of the particles in the elastomer matrix by applying an external electric field.[125,143] The anisotropically dispersed filler provides anisotropic functionality in the conductive polymer composite which can be used for a variety of applications such as asymmetrical strain sensing,[143] pressure mapping in wearable sensors,[144] thermal conductive interface for heat sink,[145] and z-direction conductive film for electrical interconnects.[146]

In this section, we examine the influence of externally applied DC electric field at low voltages (< 50 V) on decreasing the volume fraction of 35 µm conductive microspheres required for the electrical percolation. Dynamic percolation is simultaneously electrically and morphologically investigated using dynamic two-probe resistance measurements using an SMU and OM.

4.7.2. Dynamic Percolation Threshold Investigation

The microspheres are manually dispersed in a viscous polymer solution of EVA and anisole, as the elastic polymer and a non-toxic solvent, respectively. The prepared paste is screen-printed onto the screen-printed silver electrodes, using stencil printing on a substrate (more details on the sample preparation are presented in Section 3.2.3). The experiment procedure

of the dynamic percolation investigations is shown in Figure 4.19a and Figure 4.19b. A DC source voltage of different strengths (< 50 V) is applied to the printed wet layer using a SMU. The schematic in Figure 4.19d illustrates the cross-section of the layer under the DC-electric field. As discussed in Section 2.8, conductive core-shell (glass core, silver shell) microspheres dispersed in a liquid medium (ethylene vinyl acetate mixed in anisole) obtain a double-layer surface charge. Due to the presence of this layer on and around the microspheres in the medium, when an electric field is applied to the two electrodes, on the one hand, several forces attract the microspheres towards the electrodes which are the electrophoresis force, the chain force, and the dielectrophoretic force. On the other hand, under the DC electric field, the viscous polymer-solvent mixture at the vicinity of the substrate and electrode obtains counter-surface charges. These charges screen the induced charges on the microspheres exerting a frictional force on the microspheres which is called the hydrodynamic drag force which is described in Section 2.8. The sum of these forces results in microspheres migrating towards the electrodes, aligning in the direction of the electric field that is formed between the two electrodes.[121]

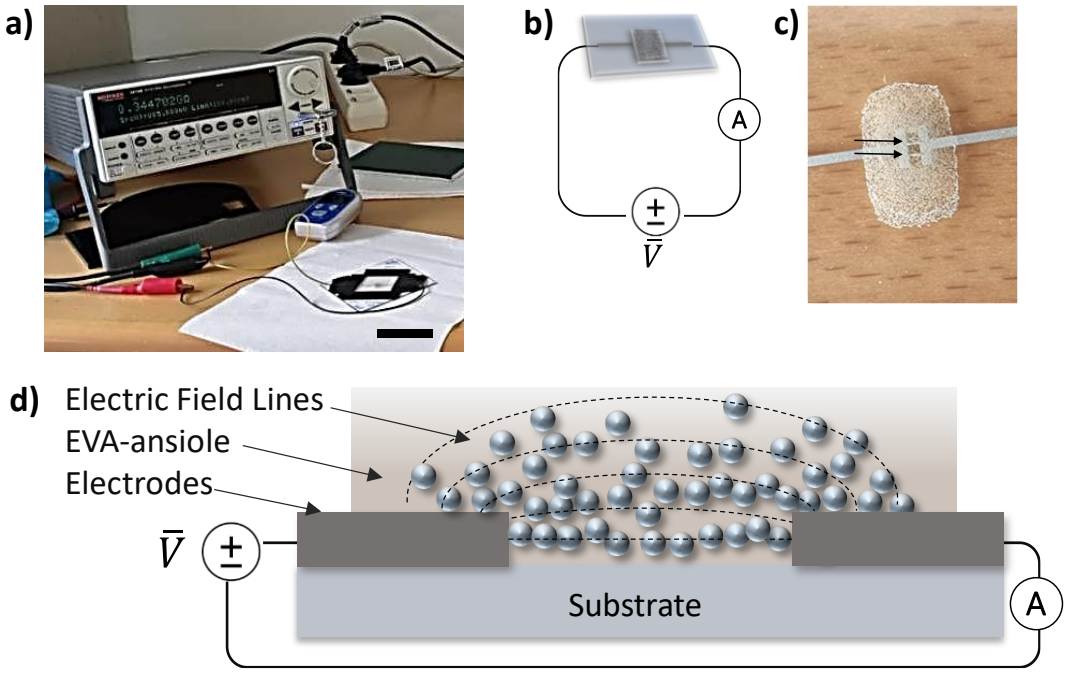

Figure 4.19. Schematics and experimental procedure of dynamic percolation threshold investigations. a) Photo of the DC electric field applying experiments.

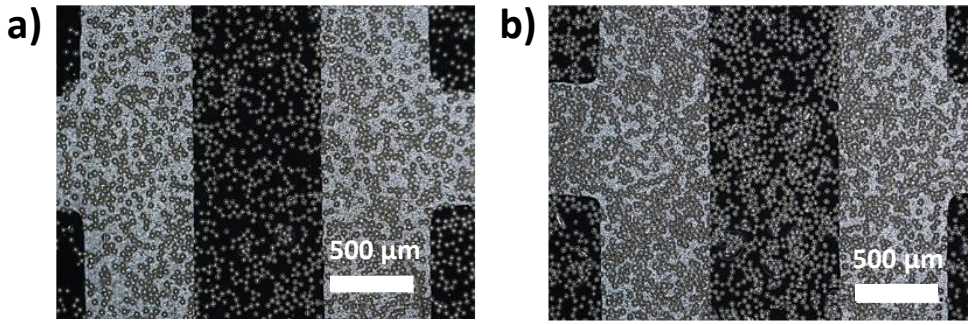

Figure 4.20. OM images of the printed layer in the absence of electric field (E_0), a) bellow the percolation threshold at 15 vol.%, and b) at the percolation threshold at 33 vol.%. b) Schematic illustration of the printed layer under DC electric field. c) Digital photo of the electric-field driven percolation in a 35MS-EVA composite. Two regions in the composite exhibit two linear agglomerates visible to the naked eye (the two black arrows point toward the two linear particle assemblies). d) Cross-section schematic of the electric-field driven percolation by applying DC electric field (schematic not to scale).

A photo of the printed layer after the electric-field-assisted percolation is shown in Figure 4.19c. The formed linear-shaped clumps of particles can be observed. In the presented example, two linear agglomerates perpendicular to the electrodes and inline with the direction of the applied electric field are formed.

4.8. In-situ Observation of Percolation Under DC Electric Field

The in-situ changes in the microstructure of the printed layers under different DC electric field strengths are investigated by tracking the real-time video and photos under an OM. The percolation theory, as described in Section 2.1, defines the relationship between the volume fraction of conductive fillers and the electrical conductivity of the composite. The OM image in Figure 4.20a shows a layer at φ_0 = 15 vol.% (well below the percolation threshold) in the absence of an electric field (at E_0). Here, randomly distributed microspheres are mostly isolated from one another in the EVA matrix, resulting in an electrically disconnected composite. Figure 4.20b at E_0, shows a percolated layer (φ_{c0}=33 vol.%) where agglomerated particles create conductive paths. In the following sections, the results of experiments for

lowering the percolation threshold by applying a DC electric field are discussed. Figure 4.21a shows the OM image of the printed layer at 20 vol.% (below percolation threshold). When an electric field of 25 V μm^{-1} (Figure 4.21b) is applied to the wet layer, microspheres form linear agglomerates. These agglomerates are parallel to the direction of the electric field between the electrodes and perpendicular to the electrodes.

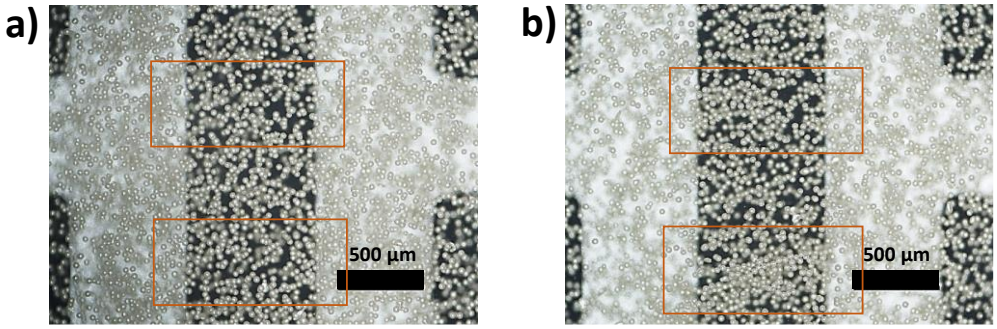

Figure 4.21. OM images of the printed layer (in wet state) having 20 vol.% microspheres a) before and b) during applying a 25 V μm^{-1}. Comparing the same regions in a with b, indicated by the orange frames, shows linear-shaped agglomerates are formed in line with the direction of the applied electric field.

As explained in Section 2.7, the reason behind the chain-like structures is ascribed to the formation of a double layer of surface charge around the microspheres and on the substrate and electrodes. The interaction of these layers, under the applied electric field (i.e. electrophoretic force, Section 2.8.1) triggers the movement of microspheres toward the electrodes. Additionally, conductive microspheres under the application of an electric field obtain an induced dipole moment that points along the direction of the electric field in the surroundings (Section 2.8.5). As the first microsphere is connected to one of the electrodes, it changes the distribution of the electric field inside the medium (Figure 2.5), resulting in a gradient of the electric field. This gradient enhances the attractive forces being applied to microspheres by enhancing dipole-dipole interactions and putting the dielectrophoretic force and the chain force into action. Subsequently, a linear agglomerate of microspheres starts to form a chain. This chain formation continues until the two electrodes.

Further Lowering the Percolation Threshold and Electric Field Strength

It is known that the formation of conductive paths in a composite is a process-dependent phenomenon.[116] Based on Equation 2.19 (Section 2.8.2), mobility is inversely proportional to the viscosity of the medium. Due to the surface evaporation of the solvent, the viscosity of the solution increases, therefore, increasing the surface tension. In our case, this phenomenon causes hindrance to the movement of microspheres.[147] Therefore, to further lower the percolation threshold achievable using the same 25 V μm^{-1} electric field, the rate of solvent evaporation is slowed down (at room temperature). In doing so, and to lower the airflow on the printed layer while applying the electric field, immediately after stencil-printing of the paste, a 500 µl anisole droplet is placed on the glass slide near the sample. The sample and the anisole droplet are covered with a petri dish. Therefore, it keeps a favorable wet state for the printed layers long enough to allow for electric-field-driven network formation and in-situ dynamic percolation investigations. As shown in the OM images in Figure 4.22, a 25 V μm^{-1} electric field successfully creates linear agglomerates in a layer having as low as 15 vol.% microspheres (indicated by the orange frames). Furthermore, using the above-mentioned method, conductive network formation at 20 vol.% is achieved using an 18 V μm^{-1}. This finding indicates to create a conductive layer having 20 vol.%, instead of applying a 25 V μm^{-1} electric field (which was the case in Figure 4.21, without lowering the solvent evaporation rate), a lower electric field of 18 V μm^{-1} can be applied if the solvent evaporation is lowered and the printed layer stays wet for a longer time.

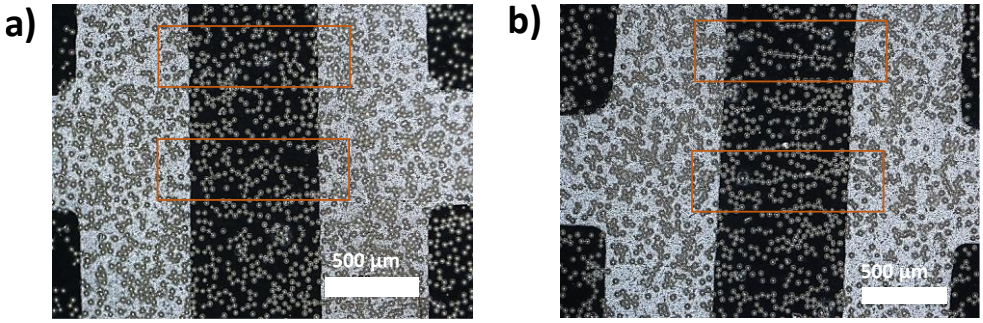

Figure 4.22. OM images of the printed layers having 15 vol.% a) before applying the electric field and b) after applying 25 V μm^{-1}. A small droplet of anisole is placed near the printed layer, and a glass petri dish is placed on top of the printed layer and the droplet to lower the airflow and slow down the anisole evaporation rate. Comparing the same regions in the orange frames indicates chain-like agglomerates

are formed in between electrodes, in line with the direction of the electric field (scale bar 500 µm).

Based on the discussions detailed in Section 2.8, as electric field strength increases, the forces attracting the microspheres towards the high-intensity regions, which are electrodes, increase. This is the reason why a higher electric field strength results in a lower percolation threshold. Thus, to further lower the percolation threshold, the strength of the electric field is increased up to 38 V μm^{-1}. This yields a very low percolation threshold of 10 vol.%. However, instead of linear filament formation between the electrodes, clumps of dune-shaped agglomerates are formed. An example of a couple of large dune-shaped agglomerates in a layer with 25 vol.% is shown in Figure 4.23.

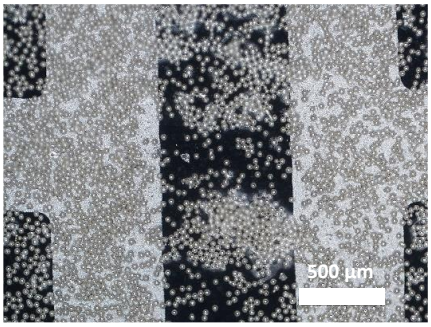

Figure 4.23. OM images of a printed layer having 25 vol.% when a 38 V μm^{-1} electric field is applied. Microspheres Clumped with dune-shaped agglomerates are formed between electrodes (scale bar 500 µm).

In Figure 4.24, the result of percolation threshold investigations and lowering it by slowing down solvent evaporation is shown. Data shows the mean normalized conductivity vs volume fraction of 10 samples per data point. An electric field of either 0, 18 V μm^{-1}, or 25 V μm^{-1} is applied to the samples which are plotted in purple, orange, and green, respectively. A percolation threshold of 19% is achieved using an 18 V μm^{-1} electric field, and a percolation threshold of 14% is achieved using a 25 V μm^{-1} electric field.

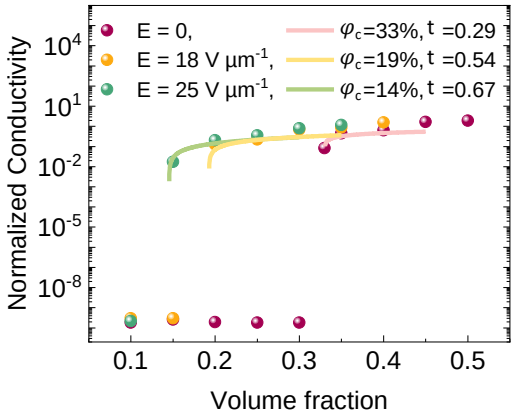

Figure 4.24. Percolation threshold investigations. The normalized mean of conductivities measured in the absence of the electric field is plotted in dark-red circles, under an electric field of 18 V µm^{-1} in orange circles, and an electric field of 25 V µm^{-1} in green circles. The percolation thresholds estimated are 33 vol.% at E = 0, 20 vol.% at E = 18 V µm^{-1}, and 15 vol.% at E = 25 V µm^{-1}.

Figure 4.25 presents a summary of electrical conductivity measurements of all performed experiments. The solid triangle sign means the layer is conductive and the × sign means the layer is disconnected. Under the application of an electric field of either 0, 18, 25, or 38 V µm^{-1} a conductive layer can be formed at 33, 20, 15, or 10 vol.%, respectively. A further increase of the electric field to values higher than 38 V µm^{-1} causes observable Joule heating.

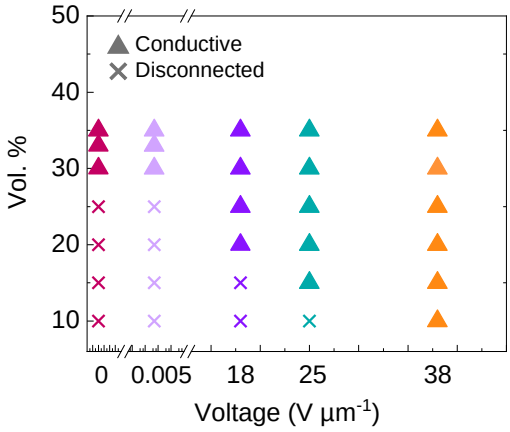

Figure 4.25. Summary of electrical conductivity investigations after optimizing solvent evaporation. Cross sign (×) presents electrically disconnected layers (R >10^9 Ohm) and solid triangle ones the conductive layers.

4.8.1. Decreasing the Percolation Time

The discussions detailed so far implicate clearly that, percolation is not only a process-dependent phenomenon but also a time-dependent one.[116] Meaning percolation depends also on the duration that the layer is exposed to specific processing conditions. For our case for example lowering the solvent evaporation or letting the uncapped printed layer rest for a longer time instead of immediately drying it (Section 3.2.3) have shown to be effective ways to lower the percolation threshold. In Figure 4.26 the percolation time, defined as the time when the first conductive path is formed, is investigated. After a certain amount of time resistance of the layer undergoes a sharp decrease from disconnected values (>10^9 Ohm) down to conductive ranges (here <10^6 Ohm).

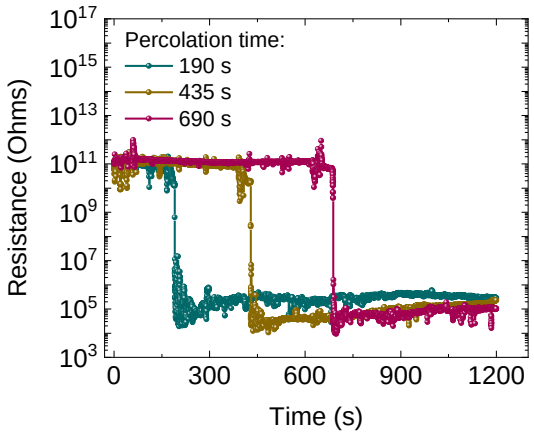

Figure 4.26. Percolation time investigations. Magenta color data shows the resistance changes of a layer to which an electric field of 18 V µm^{-1} is applied (at t = 0) where percolation occurs at 690 s. The mustard color plot presents the resistance change of a printed layer to which the same electric field of 18 V µm^{-1} is applied. However, the solvent evaporation of this layer is lowered where the percolation time is reached at 435 s. The teal color plot shows the resistance change under a 25 V µm^{-1} electric field. The solvent evaporation of this layer is also lowered. Here an increase in electric field strength further reduced the percolation time to 190 s.

The plot in magenta color shows the percolation time of 690 s for a layer under 18 V µm^{-1} without capping it. By reducing the solvent evaporation rate using the cap, under the same electric field, the percolation time is decreased to 435 s (mustard data). To further lower the percolation time, the electric field is increased to 25 V µm^{-1}, yielding a percolation time of 190 s (teal data). This graph shows that the percolation time required for microspheres-

directed assembly highly depends on the electric field strength and the solvent evaporation rate. The reason behind the decreased percolation time from 690 s to 435 s is attributed to the decrease in solvent evaporation rate. Decreasing from 435 s down to 190 s is ascribed to the increased electric field which in turn increases the forces contributing to the formation of filamented structures.

4.9. Summary

In conclusion, this chapter presented the development of a piezoresistive strain sensor material using all-scalable printing methods. Conductive core-shell microspheres, as active sensing elements were dispersed in an elastomer. As the stretchable part, EVA was compared with PDMS in terms of electrical percolation threshold, morphological differences of the interface with microspheres, and electromechanical characteristics of the sensors. Overall the percolation threshold of the sensors made with EVA is lower and the electromechanical performance of the EVA-based sensor under cyclic tensile strain test is more promising with less hysteresis. The reason behind the observed differences in percolation and better performance of EVA-based sensors is attributed to the difference in the morphology of the interface. Choosing EVA over PDMS, as the elastomer, the electromechanical performance of the EVA-based sensor was further investigated. Using 35MS, a very low detection limit of 0.01% was achieved. However as strain increases to 0.2%, hysteresis-related effects grow. A reason for the poor performance of the 35MS-EVA sensor is attributed to the large size of the solid fillers. Using 4 µm microspheres, a low detection limit of 0.015% was achieved alongside a high resolution in the detection of 0.025% strain change. The response mechanism of the piezoresistive sensor was explained using the percolation theory and a strain sensitivity of 7 in a working range of 0.067 strain was estimated in the (semi-logarithmic) linear region. The response time of the sensor under the straining instrument was estimated to be 69 ms and electromechanical durability of the sensor response to 1000 cycles of 1% was shown.

Further, we aimed to lower the percolation threshold of 35MS-EVA by applying a DC electric field. In our optimized sample condition, a low DC electric field of a maximum of 18 V μm^{-1} could effectively produce filamented networks of the conductive core-shell

microspheres with a volume fraction ($\varphi_{c,E}$ = 20%) well below the percolation threshold in the absence of the electric field ($\varphi_{c,0}$ = 33%). Therefore, the electrical percolation threshold can be effectively lowered by applying a low DC electric field. To maintain the viscosity of the printed layer and prevent its increment while the electric field is being applied (due to solvent evaporation), the solvent evaporation is decreased by placing a droplet of the solvent and capping the layer. Using this method, the electric field required for the same percolation threshold is lowered, and the percolation time is decreased. Therefore, overall the percolation threshold of 35MS-EVA can be effectively lowered by applying an electric field to the layers right after printing. To further lower the percolation threshold, a decrease in the solvent evaporation rate is shown to be an effective approach. To further reduce the percolation time in future studies, apart from increasing the electric field strength, the solution mixture viscosity can be modified by lowering the elastomer concentration in the solvent. The obtained percolation threshold of 20 vol.% for 35MS-EVA by applying an electric field of 18 V μm^{-1} is desirable for the future development of high-precision directional strain sensors.

5. Free-standing Microfiber Strain Sensor

In this chapter, a substrate-free microfiber sensor made of EVA and conductive core-shell microspheres is developed. A scalable wet-spinning method is used for the fabrication of the stretchable microfiber. The transformation of a viscous paste containing EVA, anisole, and microspheres into a cylindrical-shape is described. The microstructure of the microfiber fabricated using either 4 µm or 35µm microspheres is investigated using OM and SEM. Focusing on 4 µm microspheres (4MS), percolation threshold investigation of 4MS containing microfiber is discussed. Mechanical characteristics of the pristine elastomer microfiber are compared with microfiber including microspheres under similar tensile strain tests. Microfiber, having connected electrodes, is further examined under electromechanical tests. Based on the tunneling theory, the general response of the sensor over the entire conductive range is described. The strain sensitivity of the 4MS-EVA microfiber sensor is compared with that of 35MS-EVA. Although the strain sensitivity of the 35MS-EVA sensor is higher than the 4MS-EVA sensor, its workable range is lower. Hence, to realize a larger working range, further electromechanical properties of the 4MS-EVA microfiber are investigated such as minimum strain detection limit and minimum strain resolution. The minimum detection limit and minimum resolution reported in this work are compared with piezoresistive strain sensors in the literature. The reproducibility of the sensor is examined under repetitive cyclic stain and its response time is estimated. Electromechanical durability to overload strain and large number of cycles is presented. The results presented in this chapter have been previously published as a journal article in Advanced Materials.[148]

5.1. Introduction

The substrate-free fiber-shape sensors offer several advantages compared to the other forms of SPC sensors deposited on a substrate. Foremost, the high conformability in a fiber sensor allows easier access to irregular and intricate structures. Additionally, in applications where high precision in small strain sensing is the focus, a substrate-free sensor provides improved resolution and response time compared to a sensor deposited on a substrate. A fiber-shape stretchable strain sensor is commonly based on a composite of an electrically insulating elastic polymer (e.g. PDMS[52,55] or thermoplastic polyurethane[38,59]) and a conductive material (carbon nanotubes[38,39] or graphene[46,47]). When tensile strain is applied to such a sensor, the mechanical deformation stretches the elastomer resulting in slight displacement of the conductive constituents, hence causing an increase of resistance of the sensor, that is piezoresistivity. Although there are numerous reports around ultra-stretchable fiber strain sensors ($\varepsilon_{max} \geq 100\%$),[38,43,59,77,79] typical SPC fiber sensors introduced so far are reliable and functional in large strain ranges with an insufficient detection limit for subtle strain sensing ($\varepsilon_{min} > 1\%$).[38] For small strain sensing applications, high resolution and reliable detection of micrometer thickness changes are of high priority. There is a subgroup of highly sensitive fiber strain sensors the limit of detection of which is $\varepsilon_{min} \geq 0.1\%$.[34,62,80–82] There has also been extensive work on increasing the stretchability or sensitivity of the fiber strain sensors.[34,131,149,150] However, most reported works lack high resolution and sensitivity for smaller strains ($\varepsilon < 0.1\%$). Overall, fiber-based strain sensors prepared with economic and facile methods yielding reasonable stretchability, a very small detection limit ($\varepsilon_{min} < 0.1\%$), and high resolution in detecting very small strain changes are lagging.

In this chapter, using wet-spinning as an industrially relevant scalable method, a novel microfiber consisting of uncommon silver-coated glass microspheres and EVA is introduced. This fabrication approach eliminates the need for a substrate, therefore canceling out the unwanted substrate effects such as hysteresis. The developed microfiber is investigated in terms of microstructure morphology. Under mechanical tests, the effect of incorporating microspheres in the elastomer is examined. Moreover, in this chapter instead of the common approach in the literature to have a secondary conductive material,[42,52–54] one type of conductive particle (conductive microspheres) is chosen as the active sensing element. An outstanding high resolution of 0.005% strain change detection and linear response over the whole working range, from 0.005% strain up to 14%, is achieved.

Additionally, the strain sensing mechanism is described based on the tunneling theory and thereupon a high strain sensitivity is estimated. The delay in response time of the sensor during stretching is estimated to be 11 ms and reproducibility of the sensor response over fast cycling rate is presented. Moreover, retrieved electrical conductivity under overload strain is presented as well as durability to 10,000 cycles of 1% strain. Lastly, the sensing properties of the developed microfiber are compared to that of the piezoresistive strain sensors in the literature. This comparison indicates, to the best of our knowledge, that the minimum detection limit and the minimum (strain difference) detection resolution are the lowest among the reported works.

5.2. Fabrication and Structure of Microfiber

For the fabrication of the free-standing microfiber sensor, the wet-spinning method shown in Figure 5.1a is used as a facile and scalable method (Section 3.2.43.2.4).[38,62,77] Here, EVA, as the elastomer matrix is dissolved into anisole as a non-toxic solvent. Then the 4 µm silver-shell glass-core microsphere powder is mixed into the EVA-anisole solution. Via a nozzle, the prepared spinning solution mixture is dispensed into the acetone bath, as the non-solvent. The choice of anisole as the solvent and acetone as the non-solvent is based on the analysis of the Hildebrand-Hansen solubility parameters and the relative energy differences of EVA-anisole and EVA-acetone (Section 2.5). The Hildebrand Hansen solubility parameters of EVA copolymer are estimated based on Equation 5.1 and the Hildebrand-Hansen solubility parameters of the polyvinyl acetate (PVA) and the polyethylene (PE) homopolymers, and the weight ratio of the two in the corresponding EVA (W_i).[94,96]

$$\delta_{i\ EVA40} = \delta_{i\ PVA} W_{PVA} + \delta_{i\ PE} W_{PE} \tag{5.1}$$

Where $W_{PE} = 1 - W_{PVA}$, W_{PVA} is the weight ratio of the vinyl acetate in EVA copolymer, and $\delta_{i\ EVA40}$ is the corresponding Hildebrand-Hansen solubility parameter of EVA. In Table 5.1 the calculated Hildebrand-Hansen solubility parameters of EVA and the relative energy differences are summarized.[96,151]

Table 5.1. The summary of the analysis of the Hildebrand-Hansen solubility parameters of constituent solutes and solvents in the spinning solution and the calculated relative energy difference for EVA.[96,151]

Material	$\delta_D(MPa)^{1/2}$	$\delta_P(MPa)^{1/2}$	$\delta_P(MPa)^{1/2}$	$\delta_i(MPa)^{1/2}$	*RED*
PE	14.84	-3.88	1.78	15.44	-
PVA	19.45	10.59	5.76	17.91	-
EVA[a]	16.68	1.91	3.37	17.13	0.601[b] [96]
Anisole	17.8	4.1	6.7	19.4	-
Acetone	15.5	10.4	7.0	20.3	1.236

Based on Table 5.1, for EVA used in this thesis, based on the weight ratio content of ethylene and vinyl acetate homopolymers, we calculate the RED for a compound of EVA copolymer and anisole to be ~ 0.6 (for solubility parameters and RED calculations see Section 2.5).[96,151] The RED of 0.6 means the anisole has close-enough physical composite affinity parameters with EVA, indicating the solubility of the EVA in the anisole. Additionally, since anisole and acetone have similar solubility parameters (Table 5.1), they are miscible. This is essential for the choice of the coagulation bath. For a mixture of EVA and acetone the calculated RED is 1.26, indicating that acetone is a non-solvent for EVA. Therefore, in this work acetone is chosen as a favorable non-solvent for the coagulation bath.[95,96,151]

[a] EVA solubility parameters are calculated from Equation (5.1).
[b] The RED of the EVA40 with anisole and acetone is calculated based on R0 = 7.71, Equation (5.1), and Hildebrand-Hansen solubility parameters of PVA and PE as given in Table 5.1.

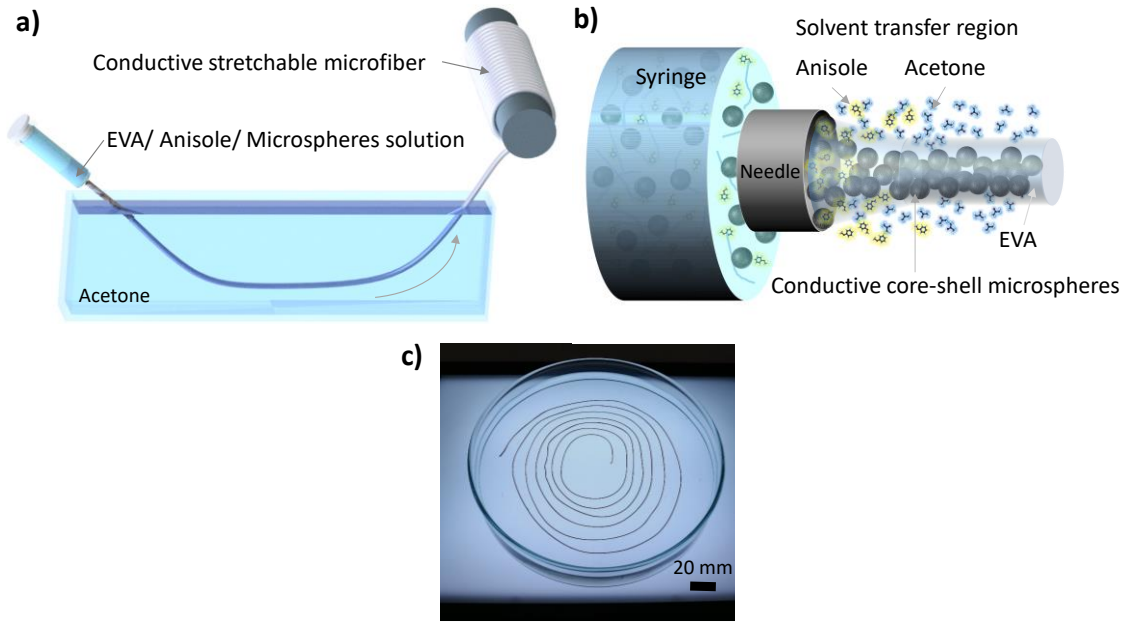

Figure 5.1. Fabrication method and structure of the free-standing stretchable microfiber strain sensor. a) Schematic of the wet spinning constituents. A viscous solution mixture of EVA, anisole, and conductive microspheres is dispensed in the acetone bath. b) Schematic illustration of the solvent interchanges in the non-solvent bath. The spinning material densifies and a gel-like material is formed during the extrusion. c) Digital photo of the extruded (2 m long) microfiber resting in the acetone bath.

When the solution mixture is dispensed into the non-solvent bath, as shown in the schematic in Figure 5.1b (in the solvent transfer region), due to the net random molecular motions towards low concentration regions in the bath, the counter diffusion between anisole and acetone molecules takes place.[152–154] Anisole is removed from the EVA solution moving outward and being exchanged with acetone which diffuses inward to the EVA solution rendering decreased solubility of the EVA. Therefore, the EVA starts to gelify first at the areas where it is in closest contact with the non-solvent bath.[77,155,156] Over the course of coagulation, the gel-boundary between EVA and bath moves inwardly to the center of the spinned material. This process continues until all the EVA in the extruded material is deprived of anisole and hence is densified. Therefore, under the influence of the shear force applied by the spinneret capillary and due to a series of diffusional interchanges between the anisole and the non-solvent acetone bath, a spinning solution mixture is transformed into a cylindrical fiber shape. Additionally, to form a long fiber, we exert an additional shear force on the spinning material by moving the nozzle in the bath in a circular path (Figure 5.1c). The two shear forces applied to the material[157] yield a condensed and homogenously

cylindrical microfiber having a meter length. The microfiber stays in the non-solvent bath for three minutes to let the solvent interchange be completed and the polymer fully coagulated. This fabrication method is conveniently scalable for the mass production of microfiber strain sensors for industrial applications.

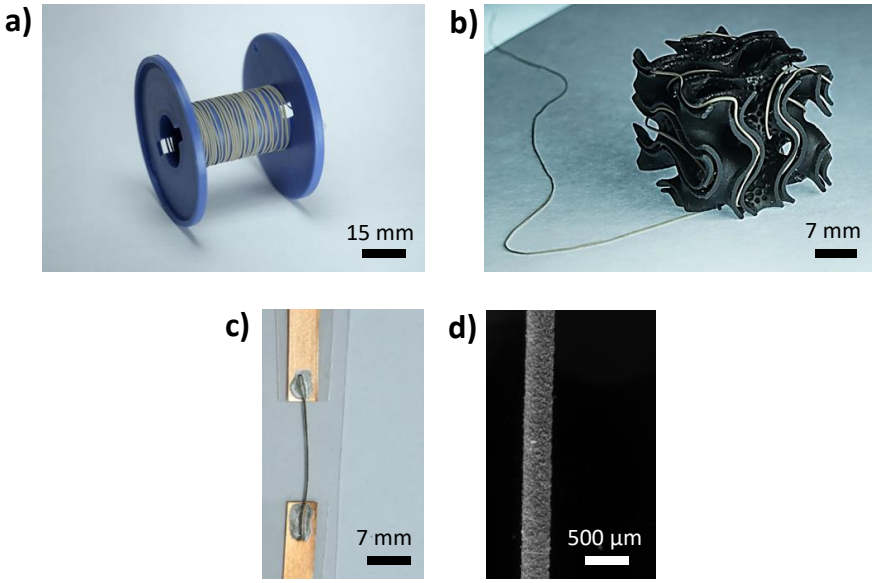

Figure 5.2. Structure of the free-standing stretchable microfiber strain sensor after the wet-spinning. a) Digital photo of the spooled two-meter microfiber. b) Digital photo of the microfiber assembled throughout a curved (3D-printed) object. c) Digital photo of the microfiber prepared for electromechanical tests (with coper-tape and silver lacquer electrode contacts attached at the two ends of it). d) OM image of the microfiber.

After the coagulation time, the free-standing microfiber is drawn out of the non-solvent bath and spooled (Figure 5.2a), then dried at room temperature under vacuum, to remove the acetone residue inside. As shown in Figure 5.2a, to demonstrate the conformability of the developed microfiber, it is assembled around and into a curved 3D-printed structure, exhibiting its high conformability and potential for strain sensing in intricate applications with detailed form factors. The developed microfiber strain sensor with attached electrodes as shown in Figure 5.2c can be used for electromechanical characterizations. The OM image of the lightweight microfiber (0.133 mg mm^{-1}) in Figure 5.2d displays the cylindrical form of the microfiber strain sensor used in this work with a diameter of 330 µm ±10µm.

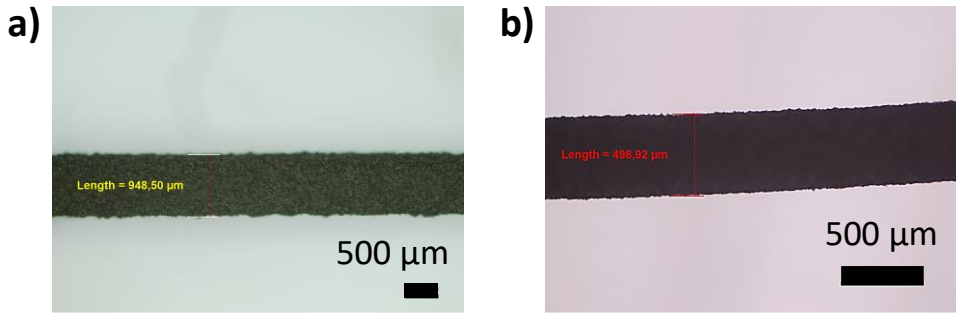

Figure 5.3. The diameter of the microfiber is controlled by the wet-spinning parameters. a) OM image of the microfiber fabricated by a needle gauge of 17 (inner diameter of needle 1070 µm) and wet-spinning rate of 50 mm s^{-1}. b) OM image of the microfiber fabricated by a needle gauge of 18 (inner diameter of needle 840 µm) and a spinning rate of 70 mm s^{-1}.

The diameter of the microfiber can be tuned from 300 µm up to 1000 µm, according to the wet-spinning parameters, i.e. the nozzle gauge (or in other words the inner diameter of the nozzle), the weight ratio of EVA to anisole, and the wet-spinning rate. For example, a nozzle gauge of 17 (inner diameter of needle 1070 µm) and a wet-spinning rate of 50 mm s^{-1} results in a microfiber diameter of 950 µm, as shown in Figure 5.3a. Another example is where a nozzle gauge of 18 (inner diameter of needle 840 µm) and a wet-spinning rate of 70 mm s^{-1} are used which results in a microfiber with 490 µm diameter, as shown in Figure 5.3b. In this work, microfibers with 330 µm ± 10 µm diameter are fabricated by a nozzle gauge of 18 and a spinning rate of 50 mm s^{-1}.

5.3. Microstructure Morphology

As illustrated in Figure 5.4a (left), within the microfiber, conductive paths are formed through a percolated network of conductive core-shell microspheres, with minimal contact due to the spherical shape of particles Figure 5.4a (right). The microstructure of the microfibers is studied by SEM images. In Figure 5.4b the SEM cross-sectional image shows the compact and cylindrical structure of the developed microfiber. The SEM image in Figure 5.4c displays the percolated cluster of conductive microspheres with an average diameter of 4 µm formed in the EVA matrix. A further enlarged SEM image in Figure 5.4d shows the smaller features of the nanoscale silver coating on the glass core.

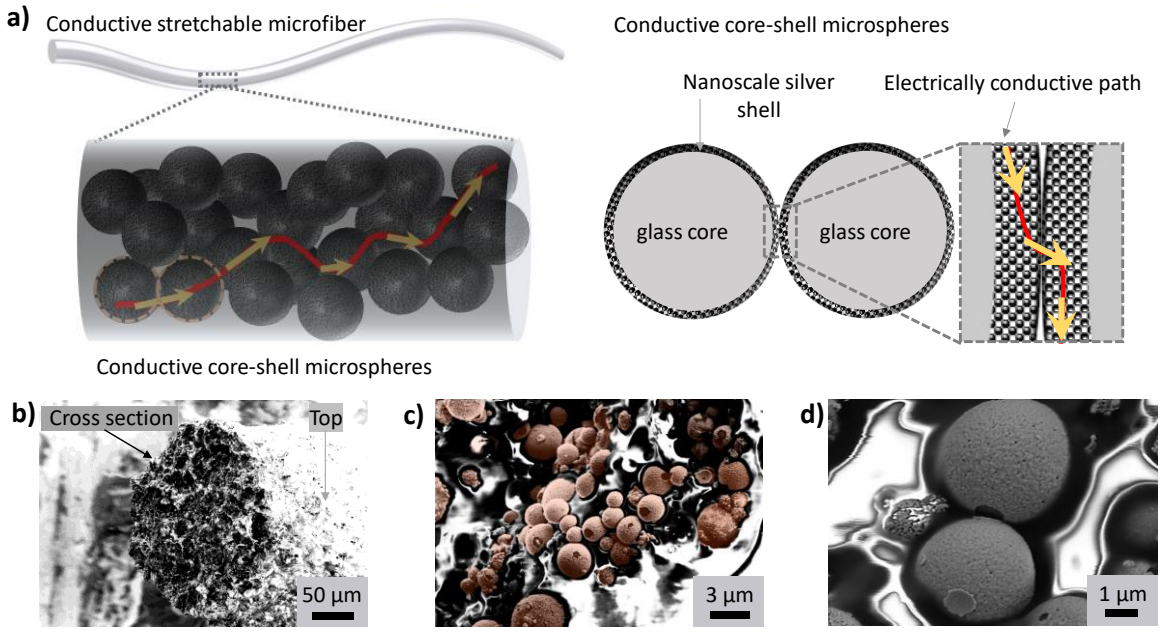

Figure 5.4. Microstructure of the 4MS-EVA microfiber strain sensor. a) Schematic of the microfiber (not to scale) depicting the formation of an electrically conductive path by percolated microspheres and the minimal contact interface between them. b) Cross-sectional SEM image of the microfiber. c) Magnified cross-sectional SEM image of conductive core-shell microspheres (colored orange digitally). d) SEM image of microspheres with a nanoscale silver coating (with an average thickness of 50 – 80 nm).

5.4. Percolation Threshold

In Figure 5.5, the normalized mean conductivity of the developed 4MS-EVA microfibers (containing EVA and 4 µm microspheres) as a function of different volume fractions of microsphere to sensing material is plotted (single data points). Based on the percolation theory of Kirkpatrick (Section 2.1) the conductivity vs volume ratio behavior of a composite of conductive particle and insulating elastomer can be defined by a power law relationship as $\sigma/\sigma_0 = (\varphi - \varphi_c)^t$. In Figure 5.5 the fit to the conductivity data based on the percolation theory is plotted by the solid line. The percolation threshold of 4MS-EVA microfibers, where there is a shift from electrically disconnected to conductivity, is estimated to be 13 vol.%. Considering the volume ratio of the silver shell to the total sensing material (EVA, the spherical insulating core, and the spherical silver shell), a very low percolation threshold of 1.9 vol.% is achieved. For the fabrication of the 4MS-EVA microfiber sensors, to make sure the electrical response is repeatable, a microsphere to elastomer volume fraction of 20% (slightly above the percolation threshold) is chosen. Using a further higher volume fraction,

by increasing conductive particles in the matrix, is known to have an adverse effect on the stretchability of the composite.[72]

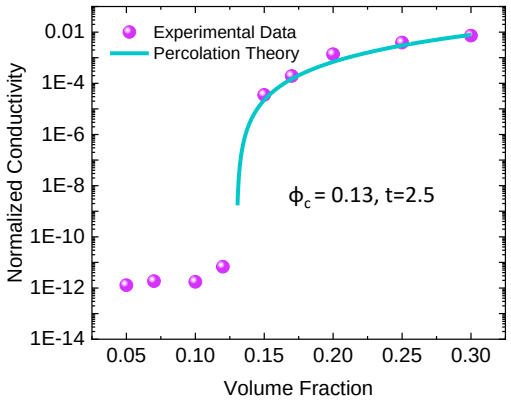

Figure 5.5. The mean of normalized conductivity of 4MS-EVA microfibers as a function of the volumetric ratio of microsphere to the sensing material.

5.5. MS-EVA Interface

The electrical response of the stretchable conductive microfiber is strongly correlated to the changes in the mechanical characteristics of the elastomer matrix as a result of solid microsphere inclusion. In this work, EVA as an economic and advantageous copolymer consisting of physically cross-linked vinyl acetate and ethylene polymer chains (40 wt.% vinyl acetate) is used as the stretchable polymer. To investigate the interface that EVA makes with the microspheres, the SEM images are examined. In Figure 5.6a the 4MS-EVA microfiber is displayed in the relaxed state, and Figure 5.6b when the same microfiber is under a tensile strain. To gain more insights into the particle-polymer interface in Figure 5.6c and Figure 5.6d the SEM images of the 35MS-EVA microfiber under strain are shown. The observations suggest that EVA forms a loosely attached layer around the microspheres. The weak bond between the EVA and microsphere is ascribed to stem from the weak Van-der-Waals forces between the silver shell and the polar and mobile vinyl acetate chains. These chains are the main reason why EVA is highly stretchable and rubbery. Additionally, it is important to note that since EVA is already polymerized, its semi-crystalline ethylene chains and amorphous vinyl acetate chains cannot form a strong bond with the silver shell, as compared to PDMS, as discussed in Section 4.2.2. Forming a blanket-type cover around the microspheres promotes the formation of a percolated network of agglomerated

microspheres. Hence, resulting in a lower percolation threshold, compared to a chemically cross-linked polymer.[158]

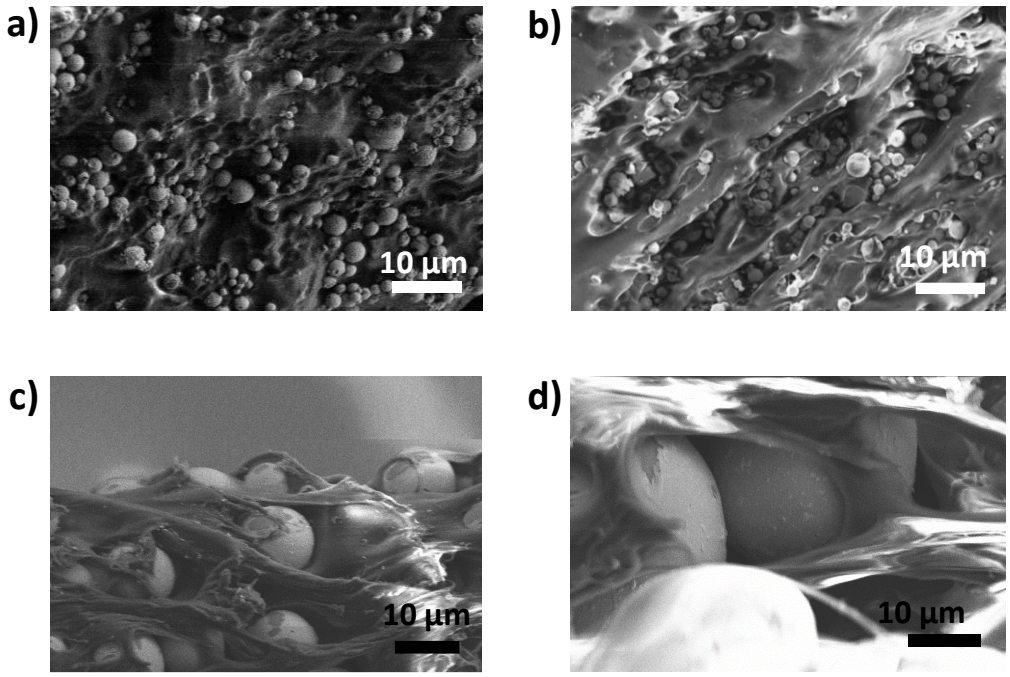

Figure 5.6. SEM images to investigate the EVA-microsphere interface. a) SEM image of the 4MS-EVA in a relaxed state, and b) under a tensile strain of 70%. c) and d) SEM images of the 35MS-EVA microfiber under a tensile strain of 30%.

5.6. Microfiber Prepartion for Mechanical and Electromechanical Tests

In this work the active sensing length of the microfiber sensor is 20 mm. The two-meter-long microfiber (after drying) is cut into 25 mm pieces to allow for an active sensing length of 20 mm and an excess of 5 mm for the electrode connections. For the mechanical and electrical characterizations, to facilitate the contacting from the free-standing microfiber sensor, using a 5 mm wide copper tape (pre-cleaned with isopropanol) and silver lacquer, contact electrodes are attached at the two ends of the microfiber. The silver lacquer is left to dry at room temperature for ten minutes before mechanical and electrical characterizations of the microfibers. The mechanical and electromechanical characteristics of the microfibers are examined using a force and displacement applying aparatus, as shown in Figure 5.7. The microfiber under test is placed between the two clamps of the instrument (with the contact electrodes being isolated with a PET foil against the metal clamps).

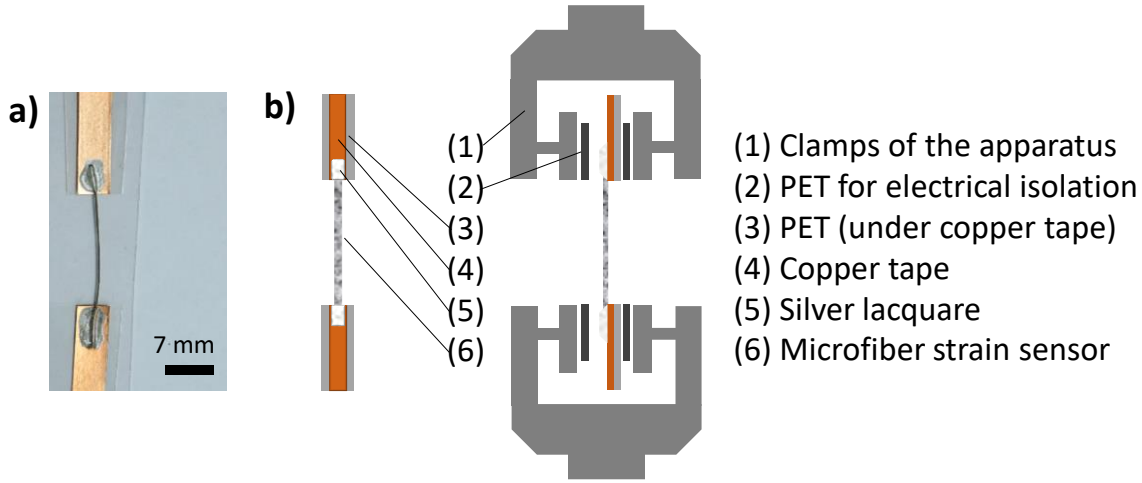

Figure 5.7. Electrode connections of the microfiber sensor for mechanical and electromechanical measurements. a) Photo of the microfiber electrode connections. A copper tape is connected to the two ends of the microfiber sensor, using a silver lacquer. b) Schematic illustration of the microfiber sensor (front and side view) for mechanical and electromechanical measurements using the tensile strain applying instrument.

5.7. Mechanical Properties of Microfibers

Under an externally applied tensile strain, as shown in Figure 5.8 (Section 3.3.4) the mechanical properties of the 4MS-EVA microfiber strain sensors are characterized.

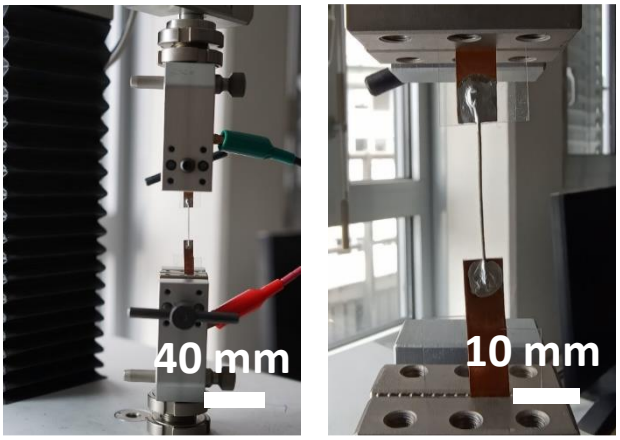

Figure 5.8. Digital photographs of the 4MS-EVA microfiber installed between the clamps of the strain-applying instrument for mechanical and electromechanical tests.

Figure 5.9a shows the engineering stress vs applied strain to eight identical pure EVA microfibers without microspheres, denoted as P-EVA. Figure 5.9b the same data (similar to P-EVA microfibers) measured for eight identical 4MS-EVA microfibers, denoted as 4MS-EVA.

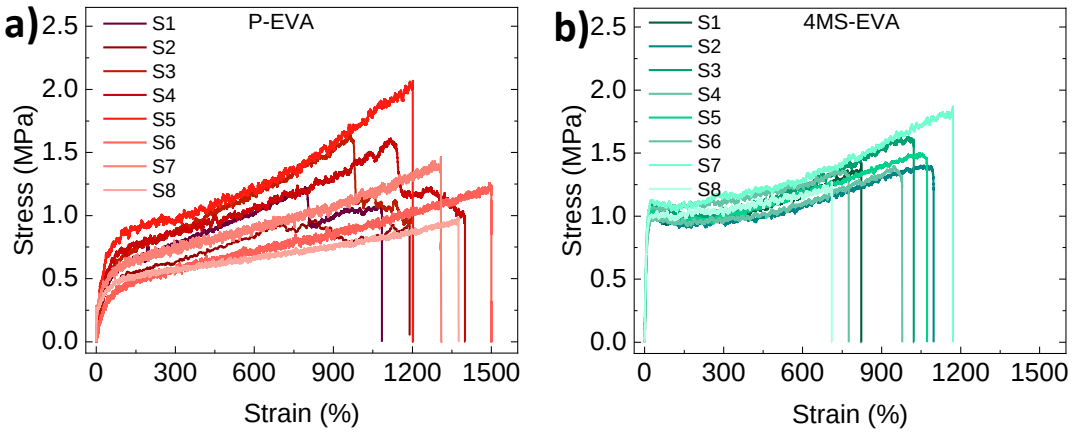

Figure 5.9. Engineering stress vs applied strain of a) pure EVA microfibers (P-EVA) and the same parameters measured for b) 4 µm microsphere containing microfibers (4MS-EVA).

Based on Figure 5.9 (and Section 2.6.1), the relevant mechanical properties of the P-EVA and 4MS-EVA microfibers are extracted and presented in bar plots in Figure 5.10. Based on Figure 5.10a the elastic modulus of P-EVA, estimated as 1.4 MPa ± 0.4 MPa, is lower compared to the estimated 9.5 MPa ± 0.8 MPa elastic modulus of 4MS-EVA. The main contributing factor to the low elastic modulus of P-EVA is the high weight ratio of the acetoxy group in EVA copolymer (compared to pure polyethylene) which hinders the neighboring ethylene chains from crystallizing. Thus, EVA with 40 wt.% has a rubbery and amorphous nature,[159,160] as opposed to PDMS which is considered a crystalline elastomer. Having 4 µm microspheres in EVA, as a natural result, apart from the elastic modulus of the microfiber, as shown in Figure 5.10b and Figure 5.10b its toughness and yield strength are also increased, respectively.

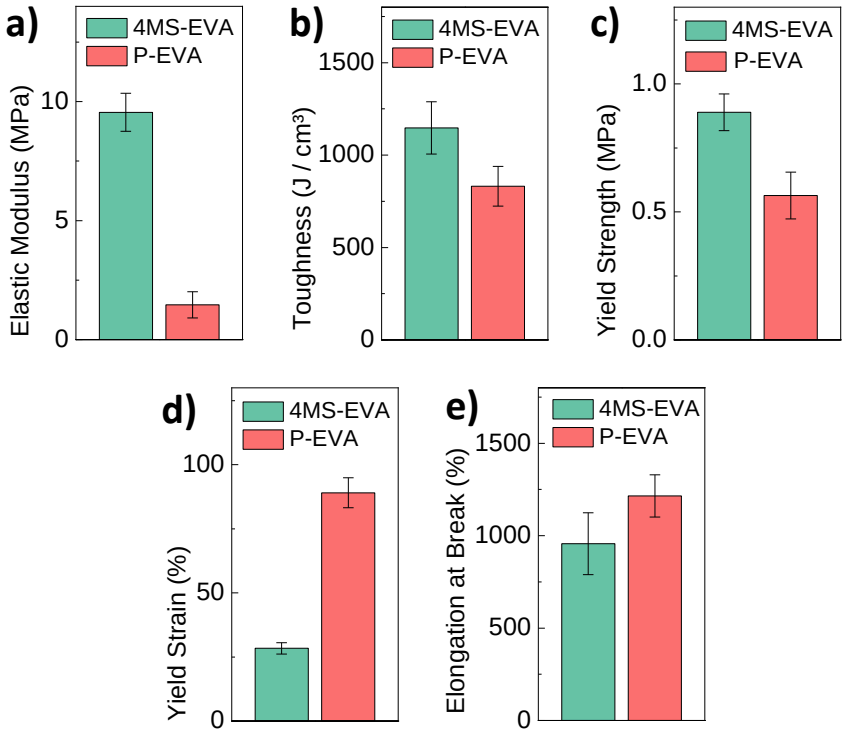

Figure 5.10. Bar plots of the mechanical properties extracted from Figure 5.9 for the eight pure microfibers (P-EVA) and eight 4MS-EVA microfibers. For a detailed description of the mechanical properties see Section 2.6.1. a) Elastic modulus. b) Toughness. c) Yield strength. d) Yield strain. e) Elongation at break.

The underlying reason behind the increase in elastic modulus, toughness, and yield strength is attributed to the well-known[161] toughening of an elastomer due to the presence of solid spherical fillers in it. This effect, in our work, stems from the decrease of vinyl acetate chain mobility as a result of microsphere inclusion in its matrix. However, for small strain sensing applications, the elastic modulus of the developed 4MS-EVA microfiber is low-enough, meaning it is considered highly conformable.[140] Compared to other filler shapes (e.g. micro flakes), the incorporation of spherical particles is proven to decrease the internal friction in the matrix due to the lower contact points between conductive fillers.[131] Another mechanical parameter determined by the stress-vs-strain plot is the mechanical yield strain, which is the strain at the onset of the plastic deformation. As shown in Figure 5.10d, from 89% for P-EVA it is decreased to 28% in 4MS-EVA. The elongation-at-break of 1282% for P-EVA, as plotted in Figure 5.10e indicates the high stretchability of the EVA, which is decreased to 956% for 4MS-EVA. The lower elongation at the break of 4MS-EVA is ascribed to the microstructure disruptions caused by the presence of solid microspheres causing polymer-particle chain ruptures at the interface. In the presence of microspheres in

4MS-EVA microfiber, as strain increases to high values the long polymer chains connecting the adjacent microspheres and the chains physically bonded to the surface of microspheres break. In the absense of the microspheres, in P-EVA under high strain, the long polymer chains having less constraints are assumed to rearange and untangle easier allowing for higher stretchability before complete microfiber rupture.[113] The summary of Figure 5.10 the relevant mechanical properties determined is presented in Table 5.2.

Table 5.2. The mean and error bars are extracted from Figure 5.9 and plotted in Figure 5.10 for eight 4MS-EVA and eight P-EVA microfibers.

	MS-EVA		*P-EVA*	
Statistical parameters	Mean	StdDev.	Mean	StdDev.
Elastic Modulus (MPa)	9.5	0.8	1.4	0.4
Toughness (J/cm³)	1140.9	141.9	846.9	125.4
Yield Strength (MPa)	0.9	0.1	0.5	0.1
Mechanical Yield Strain (%)	28.3	2.2	89.1	5.9
Elongation at Break (%)	956.2	166.9	1282.2	136.8

5.8. Electromechanical Characteristics of 4MS-EVA Microfiber Sensors

Applying strain to the conductive microfiber stretches the EVA matrix and decreases the microsphere network interconnections. The applied strain reduces the number of conductive paths consequently increasing the resistance, which is called the piezoresistive effect in an elastomer-filler composite (Section 2.2). The strain is applied using an instrument, (Section 3.3.4) and the resistance of the microfiber is measured via a SMU unit. In the following sections, the electromechanical behavior of the 4MS-EVA microfiber sensor under various tensile strain tests is examined.

5.8.1. Sensing Mechanism Based on Tunneling Theory

To investigate the sensing mechanism of the 4MS-EVA microfiber, its resistance is measured while it is subjected to a tensile strain (ε) from 0 up to the point of electrical disconnection. As shown in Figure 5.11 (violet color data), the relative change of resistance of the microfiber defined as $\Delta R/R_0$ (where $\Delta R=R-R_0$ and R is the resistance at the applied strain, and R_0 the initial resistance) is plotted against the applied strain. The experimentally measured data is examined against the tunneling theory model (cyan color line), which describes the piezoresistive response of an elastomer-filler composite (Section 2.4).[12,85] Accordingly, the sensor response (experimental $\Delta R/R_0$) is fit to the $\Delta R/R_0$ defined based on the tunneling theory model presented in Equation 5.2. As shown in Figure 5.11, the experimentally measured data is in good agreement with Equation 5.2. The fitting parameters are listed in Appendix A5.1, Table A5.1.

$$\frac{\Delta R}{R_0} = (1 + E\varepsilon)\exp[(A + FE)\varepsilon + B\varepsilon^2 + C\varepsilon^3 + D\varepsilon^4] - 1 \quad (5.2)$$

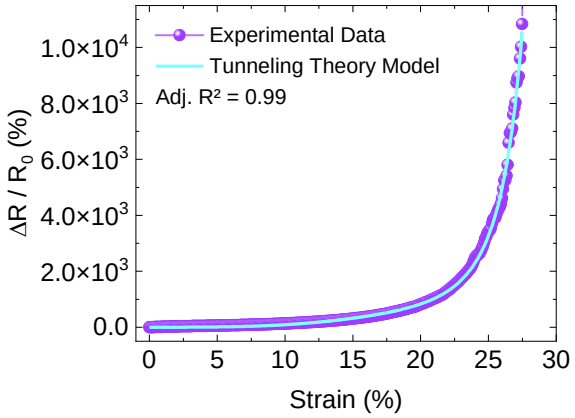

Figure 5.11. Response of the 4MS-EVA microfiber sensor subjected to an increasing strain denoted as violet color data points and the fit to it based on the tunneling theory model (cyan color line) (Section 2.4, and Appendix A5.1).

5.8.2. Strain Sensitivity

The gauge factor, defined as GF = $\Delta R/R_0 \cdot 1/\Delta\varepsilon$ is a key electromechanical property of a strain sensor. However, as discussed in Section 2.7.1, this formula is only relevant in small strain ranges where the cross-section and length of the sensing material have approximately the same value as in the relaxed state, i.e. under very small strain.[140,142] Considering Equation

5.2, meaning the response of a piezoresistive composite is exponential, a more inclusive definition to estimate the strain sensitivity is Equation 5.3.[142]

$$\frac{R}{R_0} = \exp(G\varepsilon) \tag{5.3}$$

Where G is the strain sensitivity. As discussed in the literature,[140,162,163] the resistance change of a composite of conductive filler in an insulating elastomer matrix is comprised of two different behaviors. First, in the small strain values, the first-order exponential dependence of resistance to strain appears as a linear response curve (in a semilog plot). After reaching a strain limit, which is called the working factor point, the higher orders of strain dependency come into play which is reflected in Figure 5.12 as the non-linear R/R_0 part of the plot. This is attributed to the change in the tunneling or interparticle distances in the matrix, which contributes to the surge in the rate of resistance change.

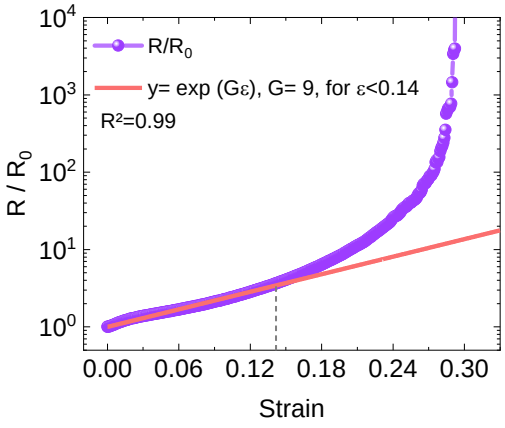

Figure 5.12. The strain sensitivity of the 4MS-EVA microfiber. A strain sensitivity (G) of 9 is estimated based on Equation 5.3 and in the linear range of R/R_0 (in the semi-log plot), which is the strain range smaller than 14%. The working factor of the microfiber sensor is estimated to be 0.14.

The key criteria for practical applications are that the sensor response should be calibratable, i.e. a measured resistance should be reliably assignable to a strain value and vice-versa. In this regard, the non-linear resistance-strain dependency is not reliable, mainly due to the onset of the electromechanical hysteresis at strain values larger than the working factor. The main origin of the hysteresis in an SPC consisting of solid particles and an elastomer is the inherent viscoelastic properties of the elastomer as well as the microstructure breakdown and failure of elastomer chain reorganization as strain grows.[140] It is important to note that the

working factor, in addition to the strain sensitivity, can be considered as a key property of the respective sensor for classifying its reliable response range.

For the 4MS-EVA microfiber, the strain sensitivity (G) of 9 ($R^2 = 0.99$) and working factor of 0.14 are obtained by fitting Equation 5.3, to the response of the sensor as R/R_0 vs applied strain, plotted in Figure 5.13. It means the response of our developed microfiber, in the linear range ($\varepsilon < 14\%$) is calibratable for a target application. The mean strain sensitivity and working factor of 10 identical microfibers plotted in Figure 5.13 is 9.1 ± 1.7 and 0.139 ± 0.029, respectively (Appendix A5.2, Table A5.2).

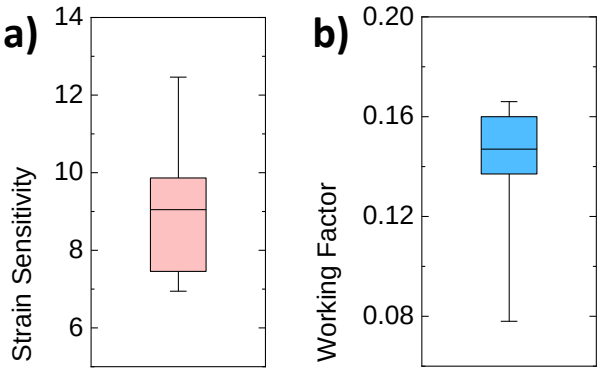

Figure 5.13. Statistical analysis of strain sensitivity and working factor of 10 identical 4MS-EVA microfibers at the respective linear response range. a) A mean strain sensitivity (G) of 9.1 ± 1.7 is estimated based on fitting Equation 5.3 to the R/R_0 vs strain data and b) the corresponding working factor is estimated to be 0.139 ± 0.029.

The commercially available metallic thin film strain gauges have a limited deformation range of less than 5% and a low gauge factor of up to 2.[164,165] Furthermore, the microfiber-based piezoresistive sensors which can detect a small strain ($\varepsilon_{min} < 1\%$), are based on more than one type of conductive and elastomer material, [34,62,77] or commonly their fabrication procedure involves expensive and arduous steps, such as high temperature, hazardous material, or high vacuum.[12,77,166] However, in this work the high strain sensitivity is realized using only one type of filler and one type of elastomer prepared in a scalable method.

5.8.3. Minimum Strain Detection Limit

The minimum strain detection limit of the 4MS-EVA microfiber under 10 repetitive strain-release cycles of 0.005% is investigated in Figure 5.14. The dynamic response of the sensor to the very small strain of 0.005% is shown as $\Delta R/R_0$ vs time. It demonstrates a consistently reproducible and easily detectable signal reaching 0.05% at the maxima. The high signal-to-noise ratio of five, under such a small strain magnitude enables facile detection of subtle deformations in the target application. It is important to note that the 0.005% strain is equivalent to detecting a 1 µm elongation over a 20 mm active sensing length, indicating the outstanding sensitivity of the developed microfiber sensor.

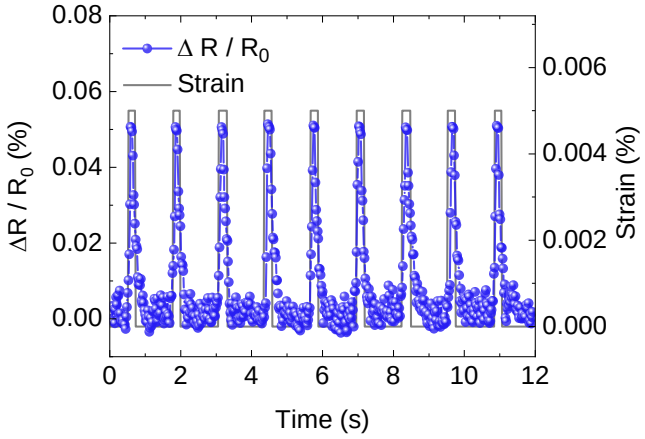

Figure 5.14. Minimum strain detection limit of the 4MS-EVA microfiber sensor. The highly reproducible dynamic response of the sensor under a cyclic strain of 0.005% indicates its reliability in detecting an elongation of 1 µm over the active sensing length of 20 mm.

5.8.4. Minimum Strain Detection Resolution

As the applied strain is changed, the smallest resolution limit, i.e. minimum strain detection resolution, is an important property that can be used to classify the performance of the strain sensor. Correspondingly, the response of the sensor as $\Delta R/R_0$ under different sequentially applied strain values from 0.005% to 0.025% in 0.005% step increase is examined. As shown in Figure 5.15, the response of the sensor to the small changes in strain is easily detectable. This high resolution in strain difference (0.005%) provides a reliable application of the developed microfiber for small strain sensing applications. Against intuition, large

conductive microspheres, with the least interparticle contact points (compared to other shapes), enable the reported detection limit and resolution in very small strain values.[131]

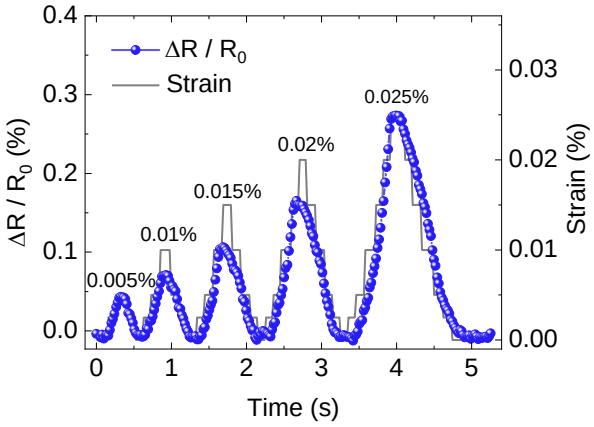

Figure 5.15. Minimum resolution of 4MS-EVA microfiber sensor in strain-change detection under 0.005% strain step increasing.

Sensing Limits Comparison to Literature

Figure 5.16 demonstrates the minimum strain detection limit and minimum resolution in strain-change detection of the developed 4MS-EVA microfiber are the lowest among the recently reported piezoresistive-based sensors (Appendix A5.3, Table A5.3).

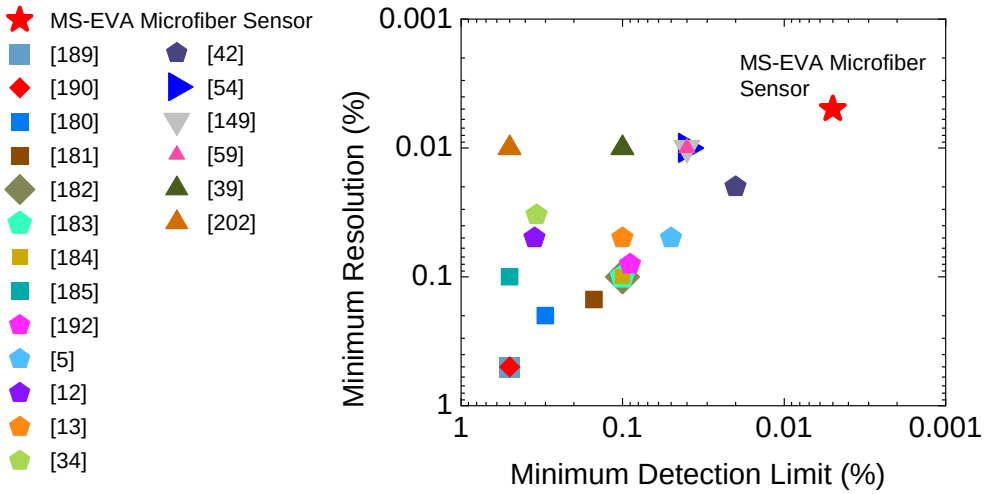

Figure 5.16. Comparison of the smallest resolution in strain-change detection and smallest detection limit of the 4MS-EVA microfiber sensor with the reported piezoresistive strain sensors.

5.9. Reproducibility of Microfiber Response

The reproducibility of the response of the 4MS-EVA microfiber to 10 repetitive cycles of 1% strain under a high rate of 900 mm min^{-1} is examined. As demonstrated in Figure 5.17, the $\Delta R/R_0$ of the sensor closely follows the strain data with slight hysteresis in resistance values. The capability to react quickly, with the least delay, to a very fast stimulus is crucial for all dynamic sensing applications. Therefore, in the following section, we examine the delay in response of the microfiber to one of the cycles (presented in Figure 5.17) more closely.

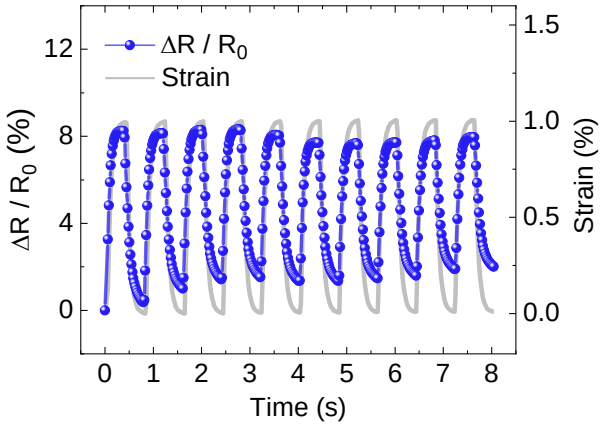

Figure 5.17. Repetitive cycles of 1% strain with a high rate of 900 mm min^{-1} are applied to the 4MS-EVA microfiber to test the reproducibility of its response.

5.10. Response Time Evaluation

The strain-applying instrument is not infinitely fast. It requires some time to take the sensor to the set elongation. Therefore, the response time of the sensor is estimated based on the delay between the time it takes for the instrument to apply or release the strain and the time it takes for the sensor to react to the instrument. The delay time in responding to a 1% strain, as shown in Figure 5.18 is estimated to be 11 ms, and it takes 34 ms to react to releasing from the strain. These time constants are calculated based on fitting both the stimulus and the sensor response to $y_i = y_{0i} + A_i * exp^{-x/\tau_i}$.

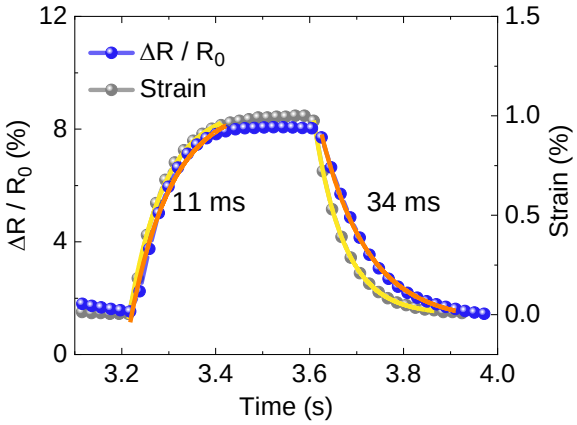

Figure 5.18. Estimating the response time of the 4MS-EVA microfiber sensor when subjected to a strain of 1% with a rate of 900 mm min^{-1} and released back to a relaxed state (Figure 5.17). It takes 11 ms for the microfiber to respond to the strain applied by the instrument, and 34 ms to react to the relaxing phase of the test.

In Figure 5.19 and Appendix A5.4, Table A5.4, the statistical delay in response time evaluation of 10 identical microfibers under applying and releasing a 1% strain are summarized. Overall the mean value for straining time constant is estimated to be 15.3 ms ± 6.7 ms and the mean response time to relaxing is estimated to be 40.6 ms ± 8.6 ms. There is generally a higher response time measured for the relaxing from the applied strain. This can be attributed to the typical mechanical hysteresis in response of a rubbery elastomer to a deformation (Section 2.7.3).[167] It is important to note that the overall very short response time of the developed microfiber sensor provides the possibility of dynamic strain sensing applications in real-time.

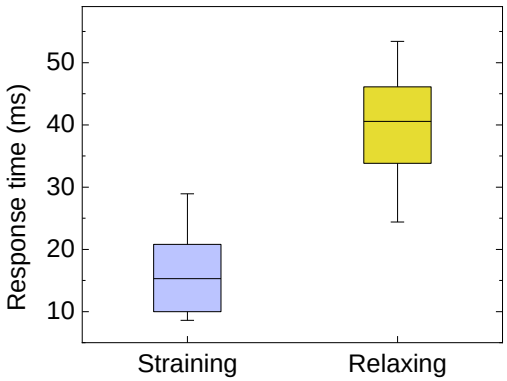

Figure 5.19. Statistical analysis of the response time estimation for 10 identical 4MS-EVA microfibers subjected to a 1% strain with a rate of 900 mm min^{-1}. The mean response time for straining is estimated to be 15.3 ± 6.7 ms, and for relaxing 40.6 ± 8.6 ms.

5.11. Durability to Overload Strain Cycles

One key requirement of an SPC sensor is its durability to strain values higher than its working factor, meaning the sensor should remain conductive and provide a reliable response even after being over-stretched. In this regard, the performance of the 4MS-EVA microfiber is tested against 5 consecutive cycles of 12% strain with a high strain rate of 900 mm min^{-1}. Figure 5.20a shows the dynamic response of the microfiber as $\Delta R/R_0$ under the strain-release cycles. As strain peaks, the sensor is electrically disconnected reaching resistances higher than 10^9 Ohms, and noticeably when relaxed, it becomes conductive again. The restored conductivity when the sensor is relaxed means the disconnected paths become mostly reconnected. This beneficial behavior is assumed to stem from using spherical-shaped conductive particles and EVA as a favorable elastomer, indicating the effective material engineering in this work. EVA is highly stretchable (elastic modulus of P-EVA is 1.4 MPa), and creates a beneficial interface with microspheres allowing for the efficient contraction of the matrix (Figure 4.3 and Figure 5.6). Additionally, due to the low internal friction of spherical fillers in the elastomer matrix, the reconstruction of conductive paths is done with the least hurdle. There is a growing hysteresis in resistances measured at the relaxed state, as plotted in Figure 5.20a which is ascribed to the inherent viscoelastic behavior of the EVA, surged microstructure breakage, and formation of voids especially at the interface with microspheres (Figure 5.6b-d).[161]

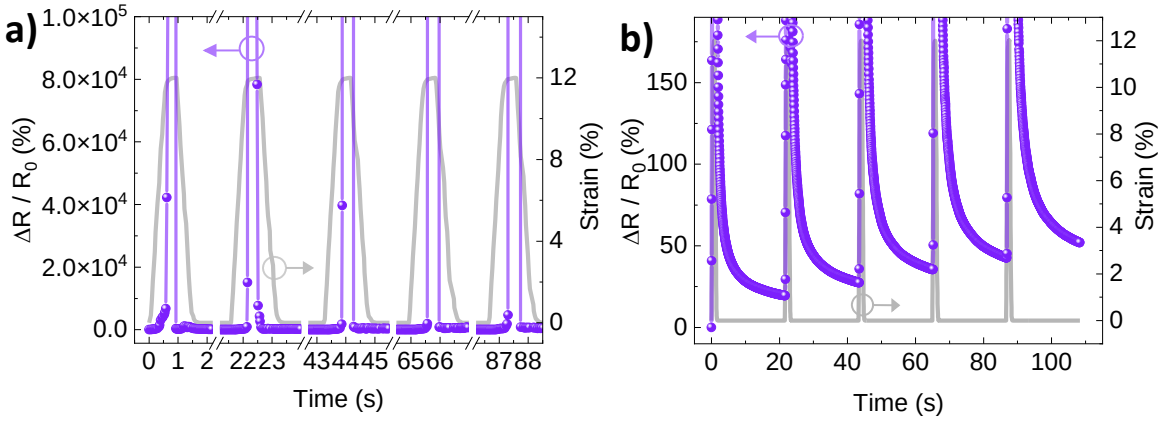

Figure 5.20. Electromechanical durability of the 4MS-EVA microfiber to cycles of 12% strain (overloading it) with a high strain rate of 900 mm min^{-1}. a) Notably, the electrical conductivity of the microfiber is retrieved after complete disconnection. b) There is a hysteresis in the reconnection of disrupted paths which is reflected in resistances at $\varepsilon = 0$.

Moreover, as shown in Figure 5.21, the microfiber is subjected to five cycles of 25% strain-release under a lower strain rate of 100 mm min^{-1} compared to Figure 5.20 (where a strain rate of 900 mm min^{-1} was applied). Here the microfiber demonstrates a repeatable response and reversible disconnection-connection transition to, overload strain, with strain values higher than its working factor. The Payne effect (Section 2.7.3) is assumed to cause strain-hysteresis behavior in recreation of conductive paths.[162] It is noteworthy that in the literature, apart from the main sensing constituents, another solid particle or encapsulating elastomer is incorporated to preserve the conductivity after complete disconnection.[77,80] Our minimalistic approach uses only one type of filler and elastomer to provide electromechanical durability to overload strain, without the aid of any secondary coating elastomer or 1D particles for reinforcements. Nevertheless, when subjected to strain values higher than the mechanical yield strain of the 4MS-EVA, at 28% strain, the microfiber becomes irreversibly disconnected. This is assumed to stem from the increased network microstructure breakdown of filler-elastomer, leading to an unbalance in the number of disconnected and restored conductive paths, finally causing conductive network failure.

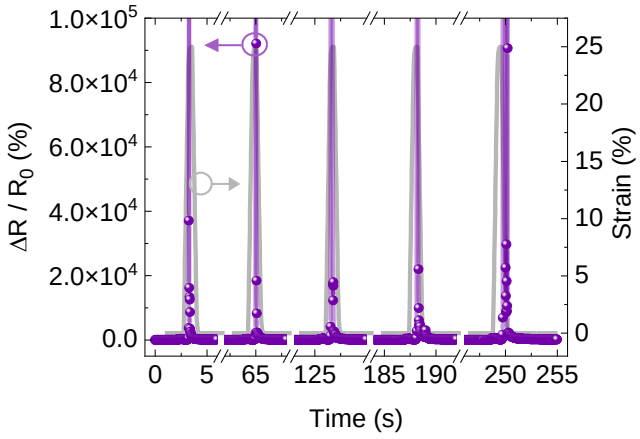

Figure 5.21. Increased electromechanical durability of the 4MS-EVA microfiber up to 25% strain under decreased strain rate from 900 mm min^{-1} in Figure 5.20 to 100 mm min^{-1}.

5.12. Durability to a Large Number of Cycles

Apart from durability to overload strain, electromechanical robustness to a large number of stretch-release cycles is a key aspect of an SPC sensor for the target applications. The 4MS-EVA is subjected to 10,000 cycles of 1% strain, as shown in Figure 5.22.

Over the entire test a higly reproducible strain detection is observed. The repeatability of the microfiber response (plotted as $\Delta R/R_0$), shown in the insets in Figure 5.22, throughout the cycles indicates the microfiber robustness for such a high load of strain-release. During the first 900 cycles, overall there is a slight reduction in the magnitude of $\Delta R/R_0$ which is ascribed to the stress-softening effect in a composite of solid filler and elastomer subjected to repetitive stress cycles, which is the Mullins effect (Section 2.7.3).[106,113,162] Additionally, in Appendix A5.5 the result of the static resistance measurement of 4MS-EVA microfiber sensors with one-month intervals within a year is demonstrated.

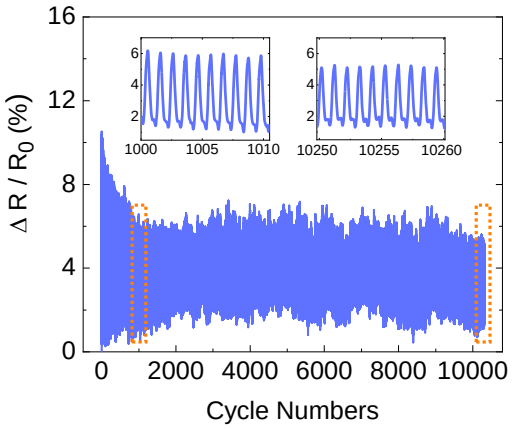

Figure 5.22. Electromechanical durability of the 4MS-EVA microfiber against more than 10,000 cycles of 1% strain. The two snapshots shown as insets demonstrate the responses during two time windows on the left from the 1000th to the 1010th cycle, and from the 10250th to the 10260th cycle.

5.13. Summary

The development of a free-standing piezoresistive microfiber strain sensor using the straightforward and industrially favorable wet-spinning fabrication method is described in this chapter. A viscous solution mixture of conductive microsphere and EVA-anisole is prepared and dispensed in the acetone as the non-solvent bath. During the wet-spinning, due to the solvent exchange between the anisole and acetone coagulation happens. Subsequently, EVA becomes densified and the EVA-microsphere microfiber is formed in the bath. The microfiber microstructure reveals a compact and uniform structure in which clusters of agglomerated microspheres are embedded in the matrix of EVA. The morphology of the interface EVA makes with microspheres is studied under tensile strain and using SEM

images, confirming the same type of loosely formed coverage around microspheres, as discussed in Section 4.4. The mechanical properties of the EVA microfiber are compared with 4MS-EVA microfiber under tensile strain. Overall when microspheres are included in the EVA matrix, although there is an increase in elastic modulus, toughness, and yield strength, the 4MS-EVA remains soft enough and in the highly conformable range for subtle strain sensing applications. There is a decrease in yield strain and elongation at the break of the microfiber. The underlying reasons behind the observed changes in the mechanical properties are the typical toughening effect due to the presence of solid particles in the elastomer as well as the earlier microstructure and filler-elastomer breakage. Electromechanical properties of the microfiber are studied under various tests including increasing strain, repetitive and very small strain cycles, sequentially increasing very small strain cycles, very fast rate strain cycles, repetitive overload strain, and a large number of strain cycles. The strain sensitivity of the microfiber is estimated to be 9 in the linear range, and the corresponding working range is estimated to be below 14%. The minimum detection limit of the microfiber is estimated to be bellow 0.005%, and its minimum resolution limit is also estimated to be less than 0.005%. These two properties are the lowest, to the best of our knowledge, in the reported piezoresistive sensors. Under a fast strain rate, the microfiber demonstrates a highly reproducible response, with a very small delay of 11 ms in responding to straining and a 34 ms delay in reacting to releasing the strain. The electromechanical durability of the microfiber strain sensor is examined under overload strain cycles. Under repetitive cycles of 12% strain with a very fast rate of 900 mm min^{-1} retrieved electrical conductivity (after complete disconnection) is exhibited. Furthermore, the threshold of reversible conductivity is increased to 25% strain when the rate is reduced to 100 mm min^{-1}. Lastly, the electromechanical durability of the microfiber sensors is examined under 10,000 cycles of 1% strain where reliable and reproducible responses over the whole cycle are demonstrated. All in all, the highly sensitive microfiber developed in this work demonstrates promising electromechanical properties for real-time small strain sensing applications providing high resolution and easily detectable signals even under very small elongations.

6. Microsphere-based Strain Sensor Applications

In this chapter, three different applications for stretchable strain sensors based on a composite of 4 µm conductive microspheres and EVA, are demonstrated. The first application introduced here is impact sensing via the printed composite on the stretchable PU substrate. Based on the promising electromechanical properties discussed in Chapter 4, real-time small impact detection is demonstrated where high sensitivity and high-resolution response are shown. The second application demonstrated here is dynamic diaphragm expansion monitoring using the printed composite. The estimated strain magnitudes applied to the sensor during diaphragm expansion tests are estimated to be above the working factor of the sensor, exhibiting outstanding electromechanical durability to overload strain. In the last part of this chapter, the free-standing microfiber introduced in Chapter 5 is employed for dynamic lithium-ion battery expansion monitoring, for the first time, using a stretchable composite. During consecutive lithium-ion battery charge and discharge cycles, seven microfibers attached to the sides of the battery provide an easily detectable signal with high resolution for the different states of expansion and contraction. The microfibers provide reproducible responses closely mirroring a costly commercially available displacement sensor. The results presented in this chapter in Sections 6 and 0 have been previously published in the journal of Advanced Sensor Research.[126] *The results presented in Section 6.1 have been previously published as a journal article in Advanced Materials.*[148]

6.1. Impact Monitoring with Printed 4MS-EVA Sensors

Monitoring the impacts on a surface has a wide range of applications across industries such as sports performance and healthcare monitoring, automotive safety, and structural health monitoring in civil engineering and infrastructure.[168,169] Impact and collision monitoring play a crucial role in improving safety, performance, and risk mitigation across various fields. Impact sensing is commonly performed in real-time by various sensor types e.g. gyroscopes, force-sensitive sensors, and strain gauges. During an impact, a strain gauge that is integrated into the target device detects the impact by outputting a sudden resistance change. Therefore, one important property of the employed sensor should be high resolution, high sensitivity, and fast response. The printed 4MS-EVA sensor introduced in this work is capable of resolving a strain as small as 0.015% with a high signal-to-noise ratio, providing fast response, and durability to 1000 cycles of 1% strain. These performance characteristics match the required criteria for high-resolution collision sensing applications. In the following, the performance of the 4MS-EVA sensor for impact sensing is examined.

6.2. Sensor Preparation for Impact Monitoring

For impact sensing, the printed sensors are used directly after being dried and reached to the room temperature. A copper tape with a length of 12 cm length and a width of 5 mm and a conductive adhesive layer is attached to the screen-printed electrodes. As shown in Figure 6.1, to facilitate the electrode connections to the sensor during the impact monitoring, a 5 mm wide copper tape having a conductive adhesive layer underneath is attached to the screen-printed electrodes.

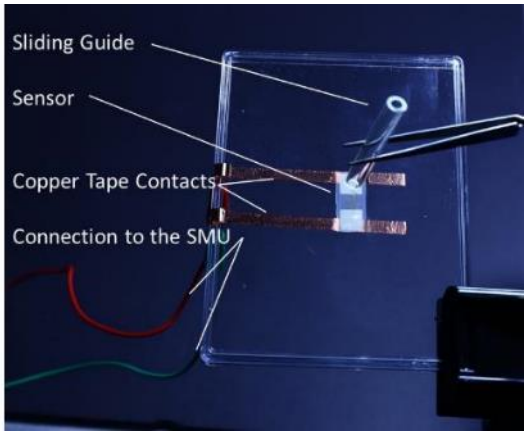

Figure 6.1. The impact sensing application setup prepared in this work

Then the sensor is adhered from the backside on top of a rigid plastic plate using a double-sided tape. The plate having the sensor attached to it is fixed on a table using a clamp. To create precise subtle impacts on the sensor, 15 small solid objects weighing 55 mg to 680 mg are dropped on the sensor from a fixed height of 60 mm. To hit the same spot at the (back) middle of the sensor, the objects are guided through a slider. The electrical response of the sensor is recorded based on a two-probe resistance measurement setting using a source-measure unit (Keithley 2612B). A DC source voltage of 50 mV is applied and the resistance readings are recorded with a 50 Hz frequency.

6.3. Impact Monitoring

As a surface is subjected to an impact shock, if it is not displaced due to the collision, the impact energy is assumed to be transformed to the surface. Impact monitoring using a piezoresistive strain sensor is commonly done by translating the detected change of the resistance of the sensor to the impact energy absorbed by the surface.[169] In this work, to apply a tunable impact on a solid surface and estimate the impact energy, in a test setup shown in Figure 6.2a various small solid objects weighing 55 mg to 680 mg are sequentially dropped from the same height on the middle of a surface at the back of which the printed 4MS-EVA sensor is attached. During the test, the 2-probe resistance of the 4MS-EVA sensor is measured using a SMU. Figure 6.2b presents the real-time data of the printed 4MS-EVA sensor as $\Delta R/R_0$. The response of the sensor is characterized by a sharp increase of resistance at the time of the impact, meaning a sudden strain is applied to the sensor, following a gradual relaxation after the collision. This is a typical resistance change behavior of a piezoresistive composite of filled elastomers subjected to an abrupt collision as the external stimulus.[168–170]

As shown in Figure 6.2c the response of the printed 4MS-EVA sensor to the impact is estimated to be 20 ms. This is a remarkably low response time and is especially beneficial for real-time impact sensing applications. Also, it is important to note that the obtained impact time is the same regardless of the mass of the dropped objects. Since all the test objects bounced back right after hitting the fixed solid surface, we assume that the collision is elastic. Therefore the kinetic energy of the impact E_i absorbed by the surface at the time

of that impact can be estimated to be equal to the potential energy of the object m_i at the height of h, that is m_igh.

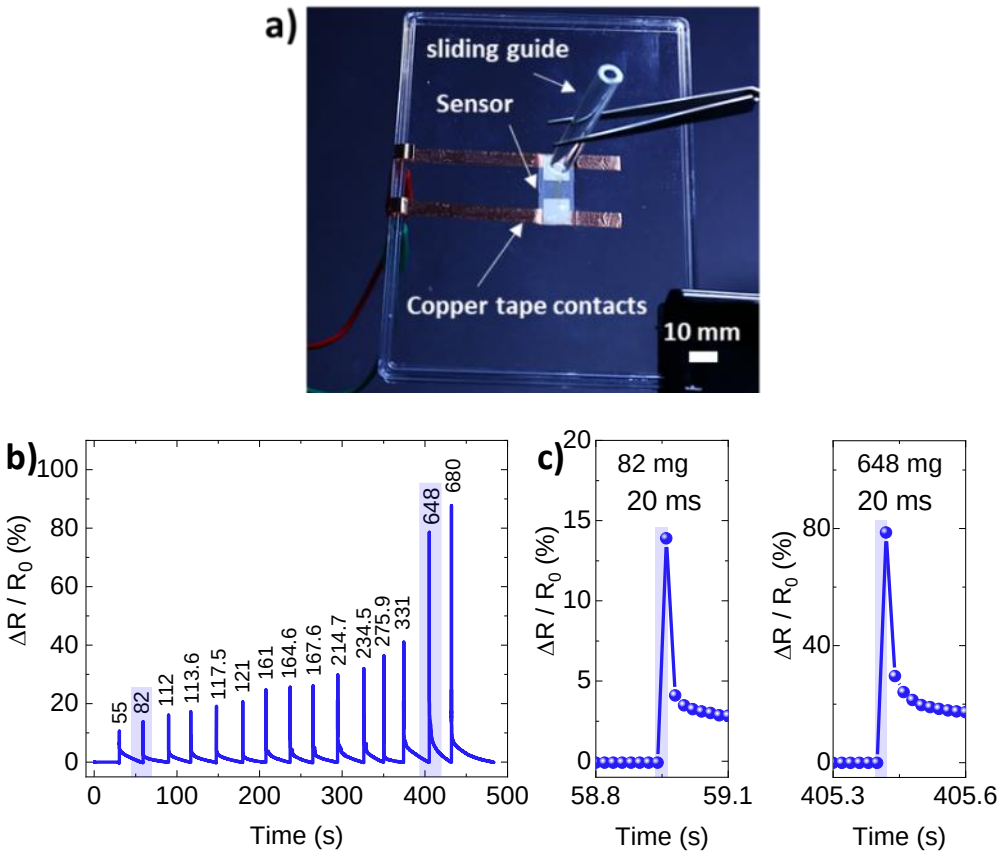

Figure 6.2. Impact sensing performed using the 4MS-EVA sensor. a) The setup for impact sensing. As small objects weighing 55 mg to 680 mg are dropped from a height of 60 mm through the sliding guide at the back (middle) of the sensor, their dynamic (2-probe) resistance is measured. b) Response of the sensor, plotted as $\Delta R/R_0$ over time during the collisions. c) Response time of the sensor to the impact created by an 82 mg object on the left and a 648 mg object on the right.

As plotted in Figure 6.3, the relationship between the $\Delta R/R_0$ at the peak of impact and the impact energy (corresponding to the mass of dropped objects) is linear. In the inset of Figure 6.3, the capability of the sensor to resolve a very small impact energy difference of 0.942 μJ is demonstrated. As plotted in Figure 6.3, the relationship between the $\Delta R/R_0$ at the peak of impact and the impact energy (corresponding to the mass of dropped objects) is linear.

In the inset of Figure 6.3, the capability of the sensor to resolve a very small impact energy difference of 0.942 µJ is demonstrated. Here the recorded difference of the output signal ($\Delta R/R_0$ max) is 1.2%, meaning an easily detectable signal for such a small change in the impact energy. This corresponds to differentiating a Δm of 1.6 mg in the masses of the two objects (113.6 mg−112 mg) dropped from a 60 mm height on the sensor, indicating the high-resolution capability of the sensor for impact sensing applications. Furthermore, the smallest object tested weighs 55 mg resulting in an $\Delta R/R_0$ of 10.66% corresponding to a E_i = 32.61 µJ at the peak of impact, showing the high sensitivity of the sensor to very low collision energies. The fast response, high sensitivity, and high resolution demonstrated in this proof-of-concept application are made available through the minimal contact point between microspherical conductive particles. These findings point toward the promising path of using conductive microspheres for the development of tactile sensors for IoT and consumer electronics applications.

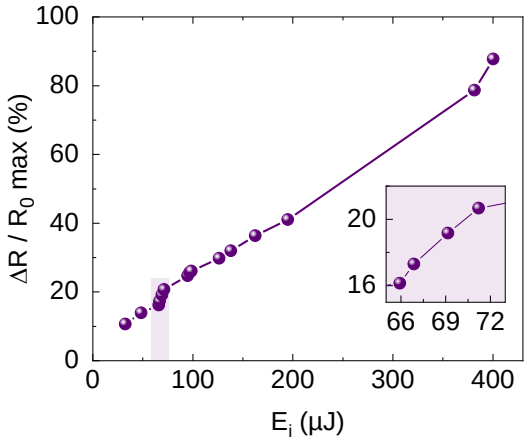

Figure 6.3. Response of the printed 4MS-EVA sensor (plotted as $\Delta R/R_0$) at the peak of impact vs the kinetic energy of the impact absorbed by the surface. Inset: a closer look at the impact energy resolution. Between the first two points, the energy difference is < 1µJ which is detected by a signal difference of 1.2%.

6.4. Diaphragm Expansion Monitoring with 4MS-EVA Sensors

In addition to the impact sensing discussed in the previous section, since the printed 4MS-EVA sensor shows beneficial sensing properties, in this section we show case its use for soft membrane expansion monitoring.

6.4.1. Sensor Preparation for Diaphragm Expansion Monitoring

As the diaphragm, a circular sheet with a 25 mm diameter is cut from the PU substrate that is the same substrate sheet on which the active sensing material is printed (Section 3.2.3). The sensor is used after being dried. As shown in Figure 6.4, two copper tapes (5 mm width) with a conductive adhesive layer are attached on the sensor electrodes (screen-printed silver). After the sensor electrode connection for the diaphragm expansion monitoring, the sensor is adhered to the expandable diaphragm using a double-sided tape. Then the diaphragm is fixed around a cylindrical container using an O-ring. To inflate the diaphragm at fixed intervals, pressurized air is pumped into and released immediately. The electrical response of the sensor is recorded in the two-probe setting using a source-measure unit (Keithley 2612B) applying a 50 mV DC voltage and the connected crocodile clamps simultaneously record the resistance readings with a 50 Hz frequency.

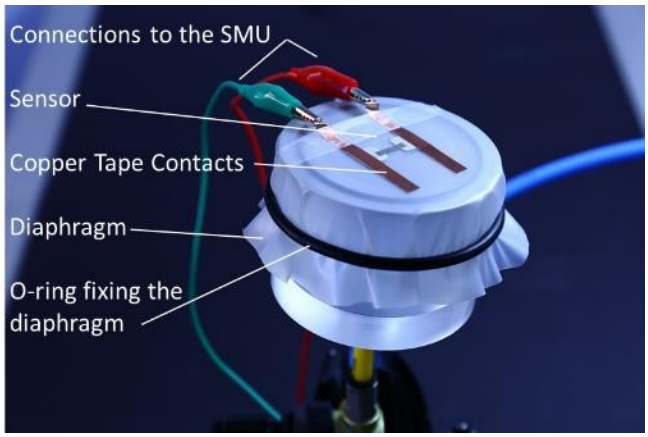

Figure 6.4. Diaphragm expansion monitoring application setup prepared in this work.

6.4.2. Diaphragm Expansion Monitoring

Figure 6.5d demonstrates the real-time response of the sensor as $\Delta R/R_0$ during the expansion and relaxation of the membrane. According to the movement of the diaphragm, the response of the sensor shows first a sharp increase and then a gradual decrease. Swallowing of the membrane results in a sudden rise of the $\Delta R/R_0$ following a slow decrease of it as the air is released.

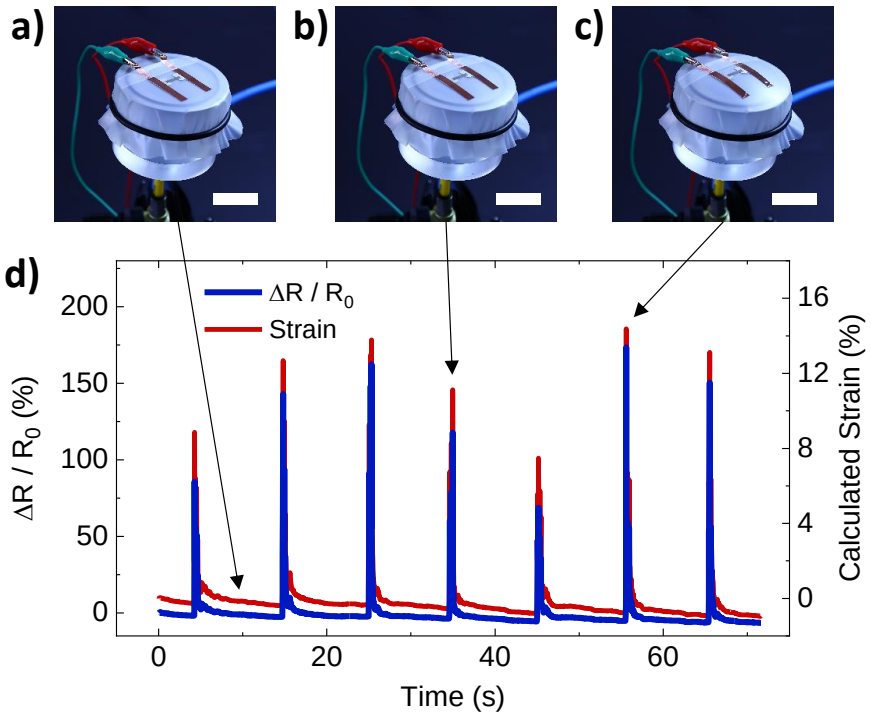

Figure 6.5. Diaphragm expansion monitoring using the 4MS-EVA sensor. a) Relaxed state (scale bars 40 mm). b) Expanded diaphragm. c) A larger expansion compared to b. d) Real-time response of the sensor as $\Delta R/R_0$ during the diaphragm expansion monitoring.

By plugging the response of the sensor as R/R_0 and the strain sensitivity (G) of 7 into the $R/R_0 = \exp(G\varepsilon)$ equation (Section 4.5) the corresponding strain applied to the sensor can be calculated. The strain experienced by the sensor in the diaphragm expansion shown in Figure 6.5c is estimated to be 14% which is reflected as 173% in $\Delta R/R_0$ at the peak. The inflation shown in Figure 6.5b applies an estimated strain of 11% causing a $\Delta R/R_0$ of 118% at the peak of the sensor response. The data presented here confirms the electromechanical durability of the printed 4MS-EVA sensor to strain values higher than its working factor as well as the reproducibility of its response to over-load strain measurements in real-life applications. These results emphasize the suitability of the developed sensor for soft membrane deformation monitoring applications such as healthcare, rehabilitation, E-skins, and robotics.

6.1. Lithium-ion Battery Expansion Monitoring

The lithium-ion (Li-ion) battery is the most popular energy storage battery in a wide range of applications such as consumer electronics or electric vehicles. Monitoring the health of a Li-ion battery during its lifetime is crucial for example to prevent early capacity reduction and decrease hazardous waste, as well as prohibiting the dangerous material leakage and explosion as a result of battery failures. During charging and discharging of the battery, because the lithium travels from cathode to anode and vice versa (that is called Li-ion de/intercalation), there are various reactions between the liquid electrolyte and the electrodes. Correspondingly, the cathode and anode lattices undergo inevitable expansions and contractions during charge and discharge cycles, giving rise to reversible battery volume expansions and contractions. This inevitable volume change is known as the breathing which _in the long run_ causes gradual structural degradation of a Li-ion battery.[164] Additionally, irreversible volume expansions are happening during charging and discharging known as swelling. The primary origin of the swelling is found to be unwanted side reactions such as gas generation, increase of solid electrolyte interphase layer, and lithium-plating. These reactions over time lead to increased internal resistance, reduction of Li-ion inventory, capacity loss, and reduced energy efficiency.[171,172] As a result of these reactions, during cycling commonly there are volume changes ranging from 1-10%, depending on the chemical composition of the electrodes and the electrolytes.[172] Thus, to enhance the Li-ion battery lifetime and therefore prevent premature aging, monitoring the volume changes of the battery in real-time has a high importance in battery management systems.[173,174] In this regard, currently there are multiple characterization techniques engaged in battery health diagnosis through volume change measurements. Examples are X-ray diffraction,[175,176] 3D digital image correlation,[177,178] atomic force microscopy,[179] ultrasonic probing,[180,181] optical sensors,[182–185] neutron imaging,[186] mechanical measurement approaches,[164,171,187–190] and displacement gauges.[172,191] Notwithstanding their success, the above-mentioned methods, in terms of the laboratory pieces of equipment needed for a single battery measurement are quite demanding and costly, and cannot be easily integrated into a battery for in-situ volume expansion monitoring.[173,192] Hence, an all-rounder volume measurement method is required that in addition to providing high-resolution and reliable data, is low-cost and its integration with diverse battery form factors is straightforward.

6.1.1. Lithium-ion Cell Assembly and Formation

The Li-ion cell assembly[a] is performed using commercially available electrodes, containing 20 double-sided cathodes and 21 double-sided anodes. Cathodes consist of $LiNi_{1/3}Mn_{1/3}Co_{1/3}O_2$ (NMC 111) with 94 wt.% active material and are 135 mm × 208 mm in size. Anodes, consisting of graphite, are 139 mm × 212 mm in size. As separators between anodes and cathodes, 143 mm × 216 mm ceramic-coated PET separators are used. Electrodes and separators are dried under low pressure for 24 h at 130 °C and 180 °C, respectively. Then as the electrolyte, the cell is filled with 80 ml LP30 and sealed under low pressure. Afterward, it is stored at 40 °C overnight. The cell has a theoretical capacity of 20 Ah. For the Li-ion cell formation, after cell assembly is performed as described above, an initial charging is performed with a constant current (CC) mode with a C/10 rate, following a constant voltage (CV) mode charging up to 4.2V, until the current decreased to C/20. Then the cell experienced two cycles at a C/2 rate, where charging was performed using a CC-CV mode until the current dropped below C/20. All electrochemical cell-cycling tests are performed with BasyTec HPS LAB at 26°C ± 1°C.

6.1.2. Microfiber Sensor Preparation for Li-ion Cell Thickness Monitoring

After the microfibers are dried under the vacuum at room temperature they are used for the Li-ion battery expansion monitoring. As the book-format Li-ion cell used in this work has a thickness of around 7 mm (Table 6.1), the two-meter long microfiber is cut into 15 mm long pieces to allow for 7.3 mm active sensing length and the electrode connections. The microfibers are fixed vertically at the edges of the two horizontal PMMA plates (holding the Li-ion cell) to the pre-attached copper tape using a silver lacquer. Afterward, the contacts are left to dry at room temperature for ten minutes. Then to ensure minimal residual strain in the microfibers after being attached to the setup, and before Li-ion cell thickness monitoring, the setup is held as prepared overnight.

[a] The Li-ion pouch cell used in this work is prepared by Christopher Schwab under supervision of Dr. Anna Smith at the Institute for Applied Materials - Energy Storage Systems at Karlsruhe Institute of Technology.

Lithium-ion Cell Expansion Monitoring Application

For the Li-ion cell expansion monitoring, it is initially discharged under a 1C rate, followed by four cycles in the voltage window of 3-4.2V charging in a CC-CV mode until the current drops to C/10 and discharging in CC mode, both with a 1C rate. Then the cell is charged to a nominal 3.7 V. It is important to note that all the electrochemical measurements are performed at 26°C ± 1°C. As the reference sensor for the thickness measurement a displacement gauge from Keyence (GT2-H12) is used having a minimum detection limit of 2 µm and 0.5 µm resolution. As shown in Figure 6.6, the reference sensor is at the center of the middle plate. While the Li-ion cell is undergoing cycles of charge and discharge, the data of the reference sensor is obtained in real-time with 1 Hz frequency using the Keyence (GT-Monitor 2) Test version software. The electrical response of the seven microfiber sensors is simultaneously obtained in a two-probe setting (using two crocodiles for each microfiber) by a Data Acquisition/Switch Unit (34972A) from Keysight under a DC source voltage of 50 mV. The resistance of all microfibers is measured with a 1 Hz frequency. The relative resistance change of the microfiber sensors is then correlated to z-direction displacements recorded by the reference displacement sensor.

Figure 6.6. Photograph of the Li-ion battery thickness change monitoring setup. While the Li-ion cell is undergoing a charging and discharging cycle, a reference sensor, installed in the middle of the setup which is connected to a laptop (using the Keyence GT-Monitor 2 Test version software), is recording the displacement changes. Simultaneous to reference data and Li-ion battery cycling, the real-time

resistance of the microfibers installed vertically around the setup are recorded using a multi-channel Keysight (data acquisition/switch unit).

6.1.3. Monitoring Li-ion Battery Expansion with Microfiber Sensors

A crucial part of a Li-ion battery health management system is monitoring the thickness or volume changes of the battery during charge and discharge cycles. In this regard, depending on the battery requirements, e.g. the form factor of the battery under investigation and the available space for the measurement an appropriate sensor is chosen. The remarkable sensing properties and high conformability of the 4MS-EVA microfiber sensor developed in this work offer a promising solution to the current demands of dynamic Li-ion battery thickness monitoring. Figure 6.7 demonstrates the setup prepared for the Li-ion battery monitoring. Here, a book-format Li-ion pouch cell (made in the laboratory)[a] is placed in between two solid PMMA plates for thickness monitoring in the z-direction (Δz), and one plate is fixed on top. Four springs are located at the corners of the plates (around a fixed rod), to keep the two lower plates in contact with the pouch cell during the thickness changes. These springs also apply a small z-direction force to the middle plate to ensure a more balanced movement of that plate during the measurements. Seven 4MS-EVA microfibers, having an active sensing length of 7.3 mm (Figure 6.7b) are located perpendicular to the plates on three sides around the cell, leaving one side for the battery electrode connections. The two-probe resistance of the microfibers is measured in real-time using a single SMU. There is a reference sensor, a commercially available displacement sensor (RDS), located at the center of the setup with its measurement tip extruding the upper most sheet to become in direct contact with the middle plate, which is in touch with the pouch cell's upper surface (Figure 6.7a and Figure 6.7c). A schematic illustration of the Li-ion pouch cell and the structure of its stacks is shown in Figure 6.7d.

[a] The preparation, formation, and all the electrochemical measurements of the Li-ion pouch cell used in this work is performed by Christopher Schwab with supervision of Dr. Anna Smith at the Institute for Applied Materials - Energy Storage Systems at Karlsruhe Institute of Technology.

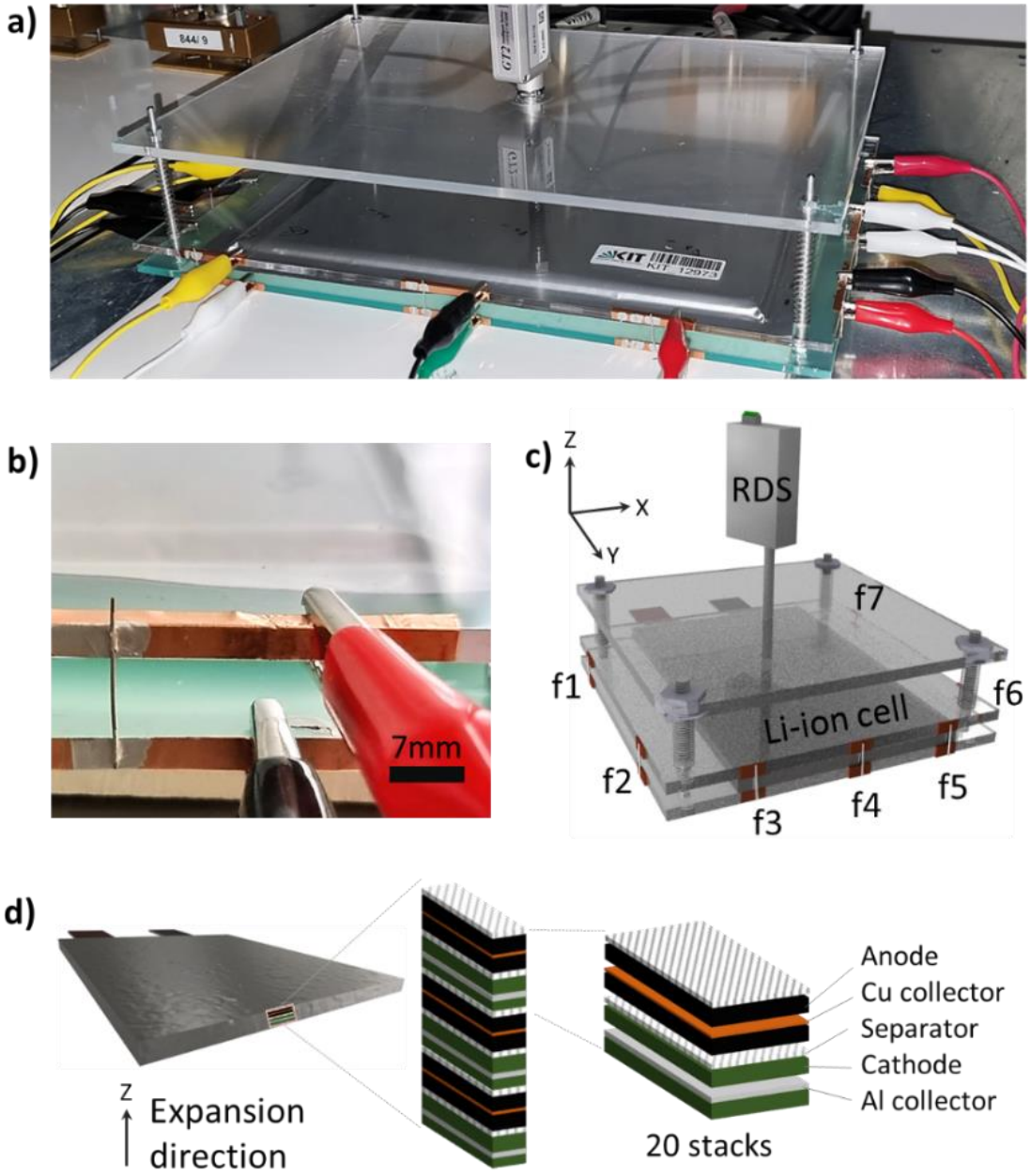

Figure 6.7. 4MS-EVA microfiber sensor employed for real-time thickness change monitoring of a Li-ion pouch cell. a) Digital photo of the prepared setup for thickness measurements. A Li-ion pouch cell is placed between two solid PMMA plates. At the four corners of the plates, springs are located to keep the two lower plates in contact with the pouch cell. A commercial displacement reference sensor (RDS) is installed in the middle of the setup. The seven MS-EVA microfibers are attached vertically at the three sides of the plates. While the pouch-cell undergoes charging and discharging, the real-time data of the RDS is collected on a laptop and the microfibers are connected to a multichannel SMU using which the two-probe resistances are recorded. b) A digital photograph of the position and electrode connections of one of the microfiber strain sensors in the setup. c) A schematic illustration of the prepared Li-ion battery thickness monitoring setup in this work. The dynamic cell thickness change is recorded in the z-direction by the RDS at the

center simultaneous to seven microfibers on the sides. d) A schematic illustration of the internal structure of the Li-ion pouch cell used in this work. It is comprised of 20 double-sided NMC cathodes and 21 double-sided graphite anodes stacked in z-direction.

One complete charging and discharging cycle of the Li-ion cell is shown in Figure 6.8. The corresponding cell voltage is plotted in black and the recorded RDS data is shown in gray. The calculated thickness changes of the cell based on the resistance changes of one of the microfibers are plotted in orange color. In our cycling routine, the cell is in constant current mode (CC) charged up to 4.2 V, and then charging is continued with a constant voltage mode (CV) under a 1C rate. Afterward, the discharging is performed up to 3 V with CC mode under a 1C rate.

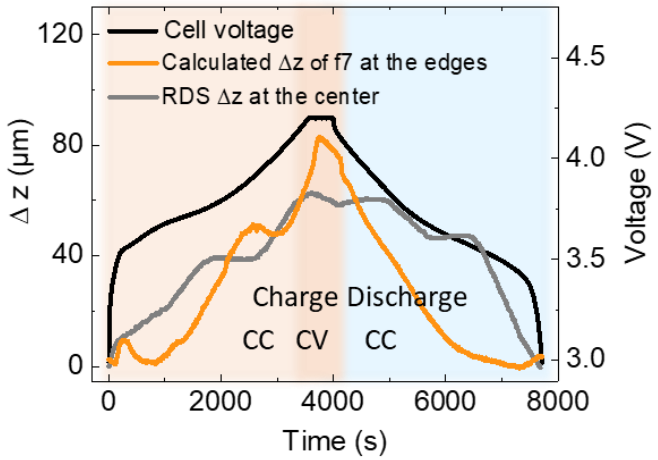

Figure 6.8. The Li-ion cell voltage during one charge and discharge cycle (plotted in black color), the calculated Li-ion cell expansion in the z-direction (Δz) during the cycle measured by one of the microfibers (f7) at the sides of the setup (plotted in orange color), and the thickness monitored using the reference sensor at the middle of the setup during the same cycle (gray color).

The cell inflates while charging under CC mode and based on the reference sensor data (measured at the center of the setup) reaches a maximum thickness change of 62 μm at the peak. The elongation experienced by the microfiber f7, is calculated based on the response of the sensor as R/R_0 (shown in the orange line in Figure 6.8), the estimated strain sensitivity (G) of 9, and $R/R_0 = \exp(G\varepsilon)$. Correspondingly, the elongation of the f7 microfiber sensor experienced at the peak of cell expansion is estimated to be 80 μm. It is important to note

that, the small difference between the measured thickness changes of the RDS and the f7 microfiber can be ascribed to the difference in their location on the setup. The RDS is located at the geometrical middle point of the setup, directly in contact with the middle plate, while all the microfibers are installed at the edges of the setup. In Figure 6.9, the real-time response ($\Delta R/R_0$ vs time) of the seven microfiber sensors denoted as f1 to f7 monitoring the expansion of the Li-ion cell at the edges of the setup is shown. All seven microfibers, similar to the response of the reference sensor, provide valuable information on the different phases of the Li-ion cell expansion.

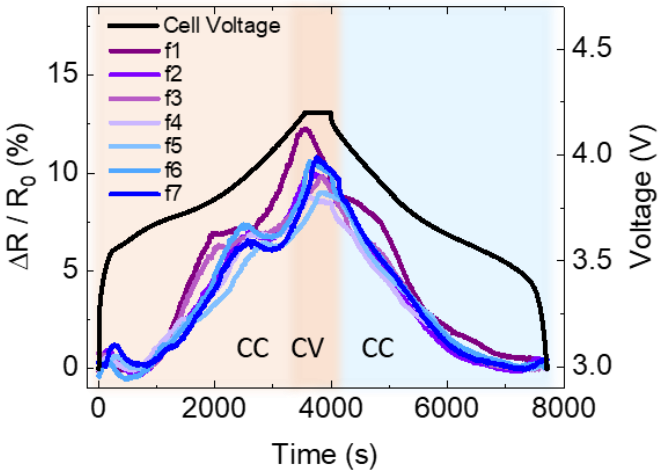

Figure 6.9. Real-time response of the seven microfibers f1-f7 to the tensile strain applied to them due to the Li-ion cell expansion during one charge and discharge cycle and the corresponding cell voltage during that cycle.

As the cell inflates, during the CC-charging phase, it applies a tensile strain of 0.085% to the microfibers at the peak of expansion which is reflected in a $\Delta R/R_0$ of 10%. It is important to note that the contraction of the cell already starts as the charging phase continues in the CV mode, instead of getting started at the discharge phase. This is notable in the shape of $\Delta R/R_0$ as the CV-mode charging begins. As an example, the f7 reaches an $\Delta R/R_0$ of 10.8% at the peak when the charging CC mode ends following a reduction in $\Delta R/R_0$ to 9.7% as reaching the end of the charging in CV mode. The cell contraction during the charging in CV mode corresponds to a -0.05% change in strain ($\Delta\varepsilon$). Based on this observation, it can be inferred that during the CV-mode charging when reducing the current, overall the volume relaxation is dominant compared to the volume expansion of the anode due to the lithiation of the anode. After the end of charging, the discharging is performed in CC mode showing contraction of the cell until reaching the initial thickness. In Figure 6.10 the calculated cell

thickness changes experienced by the microfibers are plotted for f1-f6, based on the R/R_0 of the individual sensors, the G of 9, and $R/R_0 = \exp(G\varepsilon)$. Here as well, the microfibers follow the course of the reference sensor data. Based on the calculated thickness changes recorded by the microfibers, and the RDS data, the cell thickness evolution can be studied in real-time. During charging the cell first expands applying a tensile strain to the microfibers, up to the peak of expansion at the end of CC charging mode. Then it contracts as charging continues in CV mode, which is reflected in the detected strain being released from the beginning of CV charging mode. The cell shrinkage continues further to reach the initial status by the end of the discharging in CC mode which is reflected in the response of the microfibers.

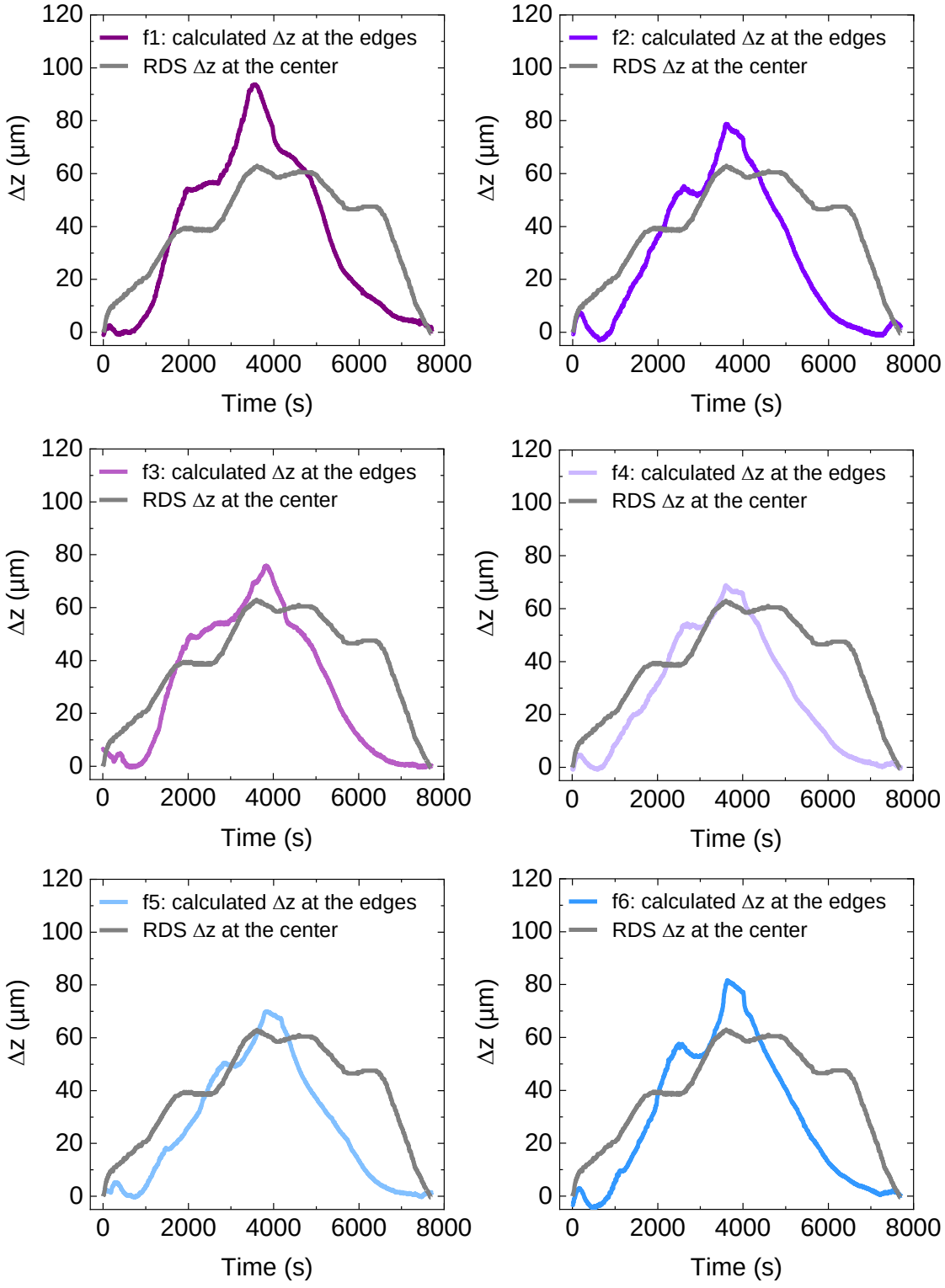

Figure 6.10. The elongation applied to the microfibers due to cell expansion and contractions (based on the response of each microfiber as R/R_0, the strain sensitivity (G) of 9, and the $R/R_0 = \exp(G\varepsilon)$, during one complete cycle. The electrical response of the microfiber to the thickness changes is converted to elongation (Δz). Here f1-f6 presents the data of six microfibers.

Figure 6.11 demonstrates the reproducibility of the response of three sensors during three successive cycles of charge and discharge as well as the corresponding RDS responses. Compared to the reference readings, all microfibers mimic the RDS data closely and reproducibly, indicating the high accuracy and reliability of the developed microfibers. We also note that, overall, there is a reduction in the total amount of expansion, which is reflected in both the RDS as well as the microfibers data.

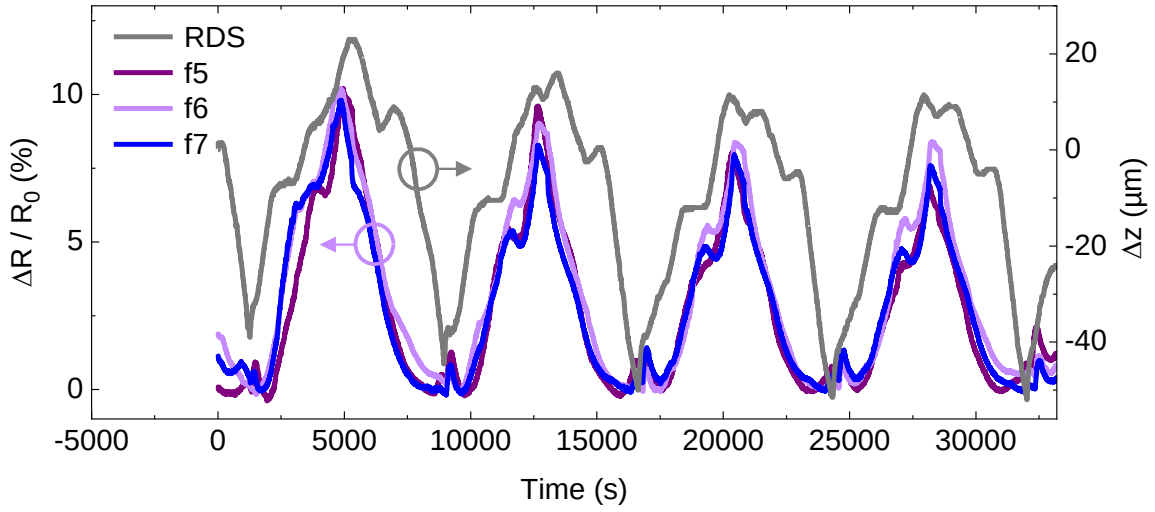

Figure 6.11. The electrical response of the three microfiber sensors (f5-f7) developed in this work and the RDS displacement data measuring the thickness of the Li-ion cell undergoing four consecutive cycles of charging and discharging.

Remarkably, the reproducible signal of the developed economic and versatile microfiber sensors mimics the RDS data as a separate reference instrument. Based on Figure 6.8 to Figure 6.11, using microfibers all phases of cell expansion and contraction are resolved in real-time. Additionally, most commercially available Li-ion pouch cells expand more than 1% of their initial volume.[193–196] Hence, the developed microfiber sensors in this work can be deployed to monitor the volume expansion of commercial Li-ion cells. The simplicity and accuracy of the introduced microfiber in this work indicate its suitability for high-precision Li-ion battery thickness monitoring in a battery management system. Furthermore, using the microfiber sensor, apart from the reversible expansions, it is also possible to monitor the irreversible expansions that occur due to the aging of the cell which could lead to leakage or explosion. Additionally, considering the fast response, low cost, detection limit, resolution, repeatability as well as durability to more than 10,000 cycles of strain, it is

feasible to monitor the volume changes of a Li-ion battery in real-time throughout its lifetime.

Static Thickness Measurement of Li-ion Cell

Table 6.1 shows the summary of the static thickness measurements performed at nine different points on top of the Li-ion cell at the completely discharged and charged states. In a static setting, the thickness of the Li-ion pouch cell (z) is measured at different spots once at 0% state of charge and once at 100%, using a Heidenhain-Metro MT12B. Figure 6.12 shows the pouch cell used in this work with the spots marked on it (as x1 to x9). It is important to note that these thickness measurements are performed in the absence of external pressure or constraints to the pouch cell. Therefore, due to the flexibility of the pouch cover, there are point-to-point differences in the measured thicknesses. Comparing the initial thickness values to the final thicknesses measured, independent from our thickness monitoring setup, indicates inhomogeneity in inflations of the cell that stems from the cell manufacturing process and the pouch foil effects. In our measurement setup, we opted for the springs pressing the four corners of the middle plates, to keep it in touch with the upper side of the cell, applying a slight pressure to it during cycling. These springs mostly distribute the differences in thickness at different points across the plate.

Figure 6.12. Photograph of the Li-ion battery pouch cell used in this work. Spots used for static thickness measurements are marked with x from top left x1 to bottom right x9. The thickness of the cell in the static mode is measured once in a 0% state of charge and once in 100% (not during cycling, but in a fixed state of charge).

Table 6.1. Static thickness measurement data at nine spots on the Li-ion pouch cell.

Location Point	*z at 100% State of charge (mm)*	*z at 0% State of charge (mm)*	*Δz*
1	7.638	7.535	+ 0.103
2	7.798	8.029	- 0.231
3	7.731	7.620	+ 0.111
4	7.575	7.500	+ 0.075
5	7.372	7.385	- 0.013
6	7.956	7.832	+ 0.124
7	7.955	7.868	+ 0.087
8	7.571	7.408	+ 0.163
9	7.876	7.786	+ 0.090

6.2. Summary

In this chapter, based on the promising electromechanical properties of the developed strain sensors three different applications are demonstrated. First, based on the printed composite of 4MS-EVA, impact sensing is show cased by dropping small objects weighing 55 to 648 mg from a short height on the sensor. The response of the sensor shows a linear relationship to the impact energy, a remarkably short response time of 20 ms, and a high resolution in detecting a difference of 1.6 mg in the weight of the dropped objects. Furthermore, as the lightest object hits the surface of the sensor, it outputs a $\Delta R/R_0$ of 10.66% at the peak of impact. Second, the printed sensor is implemented for monitoring the expansion of an inflating diaphragm. While the expandable membrane is inflated to different maxima, the electrical response of the sensor attached to its surface is monitored. Based on the strain sensitivity of the sensor, the applied strain as a result of diaphragm expansions is calculated. Although the applied strain during diaphragm expansion (e.g. $\varepsilon_{calculated}$ =11%) surpasses the work factor of the sensor (ε < 6.7%), the sensor remains reliably responsive. Lastly, the outstanding electromechanical properties of the microfiber sensor developed in this work (and discussed in Chapter 5) motivated its application for dynamic Li-ion battery expansion

monitoring. The electrical response of the microfiber is compared with a commercial displacement sensor during a single charge and discharge cycle as well as four consecutive cycles. The microfiber demonstrates high precision in resolving the different stages of expansion and contraction during charging and discharging, respectively. A high signal-to-noise ratio and reproducible response in full agreement with the reference sensor is demonstrated.

7. Conclusions and Outlook

Although MEMS-based strain sensors with high performance dominate the sensor market, due to the inherent rigidity of the crystalline silicon, the production complexity, and relatively high cost the MEMS sensor performance is limited to rigid surfaces.[197] Stretchable sensors based on a polymer, as complementary to conventional silicon technology, are designed to be mechanically deformable and adaptable to bending and stretching and can be produced in large volumes at low cost. The unique advantages stretchable sensors possess make them a promising choice for a wide range of applications such as human health monitoring, soft robotics, human-machine interfacing, and wearable electronics.[198]

Among various form factors and material designs utilized in stretchable strain sensors, a composite of an insulating elastomer with embedded conductive particle, being fully stretchable, offers an attractive approach to deformability. On the one hand, to take the successful lab-to-fab transition, the electromechanical performance of such sensors has to overcome several challenges such as long response time, low output reproducibility, and low resolution. On another hand, an important technical limitation is a trade-off relationship between high sensitivity and high stretchability.[101,199] Therefore, the sensing range and limits of detection in SPC sensors are designed with respect to the target application.

In this work, as a meaningful contribution to the field, employing high-throughput additive fabrication techniques, the goal is to improve the performance of the composite-based strain sensors and introduce novel industrially relevant applications. The steps taken to achieve this goal are the body of this thesis being explained in Chapters 4 and Chapter 5, with Chapter 6 exploring three application areas that have been left unexplored. Throughout this thesis, as

active sensing elements, conductive core-shell (glass core, nanoscale silver shell) microspheres with a diameter of either 4 µm or 35 µm are utilized.

Chapter 4 begins with exploring the role of elastomer nature in particle-polymer interface formation by comparing EVA and PDMS. Prepared by stencil printing, a composite of 35MS and PDMS or EVA is printed on a stretchable PU substrate. Microstructural studies reveal PDMS allows for a uniform distribution and compact interface while EVA forms a loose layer around clusters of particles promoting their agglomeration. These observations are reflected in a lower electrical percolation threshold of 20% for the 35MS-EVA composite compared to a 34% percolation threshold for 35MS-PDMS. Electromechanical tensile tests suggest EVA is a more promising elastomer compared to PDMS due to is lower hysteresis. Using EVA as the elastomer, the sensing properties of the printed 35MS-EVA sensor are further investigated whereupon a remarkably small detection limit and detection resolution of 0.01% is demonstrated. However, the working range of the 35MS-EVA sensor is strain values below 0.2%. Above 0.2% the onset of the second shoulder in the output signal is observed. To increase the working range and lower the hysteresis, the rest of this chapter revolves around investigating the performance of the 4MS-EVA sensor based on 4 µm conductive particles embedded in the EVA matrix. 4MS-EVA has a percolation threshold of 16%, provides a small detection limit of 0.015%, a detection resolution of 0.025%, and demonstrates highly reproducible electrical response in cyclic strain values ranging form 0.5% to 3%. Response time evaluation during straining and releasing is estimated based on a time-constant difference between the stimulus data and that of the sensor. The electrical response mechanism of the sensor is explained using the tunneling theory. The strain sensitivity and working range of the sensor are estimated to be 7, and 0.067 respectively. Electromechanical durability to 1000 cycles of 1% strain provides evidence of the reproducibility of the developed sensor for small strain sensing applications.

In the final section of this chapter, applying a direct current electric field across the sensor immediately after printing, the possibility of lowering the percolation threshold is investigated. In-situ observation of dynamic percolation via an optical microscope, under low voltages (< 50 V) reveals the alignment of microspheres toward the electrodes in the direction of the electric field. The forces acting on the microspheres and the reasons behind directed percolated network formation are described in Chapter 2. The net force acting on the particles results in the formation of a linear agglomerate connecting the electrodes and

therefore lowering the percolation threshold. To further decrease the percolation threshold, the printed layer is covered to lower the airflow on the wet layer. Another route to lower the percolation is to increase the strength of the electric field, however, as the field increases to 38 V μm^{-1} large clumps form between the electrodes instead of linear structures. Overall, applying an 18 V μm^{-1} yields a 19% percolation threshold, and a 25 V μm^{-1} results in a 14% percolation threshold. The percolation time also decreases from 690 s under 18 V μm^{-1} to 190 s under 25 V μm^{-1}. The finding in this section suggests the directed assembly of microspheres using a DC electric field effectively reduces the percolation threshold. To tune the percolation threshold the strength of the electric field and the processing conditions can be modified.

On the path to further improve the performance of the microsphere-EVA-based sensors, Chapter 5 describes the development of a high-precision free-standing microfiber strain sensor using EVA as the matrix and 4 µm microspheres as the main sensing elements. Wet-spinning as a scalable method is used by which the solvent exchange transforms a composite material from a viscous paste into a long cylindrical fiber. The microstructure morphology investigations using OM and SEM exhibit a compact microstructure in which clusters of agglomerated microspheres are formed within the EVA matrix. A closer look at the EVA-microsphere interface shows a rather loose-layer, as it is discussed in Chapter 4, in comparison to the PDMS-particle interface. The percolation threshold of the 4MS-EVA microfiber is estimated to be 13%. First, tensile destructive tests are carried out to compare the mechanical characteristics of EVA polymer microfibers with those of 4MS-EVA microfibers. Stress-strain plot and the statistical analysis of the results indicate inclusion of solid microspheres in the EVA matrix results in increased elastic modulus, toughness, and yield strength. Whereas the yield strain and elongation at break are decreased. The main reason behind the measured changes is ascribed to the rupture of microsphere-EVA bonds due to the polymer toughenning, an effect that is typically observed in filled-elastomers. This phenomenon prohibits chain re-orientation and elongation to accommodate the strain inside the matrix. The sensing mechanism of the microfiber, over the entire electrically conductive range, exhibits good agreement with the formulations based on the tunneling theory. 4MS-EVA microfibers show a mean strain sensitivity of 9.1 and a mean working factor of 0.139. Investigating the minimum detection limit under nine sequential cycles of 0.005%-0 demonstrates a highly reproducible as well as easily detectable sensor response. This remarkable detection limit is equivalent to detecting a 1 µm elongation over a 20 mm active

sensing length. Furthermore, the ability to detect a change in the applied strain is tested under sequentially increasing strain-release cycles from 0.005% up to 0.025% in +0.005% strain steps. The microfiber is capable of resolving a 0.005% strain change by clear signal differences. The reported sensing and resolution limits are the lowest compared to the reported piezoresistive works. The high repeatability of the sensor response is demonstrated under 10 repetitive 1% strain cycles with a fast strain rate of 900 mm min^{-1}. Based on the fast-rate test the time constant (response time) of the microfiber sensor is statistically estimated to be 15.3 ms for straining and 40.6 ms for relaxing. The fast response allows for realtime detection of strain in the respective application. The electromechanical durability of the microfiber to overload strain is examined under repetitive cycles of 12% and 25% under 900 mm min^{-1} and 100 mm min^{-1} strain rates, respectively. Remarkable is that, even though at the peak of strain the sensor is electrically disconnected, as the sensor relaxes it becomes conductive again. Furthermore, the electromechanical durability of the microfiber against > 10,000 cycles of 1% strain shows a highly reproducible signal when comparing the sensor response during the 1000^{th} cycle with the 10250^{th} cycle. Overall, leaving out the substrate, the 4MS-EVA microfiber reaches a record low-resolution limit and minimum detection limit, a shorter response time, and a higher signal reproducibility.

Noteworthy is that the electromechanical hysteresis is observed in results presented in Chapter 4 and Chapter 5. Meaning in the printed sensor on the PU substrate and when the sensor is a stand-alone microfiber there is hysteresis in its signal. The observed hysteresis appears especially during the overload strain tests at the relaxed-state response level. Additionally, when the sensor is subjected to a large-number cyclic test the onset of the shoulder peak as the cycle number increases is another symptom of hysteresis. The main reason behind these types of strain-history dependant responses in a polymer-based strain sensor, as explained in Chapter 2, stems from the inherent viscoelasticity of an elastomer. However, when involving the substrate, as a secondary elastomer, as discussed in Chapter 4, the hysteresis is stronger compared to the substrate-free microfiber sensor.

The performance characteristics of the developed sensors, based on the findings in this thesis (Chapter 4 and Chapter 5), are promising for application areas where high-resolution strain sensing in small strain is the focus. While the majority of strain sensors reported in the literature have chosen human health or body-part motion detection to show-case the applicability of the sensor, in Chapter 6 we aim for impact sensing and Li-ion expansion

monitoring. To facilitate the benchmarking with the literature we also reported the diaphragm expansion monitoring.

Impact sensing by the printed sensor on the PU substrate is performed using small solid objects weighing a maximum of 680 mg dropped from a close distance (60 mm) on top of the sensor. A fast response time of 20 ms, independent of the weight of the objects, is recorded. Correlating the sensor's response to the impact energy exerted on the sensor exhibits a linear relationship between the two. Remarkable is the pinpointing of a very small impact energy difference (< 1 µJ corresponding to Δm =1.6 mg) with an easily detectable signal change (1.2%). The key implication of this section is that the printed sensor attached to a surface is capable of detecting very small impacts applied on the surface with a high signal-to-noise ratio.

For the diaphragm expansion monitoring by the printed sensor, pressurized air is sequentially pumped into and out of a container that has a stretchable PU as the diaphragm attached to it. The sensor is attached to the diaphragm while its signal is recorded simultaneously. Here the maximum strain applied to the sensor is estimated to reach 14% which is well above its working range $\varepsilon < 6.7\%$. The main conclusion of this section is that the printed sensor endures overload strains during the respective application while remaining reliably responsive for subsequent sudden surface expansions.

Lastly, Li-ion battery expansion monitoring using the 4MS-EVA microfiber sensor, as an unconventional application for a piezoresistive sensor is demonstrated. The setup for this application is prepared using three solid sheets where the middle sheet is vertically displaceable. A lab-made Li-ion cell with the NMC composition is placed between two lower sheets. Around these sheets, seven microfibers are attached vertically. On top of the setup, a reference sensor is installed. Simultaneous with charging and discharging the Li-ion cell, the response of the microfibers and the reference sensor are recorded. As the battery is charged in the CC mode it expands and as soon as charging in the CV mode starts, the cell contraction starts. Further, during the discharging in the CC mode, the cell contraction continues until reaching the initial thickness by the time the battery is discharged. The phases of expansion and contraction are accurately recorded by the microfibers following the courses of the reference sensor. At the peak of the cell expansion, calculated based on the microfiber response and the strain sensitivity of 7 (discussed in Chapter 5), one of the microfibers experienced an elongation of 80 µm. Comparing the electrical response of six

microfibers with one another, each microfibers closely mirrored the the rest, exhibiting reproducibility of the sensor signal. Overall, the slight difference between the displacement the reference sensor recorded (62 µm) and the elongation the microfibers experienced is attributed to the difference in the location of the sensors. The repeatability of the microfibers is examined under four consecutive cycles of charge and discharge. The three microfibers exhibit identical signal changes throughout the test and closely follow the reference sensor. The key finding of this section is that microfiber as an economic and high-precision sensor can be reliably employed for Li-ion battery expansion monitoring. The approaches presented in this work, highlight that combined with the fast strain detection response, high resolution, and mechanical durability, the developed sensors tackle the sensing limits reported so far and their relevance for technological applications is demonstrated.

Outlook

In accordance with the respective application area, a piezoresistive particle-polymer sensor should be designed. The close relationship between the fabrication method and material performance underlines the importance of an application-oriented sensor design. When pushing the sensing boundaries through novel structures, it is crucial to account for the time and energy expended to ensure a smooth lab-to-fab transition. This work presents an approach that highlights the modifications made to a sensor printed on a substrate when the same composite is utilized in a stand-alone architecture. For example, if the application necessitates surface sensing, wherein the printed sensor on a substrate is the preferred solution, the cross-compatibility of the substrate material with the elastomer becomes essential. Additionally, the nature of the elastomer affecting the performance of the composite outlines another key aspect requiring careful attention in sensor design. Due to the inherent viscoelasticity of elastomers, and the inevitable alterations introduced to the matrix structure by incorporating solid particles, there is not a single optimal set of performance criteria to opt for when developing a piezoresistive sensor. Nevertheless, the availability of versatile conductive and elastomer materials enables a flexible and application-tailored approach to sensor design.

Looking forward, one solution to the hysteresis problem can be the improved engineering of the interfaces to prevent early damage during cycling, that is by optimizing the polymer adhesion to the particle surface or using conductive hydrogels instead of viscoelastic

polymers.[200] The longer response time observed when the sensor is relaxed stems from the weak binding with conductive fillers causing slow recovery when strain is released. However, very strong interfacial binding could result in earlier fracture of microstructure due to decreased polymer chain mobility. Therefore, according to the target application, particularly the detection limit and resolution, the particle-polymer interface can be optimized, without sacrificing the desired outcome. One side note is that, in doing so, the fabrication process might become complicated and costly. Also, there is always a trade-off relationship between a very low detection limit and high stretchability. Another strategy can be leveraging machine learning to analyze the hysteresis in the developed sensor and improve sensor error.[201] Future work can be dedicated to applying the free-standing microfiber for different battery form factors. Using printed sensors for higher-impact shocks sounds like an interesting avenue to explore further. To extend the linear working range of the developed sensors it is speculated that using hydrogels instead of EVA or microsphere surface functionlization can be another focus for future studies.

Appendices

Appendix A4.1.

Table A4.1. Key sensing characteristics of the developed strain sensors in this work compared with the reported piezoresistive strain sensors in the literature in recent years.

Ref.	*Minimum Strain Detection Limit (%)*	*Minimum Strain Detection Resolution (%)*	*Response Time (ms)*	*Sensor Form | Sensor Material*
MS-EVA Printed Sensor (Chapter 4)[126]	0.01	0.01	20	Film | PU substrate /EVA/Ag-glass core-shell microspheres
MS-EVA Microfiber Sensor (Chapter5)[148]	0.005	0.005	11	Fiber | EVA/Ag-glass microspheres
[39]	0.01	0.04	70	Fiber | rubber/polypropylene fiber sheath/CNT
[202]	0.01	0.04	60	Fiber | TPU/CNT+TPU
[203]	0.01	0.04	24	Film | Poly ether ketone substrate/graphene
[204]	0.01	0.1	22	Film | Au NW/various elastic substrates
[131]	0.01	0.5	100	Fiber | PU/Graphene/PVDF nanoballs
[205]	0.02	NA	170	Film | polyhedral cobalt nanoporous carbon/graphene/SEBS
[206]	0.02	NA	200	Film | polymerized perfluoro phenyl methacrylate/PDMS
[129]	0.05	0.05	147	Film | Polyacrylamide organohydrogel microsphere/Ecoflex
[154]	0.05	0.05	58	Film | PDMS liquid metal
[58]	0.05	NA	200	Film | PDMS/CB/PEN
[207]	0.05	0.05	28	Film | CB/natural rubber latex
[57]	0.1	NA	50	Film | PDMS/CB
[130]	0.3	0.3	NA	Film | PDMS/Au coated glass microspheres/PDMS
[81]	0.3	0.1	300	Film | CNT/silicone elastomer/silica nanoparticles
[60]	0.5	0.5	70	Fibrous mat | CNT/TPU
[208]	1	NA	230	Film | natural rubber/modified MWCNT

Appendix A5.1.

Table A5.1. Parameters derived from fitting Equation 5.2 to the experimental data of $\Delta R/R_0$.

Fitting Parameters	A	B	C	D	E	F
Fitted Values	0.17668	-0.00519	-8.10133E-4	2.56995E-5	0.01408	26.25327

Appendix A5.2.

Table A5.2. The mean strain sensitivity and working factor of 10 4MS-EVA microfibers.

Statistical descriptive parameters	Mean	StdDev
Strain sensitivity	9.1	1.7
Working factor	0.139	0.029

Appendix A5.3.

Table A5.3. The smallest strain sensing limit and smallest resolution of 4MS-EVA microfiber compared with the reported piezoresistive strain sensors in the literature.

Ref.	*Minimum resolution (%)*	*Minimum detection limit (%)*	*Strain sensor form*	*Strain sensing mechanism*	*Fabrication method*	*Material*
[62]	0.5	0.5	Fiber	PZ. (1), PC. (2)	Coaxial wet spinning	SBS/SBS-multiwalled (MW) CNT
[209]	0.5	0.5	Fiber	PZ., PC., Crk. (3)	Dip-coating	Elastic filament/ polyethylene terephthalate (PET)/CNT
[210]	0.5	NA.(4)	Film	Crk.	Magnetron sputtering	Polyimide substrate/ Cu-Al film
[166]	0.2	0.3	Fiber	PZ.	Dip coating	Polyurethane (PU) yarn/polyethylene (PE) /reduced graphene oxide
[211]	0.15	0.15	Film	PZ.	Stencil lithography	PET/Au/Au NP
[34]	0.1	0.1	Fiber	PZ., PC.	Dip coating	PU yarn/carbon black/cellulose/nanocrystals/natural rubber/chitosan
[82]	0.1	0.1	Fiber	PZ., PC.	Microfluidic	MWCNT + hydrogel
[212]	0.1	0.1	Fiber	Crk.	Dip-coating	PU yarn/ Bovine serum albumin/reduced graphene oxide
[213]	0.5	0.09	Fiber	Plasmon resonance	Molding + dip coating	PDMS + Au nanoparticles/PDMS
[214]	0.08	0.09	Foam	PZ., PC.	Chemical vapor deposition	Graphene fragmentized foam/PDMS
[142]	0.07	NA.	Fiber	PZ., PC.	Emulsification	PDMS/graphene
[215]	0.065	NA.	Fiber	PZ., PC.	Dispersion + interpenetration	Polyolefin nanofiber yarn/Ag nanowire
[41]	0.05	0.05	Film	PZ., PC.	Electrospinning	Thermoplastic polyurethane (TPU) fibrous mate/CNT
[216]	0.05	0.35	Film	PZ., PC.	Blade coating	PDMS/reduced graphene oxide flakes

[217]	0.05	0.1	Fiber	Ion transmission	Wet spinning	TPU/Ionic liquid
[51]	0.05	NA.	Film	PZ., Crk.	Screen printing	PDMS/CB or Ag/SBS
[218]	0.033	0.34	Film	Piezotronic tunneling junction	Chemical vapor deposition	Ag electrodes/HfO_2(insulator)/n-ZnO NW
[219]	0.02	NA.	Fabric	PZ., Crk.	Thermal treatment	Carbonized cellulose fabric/Ecoflex
[220]	0.02	0.02	Fabric	PZ., layer buckling	Chemical vapor deposition	Graphene/Ecoflex
[39]	0.01	0.04	Fiber	PZ.	Dip coating	Rubber/polypropylene fiber sheath/CNT
[202]	0.01	0.04	Fiber	PZ., Crk.	Coaxial wet spinning	TPU/CNT+TPU
[203]	0.01	0.04	Film	PZ., Crk.	Laser-induced carbonization	Polyether ketone substrate/graphene
[204]	0.01	0.1	Film	PZ., PC.	Drop casting	Au NW/various elastic substrates
[131]	0.01	0.5	Fiber	PZ., PC.	Wet spinning	PU/Graphene/PVDF Nano balls
This work	0.005	0.005	Fiber	PZ., PC.	Wet spinning	EVA + Ag-SLG core-shell microspheres

(1) PZ.: piezoresistive, (2) PC.: percolative, (3) Crk.: crack based, (4) NA.: not available.

Appendix A5.4.

Table A5.4. Summary of the statistical analysis of delay in response time of 10 identical MS-EVA microfibers when a 1% strain is applied and released.

Statistical descriptive parameters	Mean	StdDev
Straining (ms)	15.3	6.7
Relaxing (ms)	40.6	8.6

Appendix A5.5.

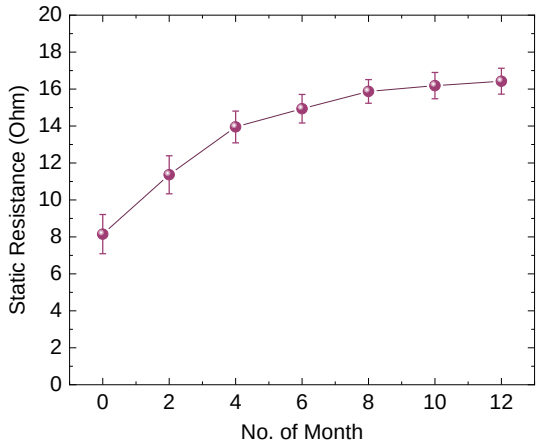

Figure A5.5. The long-term stability of developed 4MS-EVA microfiber. Static 2-probe resistance measurements of eight microfibers are performed under controlled ambient conditions, 20°C ± 2, RH 45% ± 5), at one-month intervals within a year (using a SMU).

References

[1] L. Feldman Barrett, *Seven and a Half Lessons about the Brain*, Mariner Books, New York, US, **2021**.

[2] J. Fraden, *Handbook of Modern Sensors | Physics, Designs, and Applications*, Springer, San Diego, CA, USA, **2016**.

[3] S. Gujar, D. Vishwakarma, "Smart Sensor Market, Forecast 2023 - 2032, By Global Market Insights Inc.," **n.d.**

[4] A. Ehrmann, *Micromachines* **2023**, *14*, DOI 10.3390/mi14122195.

[5] M. Baumgartner, F. Hartmann, M. Drack, D. Preninger, D. Wirthl, R. Gerstmayr, L. Lehner, G. Mao, R. Pruckner, S. Demchyshyn, L. Reiter, M. Strobel, T. Stockinger, D. Schiller, S. Kimeswenger, F. Greibich, G. Buchberger, E. Bradt, S. Hild, S. Bauer, M. Kaltenbrunner, *Nat. Mater.* **2020**, *19*, 1102.

[6] K. Kim, B. Kim, C. H. Lee, *Adv. Mater.* **2020**, *32*, 1902051.

[7] J. Kim, M. Lee, H. J. Shim, R. Ghaffari, H. R. Cho, D. Son, Y. H. Jung, M. Soh, C. Choi, S. Jung, K. Chu, D. Jeon, S.-T. Lee, J. H. Kim, S. H. Choi, T. Hyeon, D.-H. Kim, *Nat. Commun.* **2014**, *5*, 5747.

[8] D.-H. Kim, N. Lu, R. Ma, Y.-S. Kim, R.-H. Kim, S. Wang, J. Wu, S. M. Won, H. Tao, A. Islam, K. J. Yu, T. Kim, R. Chowdhury, M. Ying, L. Xu, M. Li, H.-J. Chung, H. Keum, M. McCormick, P. Liu, Y.-W. Zhang, F. G. Omenetto, Y. Huang, T. Coleman, J. A. Rogers, *Science* **2011**, *333*, 838.

[9] A. D. Mickle, S. M. Won, K. N. Noh, J. Yoon, K. W. Meacham, Y. Xue, L. A. McIlvried, B. A. Copits, V. K. Samineni, K. E. Crawford, D. H. Kim, P. Srivastava, B. H. Kim, S. Min, Y. Shiuan, Y. Yun, M. A. Payne, J. Zhang, H. Jang, Y. Li, H. H. Lai, Y. Huang, S.-I. Park, R. W. Gereau, J. A. Rogers, *Nature* **2019**, *565*, 361.

[10] H. Luan, Y. Zhang, *Adv. Intell. Syst.* **2021**, *3*, 2000228.

[11] Y. J. Hong, H. Jeong, K. W. Cho, N. Lu, D.-H. Kim, *Adv. Funct. Mater.* **2019**, *29*, 1808247.

[12] H. Souri, H. Banerjee, A. Jusufi, N. Radacsi, A. A. Stokes, I. Park, M. Sitti, M. Amjadi, *Adv. Intell. Syst.* **2020**, *2*, 2000039.

[13] C. Tan, Z. Dong, Y. Li, H. Zhao, X. Huang, Z. Zhou, J.-W. Jiang, Y.-Z. Long, P. Jiang, T.-Y. Zhang, B. Sun, *Nat. Commun.* **2020**, *11*, 3530.

[14] X. Shi, Y. Zuo, P. Zhai, J. Shen, Y. Yang, Z. Gao, M. Liao, J. Wu, J. Wang, X. Xu, Q. Tong, B. Zhang, B. Wang, X. Sun, L. Zhang, Q. Pei, D. Jin, P. Chen, H. Peng, *Nature* **2021**, *591*, 240.

[15] W. Weng, Q. Sun, Y. Zhang, S. He, Q. Wu, J. Deng, X. Fang, G. Guan, J. Ren, H. Peng, *Adv. Mater.* **2015**, *27*, 1363.

[16] W. Lee, Y. Liu, Y. Lee, B. K. Sharma, S. M. Shinde, S. D. Kim, K. Nan, Z. Yan, M.

Han, Y. Huang, Y. Zhang, J.-H. Ahn, J. A. Rogers, *Nat. Commun.* **2018**, *9*, 1417.

[17] H. Fu, K. Nan, W. Bai, W. Huang, K. Bai, L. Lu, C. Zhou, Y. Liu, F. Liu, J. Wang, M. Han, Z. Yan, H. Luan, Y. Zhang, Y. Zhang, J. Zhao, X. Cheng, M. Li, J. W. Lee, Y. Liu, D. Fang, X. Li, Y. Huang, Y. Zhang, J. A. Rogers, *Nat. Mater.* **2018**, *17*, 268.

[18] S. Xu, Y. Zhang, L. Jia, K. E. Mathewson, K.-I. Jang, J. Kim, H. Fu, X. Huang, P. Chava, R. Wang, S. Bhole, L. Wang, Y. J. Na, Y. Guan, M. Flavin, Z. Han, Y. Huang, J. A. Rogers, *Science* **2014**, *344*, 70.

[19] D.-Y. Khang, H. Jiang, Y. Huang, J. A. Rogers, *Science* **2006**, *311*, 208.

[20] S. Yang, E. Ng, N. Lu, *Extrem. Mech. Lett.* **2015**, *2*, 37.

[21] S. Zhang, Y. Li, Q. Tian, L. Liu, W. Yao, C. Chi, P. Zeng, N. Zhang, W. Wu, *J. Mater. Chem. C* **2018**, *6*, 3999.

[22] K.-I. Jang, K. Li, H. U. Chung, S. Xu, H. N. Jung, Y. Yang, J. W. Kwak, H. H. Jung, J. Song, C. Yang, A. Wang, Z. Liu, J. Y. Lee, B. H. Kim, J.-H. Kim, J. Lee, Y. Yu, B. J. Kim, H. Jang, K. J. Yu, J. Kim, J. W. Lee, J.-W. Jeong, Y. M. Song, Y. Huang, Y. Zhang, J. A. Rogers, *Nat. Commun.* **2017**, *8*, 15894.

[23] E. Okogbue, S. S. Han, T.-J. Ko, H.-S. Chung, J. Ma, M. S. Shawkat, J. H. Kim, J. H. Kim, E. Ji, K. H. Oh, L. Zhai, G.-H. Lee, Y. Jung, *Nano Lett.* **2019**, *19*, 7598.

[24] Z. Song, T. Ma, R. Tang, Q. Cheng, X. Wang, D. Krishnaraju, R. Panat, C. K. Chan, H. Yu, H. Jiang, *Nat. Commun.* **2014**, *5*, 3140.

[25] Y. Luo, M. R. Abidian, J.-H. Ahn, D. Akinwande, A. M. Andrews, M. Antonietti, Z. Bao, M. Berggren, C. A. Berkey, C. J. Bettinger, J. Chen, P. Chen, W. Cheng, X. Cheng, S.-J. Choi, A. Chortos, C. Dagdeviren, R. H. Dauskardt, C. Di, M. D. Dickey, X. Duan, A. Facchetti, Z. Fan, Y. Fang, J. Feng, X. Feng, H. Gao, W. Gao, X. Gong, C. F. Guo, X. Guo, M. C. Hartel, Z. He, J. S. Ho, Y. Hu, Q. Huang, Y. Huang, F. Huo, M. M. Hussain, A. Javey, U. Jeong, C. Jiang, X. Jiang, J. Kang, D. Karnaushenko, A. Khademhosseini, D.-H. Kim, I.-D. Kim, D. Kireev, L. Kong, C. Lee, N.-E. Lee, P. S. Lee, T.-W. Lee, F. Li, J. Li, C. Liang, C. T. Lim, Y. Lin, D. J. Lipomi, J. Liu, K. Liu, N. Liu, R. Liu, Y. Liu, Y. Liu, Z. Liu, Z. Liu, X. J. Loh, N. Lu, Z. Lv, S. Magdassi, G. G. Malliaras, N. Matsuhisa, A. Nathan, S. Niu, J. Pan, C. Pang, Q. Pei, H. Peng, D. Qi, H. Ren, J. A. Rogers, A. Rowe, O. G. Schmidt, T. Sekitani, D.-G. Seo, G. Shen, X. Sheng, Q. Shi, T. Someya, Y. Song, E. Stavrinidou, M. Su, X. Sun, K. Takei, X.-M. Tao, B. C. K. Tee, A. V.-Y. Thean, T. Q. Trung, C. Wan, H. Wang, J. Wang, M. Wang, S. Wang, T. Wang, Z. L. Wang, P. S. Weiss, H. Wen, S. Xu, T. Xu, H. Yan, X. Yan, H. Yang, L. Yang, S. Yang, L. Yin, C. Yu, G. Yu, J. Yu, S.-H. Yu, X. Yu, E. Zamburg, H. Zhang, X. Zhang, X. Zhang, X. Zhang, Y. Zhang, Y. Zhang, S. Zhao, X. Zhao, Y. Zheng, Y.-Q. Zheng, Z. Zheng, T. Zhou, B. Zhu, M. Zhu, R. Zhu, Y. Zhu, Y. Zhu, G. Zou, X. Chen, *ACS Nano* **2023**, *17*, 5211.

[26] Y. Luo, M. Wang, C. Wan, P. Cai, X. J. Loh, X. Chen, *Adv. Mater.* **2020**, *32*, 2001903.

[27] Y. Huang, C. Peng, Y. Li, Y. Yang, W. Feng, *Aggregate* **2023**, *4*, e319.

[28] Q. Peng, J. Chen, T. Wang, X. Peng, J. Liu, X. Wang, J. Wang, H. Zeng, *InfoMat* **2020**, *2*, 843.

[29] Z. Wang, H. Zhou, J. Lai, B. Yan, H. Liu, X. Jin, A. Ma, G. Zhang, W. Zhao, W. Chen, *J. Mater. Chem. C* **2018**, *6*, 9200.

[30] M. Mehrali, S. Bagherifard, M. Akbari, A. Thakur, B. Mirani, M. Mehrali, M. Hasany, G. Orive, P. Das, J. Emneus, T. L. Andresen, A. Dolatshahi-Pirouz, *Adv. Sci.* **2018**, *5*, 1700931.

[31] X. Sun, X. Wang, B. Yuan, J. Liu, *Mater. Today Phys.* **2020**, *14*, 100245.

[32] C. B. Cooper, K. Arutselvan, Y. Liu, D. Armstrong, Y. Lin, M. R. Khan, J. Genzer, M. D. Dickey, *Adv. Funct. Mater.* **2017**, *27*, 1605630.

[33] S. Zhu, J.-H. So, R. Mays, S. Desai, W. R. Barnes, B. Pourdeyhimi, M. D. Dickey, *Adv. Funct. Mater.* **2013**, *23*, 2308.

[34] X. Wu, Y. Han, X. Zhang, C. Lu, *ACS Appl. Mater. Interfaces* **2016**, *8*, 9936.

[35] B. Niu, S. Yang, Y. Yang, T. Hua, *SmartMat* **2023**, *4*, e1178.

[36] Y. Zheng, Y. Li, Z. Li, Y. Wang, K. Dai, G. Zheng, C. Liu, C. Shen, *Compos. Sci. Technol.* **2017**, *139*, 64.

[37] H. Yang, L. H. Gong, Z. Zheng, X. F. Yao, *Carbon N. Y.* **2020**, *158*, 893.

[38] Y. Yu, Y. Zhai, Z. Yun, W. Zhai, X. Wang, G. Zheng, C. Yan, K. Dai, C. Liu, C. Shen, *Adv. Electron. Mater.* **2019**, *5*, 1900538.

[39] L. Lu, Y. Zhou, J. Pan, T. Chen, Y. Hu, G. Zheng, K. Dai, C. Liu, C. Shen, X. Sun, H. Peng, *ACS Appl. Mater. Interfaces* **2019**, *11*, 4345.

[40] G. Spinelli, P. Lamberti, V. Tucci, L. Vertuccio, L. Guadagno, *Compos. Part B Eng.* **2018**, *145*, 90.

[41] H. Li, J. Chen, X. Chang, Y. Xu, G. Zhao, Y. Zhu, Y. Li, *J. Mater. Chem. A* **2021**, *9*, 1795.

[42] S. Lee, S. Shin, S. Lee, J. Seo, J. Lee, S. Son, H. J. Cho, H. Algadi, S. Al-Sayari, D. E. Kim, T. Lee, *Adv. Funct. Mater.* **2015**, *25*, 3114.

[43] W. Pan, J. Wang, Y.-P. Li, X.-B. Sun, J.-P. Wang, X.-X. Wang, J. Zhang, H.-D. You, G.-F. Yu, Y.-Z. Long, *Polymers (Basel).* **2020**, *12*, 339.

[44] S. Liu, Y. Lin, Y. Wei, S. Chen, J. Zhu, L. Liu, *Compos. Sci. Technol.* **2017**, *146*, 110.

[45] F. Yin, H. Lu, H. Pan, H. Ji, S. Pei, H. Liu, J. Huang, J. Gu, M. Li, J. Wei, *Sci. Rep.* **2019**, *9*, 2403.

[46] J. Sun, Y. Li, Q. Peng, S. Hou, D. Zou, Y. Shang, Y. Li, P. Li, Q. Du, Z. Wang, Y. Xia, L. Xia, X. Li, A. Cao, *ACS Nano* **2013**, *7*, 10225.

[47] Z. Xu, Z. Liu, H. Sun, C. Gao, *Adv. Mater.* **2013**, *25*, 3249.

[48] H. Jang, Y. J. Park, X. Chen, T. Das, M.-S. Kim, J.-H. Ahn, *Adv. Mater.* **2016**, *28*, 4184.

[49] J. Park, J. C. Hwang, G. G. Kim, J.-U. Park, *InfoMat* **2020**, *2*, 33.

[50] Y. Hu, X. Liu, L. Tian, T. Zhao, H. Wang, X. Liang, F. Zhou, P. Zhu, G. Li, R. Sun, C.-P. Wong, *ACS Appl. Mater. Interfaces* **2018**, *10*, 38493.

[51] Y.-F. Wang, T. Sekine, Y. Takeda, J. Hong, A. Yoshida, H. Matsui, D. Kumaki, T. Nishikawa, T. Shiba, T. Sunaga, S. Tokito, *ACS Appl. Mater. Interfaces* **2020**, *12*, 35282.

[52] C. Ning, K. Dong, R. Cheng, J. Yi, C. Ye, X. Peng, F. Sheng, Y. Jiang, Z. L. Wang, *Adv. Funct. Mater.* **2021**, *31*, 2006679.

[53] Y. Lu, J. Jiang, S. Yoon, K.-S. Kim, J.-H. Kim, S. Park, S.-H. Kim, L. Piao, *ACS Appl. Mater. Interfaces* **2018**, *10*, 2093.

[54] S. Chen, Y. Wei, S. Wei, Y. Lin, L. Liu, *ACS Appl. Mater. Interfaces* **2016**, *8*, 25563.

[55] M. Zu, Q. Li, G. Wang, J.-H. Byun, T.-W. Chou, *Adv. Funct. Mater.* **2013**, *23*, 789.

[56] L. Su, M. Liang, J. Wang, X. Xin, Y. Jiao, C. Wang, Y. Zhang, Z. Yao, *Chem. Eng. J.* **2023**, *468*, 143564.

[57] A. Yoshida, Y.-F. Wang, T. Sekine, Y. Takeda, D. Kumaki, S. Tokito, *ACS Appl. Eng. Mater.* **2023**, *1*, 50.

[58] Y. F. Wang, A. Yoshida, Y. Takeda, T. Sekine, D. Kumaki, S. Tokito, *Sensors* **2023**, *23*, 5041.

[59] J. Gao, X. Wang, W. Zhai, H. Liu, G. Zheng, K. Dai, L. Mi, C. Liu, C. Shen, *ACS Appl. Mater. Interfaces* **2018**, *10*, 34592.

[60] M. Ren, Y. Zhou, Y. Wang, G. Zheng, K. Dai, C. Liu, C. Shen, *Chem. Eng. J.* **2019**, *360*, 762.

[61] Y. Zhang, C. Li, B. Zhou, H. He, Y. Zhou, L. Jiang, F.-L. Zhou, S. Chen, *J. Appl. Polym. Sci.* **2022**, *139*, e52475.

[62] W. Li, Y. Zhou, Y. Wang, L. Jiang, J. Ma, S. Chen, F.-L. Zhou, *Adv. Electron. Mater.* **2021**, *7*, 2000865.

[63] B. Zhou, Z. Liu, C. Li, M. Liu, L. Jiang, Y. Zhou, F.-L. Zhou, S. Chen, S. Jerrams, J. Yu, *Adv. Electron. Mater.* **2021**, *7*, 2100233.

[64] P. Costa, A. Maceiras, M. San Sebastián, C. García-Astrain, J. L. Vilas, S. Lanceros-Mendez, *J. Mater. Chem. C* **2018**, *6*, 10580.

[65] H.-R. Lim, H. S. Kim, R. Qazi, Y.-T. Kwon, J.-W. Jeong, W.-H. Yeo, *Adv. Mater.* **2020**, *32*, 1901924.

[66] T. Li, J. Li, A. Zhong, F. Han, R. Sun, C.-P. Wong, F. Niu, G. Zhang, Y. Jin, *Sensors Actuators A Phys.* **2020**, *306*, 111959.

[67] Z. Su, H. Chen, Y. Song, X. Cheng, X. Chen, H. Guo, L. Miao, H. Zhang, *Small* **2017**, *13*, 1702108.

[68] T. Bardelli, C. Marano, F. Briatico Vangosa, *J. Appl. Polym. Sci.* **2021**, *138*, 51013.

[69] Z. Li, X. Qi, L. Xu, H. Lu, W. Wang, X. Jin, Z. I. Md, Y. Zhu, Y. Fu, Q. Ni, Y. Dong, *ACS Appl. Mater. Interfaces* **2020**, *12*, 42179.

[70] D. Xiang, J. Li, Z. Li, X. Zhang, C. Zhao, H. Li, J. Lai, B. Wang, P. Wang, D. Li, Y. Wu, *Sensors Actuators A Phys.* **2024**, *366*, 114992.

[71] X. Qi, W. Wang, H. Dai, Y. Zhu, Y. Dong, S.-Y. Fu, Q. Ni, Y. Fu, *Compos. Part A Appl. Sci. Manuf.* **2023**, *169*, 107521.

[72] J. Wang, G. Cai, S. Li, D. Gao, J. Xiong, P. S. Lee, *Adv. Mater.* **2018**, *30*, 1706157.

[73] M. Kempe, in *2011 37th IEEE Photovolt. Spec. Conf.*, **2011**, pp. 85–90.

[74] B. Long, X. Zhou, H. Cao, R. Chen, N. He, L. Chi, P. Fan, X. Chen, *Front. Mater.* **2022**, *9*, DOI 10.3389/fmats.2022.892657.

[75] D. Wu, P. Wessel, J. Zhu, D. Montiel-Chicharro, T. R. Betts, A. Mordvinkin, R. Gottschalg, *Materials (Basel).* **2023**, *16*, DOI 10.3390/ma16216945.

[76] S. M. Eskandarabadi, M. Mahmoudian, K. R. Farah, A. Abdali, E. Nozad, M. Enayati, *Food Packag. Shelf Life* **2019**, *22*, 100389.

[77] J. Zhou, X. Xu, Y. Xin, G. Lubineau, *Adv. Funct. Mater.* **2018**, *28*, 1705591.

[78] J. Lee, S. Kim, J. Lee, D. Yang, B. C. Park, S. Ryu, I. Park, *Nanoscale* **2014**, *6*, 11932.

[79] S.-M. Jeong, Y. Kang, T. Lim, S. Ju, *Adv. Mater. Interfaces* **2018**, *5*, 1801376.

[80] J. Zhou, X. Xu, H. Yu, G. Lubineau, *Nanoscale* **2017**, *9*, 604.

[81] Z. Tang, S. Jia, X. Shi, B. Li, C. Zhou, *Polymers (Basel).* **2019**, *11*, 666.

[82] D. Kim, J. Yoon, *ACS Appl. Mater. Interfaces* **2020**, *12*, 20965.

[83] I. Krupa, J. Prokeš, I. Křivka, Z. špitalský, in *Handb. Multiph. Polym. Syst.*, **2011**, pp. 425–477.

[84] Y. E. Elnemr, A. Abu-Libdeh, G. C. Raj, Y. Birjis, H. Nazemi, P. Munirathinam, A. Emadi, *Sensors* **2023**, *23*, DOI 10.3390/s23094457.

[85] M. Amjadi, K.-U. Kyung, I. Park, M. Sitti, *Adv. Funct. Mater.* **2016**, *26*, 1678.

[86] K. Ohe, Y. Naito, *Jpn. J. Appl. Phys.* **1971**, *10*, 99.

[87] X.-W. Zhang, Y. Pan, Q. Zheng, X.-S. Yi, *J. Polym. Sci. Part B Polym. Phys.* **2000**, *38*, 2739.

[88] H. Liu, Q. Li, S. Zhang, R. Yin, X. Liu, Y. He, K. Dai, C. Shan, J. Guo, C. Liu, C. Shen, X. Wang, N. Wang, Z. Wang, R. Wei, Z. Guo, *J. Mater. Chem. C* **2018**, *6*, 12121.

[89] J. G. Simmons, *J. Appl. Phys.* **1963**, *34*, 238.

[90] J. G. Simmons, *J. Appl. Phys.* **1963**, *34*, 1793.

[91] J. G. Simmons, G. J. Unterkofler, *J. Appl. Phys.* **1963**, *34*, 1828.

[92] J. G. Simmons, *J. Appl. Phys.* **1963**, *34*, 2581.

[93] X. Wang, X. Liu, D. W. Schubert, *Nano-Micro Lett.* **2021**, *13*, 64.

[94] C. M. Hansen, *Hansen Solubility Parameters: A User's Handbook, Second Edition*, CRC Press, **2007**.

[95] C. M. Hansen, *Prod. R&D* **1969**, *8*, 2.

[96] J. Camacho, E. Díez, I. Díaz, G. Ovejero, *Polym. Int.* **2017**, *66*, 1013.

[97] C. Lozano-Pérez, J. V Cauich-Rodríguez, F. Avilés, *Compos. Sci. Technol.* **2016**, *128*, 25.

[98] L. Duan, S. Fu, H. Deng, Q. Zhang, K. Wang, F. Chen, Q. Fu, *J. Mater. Chem. A* **2014**, *2*, 17085.

[99] J. Tang, Y. Wu, S. Ma, T. Yan, Z. Pan, *ACS Appl. Mater. Interfaces* **2023**, *15*, 7392.

[100] H. Liu, J. Gao, W. Huang, K. Dai, G. Zheng, C. Liu, C. Shen, X. Yan, J. Guo, Z. Guo, *Nanoscale* **2016**, *8*, 12977.

[101] L. Duan, D. R. D'hooge, L. Cardon, *Prog. Mater. Sci.* **2020**, *114*, 100617.

[102] M. Amjadi, A. Pichitpajongkit, S. Lee, S. Ryu, I. Park, *ACS Nano* **2014**, *8*, 5154.

[103] C. Hu, Z. Li, Y. Wang, J. Gao, K. Dai, G. Zheng, C. Liu, C. Shen, H. Song, Z. Guo, *J. Mater. Chem. C* **2017**, *5*, 2318.

[104] H. Liu, Y. Li, K. Dai, G. Zheng, C. Liu, C. Shen, X. Yan, J. Guo, Z. Guo, *J. Mater. Chem. C* **2016**, *4*, 157.

[105] X. Cao, X. Wei, G. Li, C. Hu, K. Dai, J. Guo, G. Zheng, C. Liu, C. Shen, Z. Guo, *Polymer (Guildf).* **2017**, *112*, 1.

[106] C. S. Boland, *ACS Appl. Polym. Mater.* **2020**, *2*, 3474.

[107] J. Zhao, K. Dai, C. Liu, G. Zheng, B. Wang, C. Liu, J. Chen, C. Shen, *Compos. Part A Appl. Sci. Manuf.* **2013**, *48*, 129.

[108] A. D. Drozdov, A. Dorfmann, *Polym. Eng. Sci.* **2002**, *42*, 591.

[109] D. Ponnamma, K. K. Sadasivuni, M. Strankowski, P. Moldenaers, S. Thomas, Y. Grohens, *RSC Adv.* **2013**, *3*, 16068.

[110] S. Merabia, P. Sotta, D. R. Long, *Macromolecules* **2008**, *41*, 8252.

[111] L. Bokobza, *Polymers (Basel).* **2023**, *15*, DOI 10.3390/polym15132900.

[112] A. P. Kondratov, A. V Lozitskaya, V. N. Samokhin, A. A. Volinsky, *J. Polym. Res.* **2022**, *30*, 36.

[113] F. Bueche, *J. Appl. Polym. Sci.* **1960**, *4*, 107.

[114] L. Mullins, *Rubber Chem. Technol.* **1948**, *21*, 281.

[115] J. Diani, B. Fayolle, P. Gilormini, *Eur. Polym. J.* **2009**, *45*, 601.

[116] C. Zhang, P. Wang, C. Ma, G. Wu, M. Sumita, *Polymer (Guildf).* **2006**, *47*, 466.

[117] Z. Chai, A. Childress, A. A. Busnaina, *ACS Nano* **2022**, *16*, 17641.

[118] E. G. Kalinina, E. Y. Pikalova, *Russ. Chem. Rev.* **2019**, *88*, 1179.

[119] T. B. Jones, *Electromechanics of Particles*, Cambridge University Press, Cambridge, **1995**.

[120] O. D. Velev, K. H. Bhatt, *Soft Matter* **2006**, *2*, 738.

[121] J. Austin, D. Fernandes, M. J. A. Ruszala, N. Hill, J. Corbett, *Sci. Rep.* **2020**, *10*, 4628.

[122] M. Ammam, *RSC Adv.* **2012**, *2*, 7633.

[123] L. Chen, X. Liu, X. Zheng, X. Zhang, J. Yang, T. Tian, Y. Liao, *Micromachines* **2020**, *11*, DOI 10.3390/mi11070700.

[124] C. Yu, J. Vykoukal, D. M. Vykoukal, J. A. Schwartz, L. Shi, P. R. C. Gascoyne, *J. Microelectromechanical Syst.* **2005**, *14*, 480.

[125] S. Shabaniverki, J. J. Juárez, *Micromachines* **2021**, *12*, DOI 10.3390/mi12080935.

[126] P. Nazari, J. Zimmermann, C. Melzer, W. Kowalsky, J. Aghassi-Hagmann, G. Hernandez-Sosa, U. Lemmer, *Adv. Sens. Res.* **2024**, *n/a*, 2300189.

[127] M. A. U. Khalid, S. H. Chang, *Compos. Struct.* **2022**, *284*, 115214.

[128] S. Kwag, Y. Ko, J.-Y. Jeon, D. Jang, M. Park, Y. Choi, J. Cho, H. Kim, *J. Mater. Chem. C* **2023**, *11*, 3796.

[129] K. Zhai, H. Wang, Q. Ding, Z. Wu, M. Ding, K. Tao, B.-R. Yang, X. Xie, C. Li, J. Wu, *Adv. Sci.* **2023**, *10*, 2205632.

[130] H. Hwang, Y. Kim, J.-H. Park, U. Jeong, *Adv. Funct. Mater.* **2020**, *30*, 1908514.

[131] T. Huang, P. He, R. Wang, S. Yang, J. Sun, X. Xie, G. Ding, *Adv. Funct. Mater.* **2019**, *29*, 1903732.

[132] Y. Zheng, Q. Jin, W. Chen, Y. Sun, Z. Wang, *J. Mater. Chem. C* **2019**, *7*, 8423.

[133] X. Liu, X. Liang, Z. Lin, Z. Lei, Y. Xiong, Y. Hu, P. Zhu, R. Sun, C.-P. Wong, *ACS Appl. Mater. Interfaces* **2020**, *12*, 42420.

[134] B. Agoudjil, L. Ibos, J. C. Majesté, Y. Candau, Y. P. Mamunya, *Compos. Part A Appl. Sci. Manuf.* **2008**, *39*, 342.

[135] Q.-H. Zhang, D.-J. Chen, *J. Mater. Sci.* **2004**, *39*, 1751.

[136] A. Georgopoulou, F. Clemens, *ACS Appl. Electron. Mater.* **2020**, *2*, 1826.

[137] S. Biccai, C. S. Boland, D. P. O'Driscoll, A. Harvey, C. Gabbett, D. R.

O'Suilleabhain, A. J. Griffin, Z. Li, R. J. Young, J. N. Coleman, *ACS Nano* **2019**, *13*, 6845.

[138] H. Yang, X. Yao, Z. Zheng, L. Gong, L. Yuan, Y. Yuan, Y. Liu, *Compos. Sci. Technol.* **2018**, *167*, 371.

[139] G. Mariotti, L. Vannozzi, *Nanomaterials* **2019**, *9*, DOI 10.3390/nano9081182.

[140] C. S. Boland, *ACS Nano* **2019**, *13*, 13627.

[141] A. K. A. Aljarid, M. Dong, Y. Hu, C. Wei, J. P. Salvage, D. G. Papageorgiou, C. S. Boland, *Adv. Funct. Mater.* **2023**, *n/a*, 2303837.

[142] M. A. O'Mara, S. P. Ogilvie, M. J. Large, A. Amorim Graf, A. C. Sehnal, P. J. Lynch, J. P. Salvage, I. Jurewicz, A. A. K. King, A. B. Dalton, *Adv. Funct. Mater.* **2020**, *30*, 2002433.

[143] E. C. Sengezer, G. D. Seidel, R. J. Bodnar, *Smart Mater. Struct.* **2017**, *26*, 95027.

[144] Y.-T. Lai, Y.-M. Chen, Y.-J. J. Yang, *J. Microelectromechanical Syst.* **2012**, *21*, 217.

[145] M. S. Masraff, A. M. Noh Amin Abdul Rahman, M. R. Ramli, M. K. Mohd Jamil, M. K. Abdullah, M. Z. Ali, Z. Ahmad, *Compos. Sci. Technol.* **2021**, *203*, 108611.

[146] P. Liu, D. Gong, X. Cheng, T. Chen, D. Zhang, J. Cai, *ACS Appl. Mater. Interfaces* **2023**, *15*, 22485.

[147] T. Munekata, T. Suzuki, S. Yamakawa, R. Asahi, *Phys. Rev. E* **2013**, *88*, 52314.

[148] P. Nazari, R. Bäuerle, J. Zimmermann, C. Melzer, C. Schwab, A. Smith, W. Kowalsky, J. Aghassi-Hagmann, G. Hernandez-Sosa, U. Lemmer, *Adv. Mater.* **2023**, *35*, 2212189.

[149] Z. Liu, D. Qi, G. Hu, H. Wang, Y. Jiang, G. Chen, Y. Luo, X. J. Loh, B. Liedberg, X. Chen, *Adv. Mater.* **2018**, *30*, 1704229.

[150] S. Jang, J. Kim, D. W. Kim, J. W. Kim, S. Chun, H. J. Lee, G.-R. Yi, C. Pang, *ACS Appl. Mater. Interfaces* **2019**, *11*, 15079.

[151] M. M. Batista, R. Guirardello, M. A. Krähenbühl, *J. Am. Oil Chem. Soc.* **2015**, *92*, 95.

[152] T. Matsumoto, K. Nakamae, T. Ocjiumi, T. Tamura, T. Shioyama, *Bull. Inst. Chem. Res. Kyoto Univ.* **1974**, *52*, 403.

[153] D. R. Paul, *J. Appl. Polym. Sci.* **1968**, *12*, 383.

[154] Y. Wu, Y. Zhou, W. Asghar, Y. Liu, F. Li, D. Sun, C. Hu, Z. Wu, J. Shang, Z. Yu, R.-W. Li, H. Yang, *Adv. Intell. Syst.* **2021**, *3*, 2000235.

[155] L. Kou, T. Huang, B. Zheng, Y. Han, X. Zhao, K. Gopalsamy, H. Sun, C. Gao, *Nat. Commun.* **2014**, *5*, 3754.

[156] B. Fang, J. Yan, D. Chang, J. Piao, K. M. Ma, Q. Gu, P. Gao, Y. Chai, X. Tao, *Nat. Commun.* **2022**, *13*, 2101.

[157] J. Chen, C. Wang, X. Dong, H. Liu, *J. Polym. Res.* **2006**, *13*, 515.

[158] O. Mysiukiewicz, B. Gospodarek, P. Ławniczak, T. Sterzyński, *Adv. Polym. Technol.* **2018**, *37*, 3542.

[159] K. Wang, Q. Deng, *Polymers (Basel).* **2019**, *11*, DOI 10.3390/polym11061055.

[160] G. Acik, M. Kamaci, C. E. Cansoy, *Colloid Polym. Sci.* **2018**, *296*, 1759.

[161] J. Wang, X. Zhang, L. Jiang, J. Qiao, *Prog. Polym. Sci.* **2019**, *98*, 101160.

[162] C. S. Boland, U. Khan, G. Ryan, S. Barwich, R. Charifou, A. Harvey, C. Backes, Z. Li, M. S. Ferreira, M. E. Möbius, R. J. Young, J. N. Coleman, *Science* **2016**, *354*, 1257.

[163] C. S. Boland, *ACS Appl. Nano Mater.* **2020**, *3*, 11240.

[164] L. K. Willenberg, P. Dechent, G. Fuchs, D. U. Sauer, E. Figgemeier, *Sustainability* **2020**, *12*, 557.

[165] O. A. Araromi, M. A. Graule, K. L. Dorsey, S. Castellanos, J. R. Foster, W.-H. Hsu, A. E. Passy, J. J. Vlassak, J. C. Weaver, C. J. Walsh, R. J. Wood, *Nature* **2020**, *587*, 219.

[166] Y. Cheng, R. Wang, J. Sun, L. Gao, *Adv. Mater.* **2015**, *27*, 7365.

[167] H. Cho, S. Mayer, E. Pöselt, M. Susoff, P. J. in 't Veld, G. C. Rutledge, M. C. Boyce, *Polymer (Guildf).* **2017**, *128*, 87.

[168] C. S. Boland, U. Khan, M. Binions, S. Barwich, J. B. Boland, D. Weaire, J. N. Coleman, *Nanoscale* **2018**, *10*, 5366.

[169] S. Y. Kim, B. G. Choi, W. K. Baek, S. H. Park, S. W. Park, J. W. Shin, I. Kang, *Smart Mater. Struct.* **2019**, *28*, 35025.

[170] H. H. Chen, S. C. Fang, K. C. Aw, *Int. J. Biomechatronics Biomed. Robot.* **2010**, *1*, 88.

[171] A. J. Louli, L. D. Ellis, J. R. Dahn, *Joule* **2019**, *3*, 745.

[172] P. Mohtat, S. Lee, J. B. Siegel, A. G. Stefanopoulou, *J. Electrochem. Soc.* **2021**, *168*, 100520.

[173] C. P. Grey, J. M. Tarascon, *Nat. Mater.* **2016**, *16*, 45.

[174] P. Mohtat, S. Lee, J. B. Siegel, A. G. Stefanopoulou, *J. Power Sources* **2019**, *427*, 101.

[175] X. Yu, Z. Feng, Y. Ren, D. Henn, Z. Wu, K. An, B. Wu, C. Fau, C. Li, S. J. Harris, *J. Electrochem. Soc.* **2018**, *165*, A1578.

[176] J. Hemmerling, J. Guhathakurta, F. Dettinger, A. Fill, K. P. Birke, *Batteries* **2021**, *7*, DOI 10.3390/batteries7030061.

[177] P. K. Leung, C. Moreno, I. Masters, S. Hazra, B. Conde, M. R. Mohamed, R. J.

Dashwood, R. Bhagat, *J. Power Sources* **2014**, *271*, 82.

[178] J. Luo, C. Y. Dai, Z. Wang, K. Liu, W. G. Mao, D. N. Fang, X. Chen, *Measurement* **2016**, *94*, 759.

[179] A. Li, J. L. Hempel, M. P. Balogh, Y.-T. Cheng, A. I. Taub, *J. Electrochem. Soc.* **2023**, *170*, 10533.

[180] A. G. Hsieh, S. Bhadra, B. J. Hertzberg, P. J. Gjeltema, A. Goy, J. W. Fleischer, D. A. Steingart, *Energy Environ. Sci.* **2015**, *8*, 1569.

[181] P. Ladpli, F. Kopsaftopoulos, F.-K. Chang, *J. Power Sources* **2018**, *384*, 342.

[182] A. Ganguli, B. Saha, A. Raghavan, P. Kiesel, K. Arakaki, A. Schuh, J. Schwartz, A. Hegyi, L. W. Sommer, A. Lochbaum, S. Sahu, M. Alamgir, *J. Power Sources* **2017**, *341*, 474.

[183] J. Peng, X. Zhou, S. Jia, Y. Jin, S. Xu, J. Chen, *J. Power Sources* **2019**, *433*, 226692.

[184] L. Albero Blanquer, F. Marchini, J. R. Seitz, N. Daher, F. Bétermier, J. Huang, C. Gervillié, J.-M. Tarascon, *Nat. Commun.* **2022**, *13*, 1153.

[185] G. Han, J. Yan, Z. Guo, D. Greenwood, J. Marco, Y. Yu, *Renew. Sustain. Energy Rev.* **2021**, *150*, 111514.

[186] J. B. Siegel, A. G. Stefanopoulou, P. Hagans, Y. Ding, D. Gorsich, *J. Electrochem. Soc.* **2013**, *160*, A1031.

[187] X. M. Liu, C. B. Arnold, *J. Electrochem. Soc.* **2016**, *163*, A2501.

[188] J. Cannarella, C. B. Arnold, *J. Power Sources* **2014**, *269*, 7.

[189] A. J. Louli, J. Li, S. Trussler, C. R. Fell, J. R. Dahn, *J. Electrochem. Soc.* **2017**, *164*, A2689.

[190] S. L. Glazier, J. Li, A. J. Louli, J. P. Allen, J. R. Dahn, *J. Electrochem. Soc.* **2017**, *164*, A3545.

[191] K.-Y. Oh, B. I. Epureanu, *J. Power Sources* **2016**, *303*, 86.

[192] Y.-D. Su, Y. Preger, H. Burroughs, C. Sun, P. R. Ohodnicki, *Sensors* **2021**, *21*, DOI 10.3390/s21041397.

[193] K.-Y. Oh, J. B. Siegel, L. Secondo, S. U. Kim, N. A. Samad, J. Qin, D. Anderson, K. Garikipati, A. Knobloch, B. I. Epureanu, C. W. Monroe, A. Stefanopoulou, *J. Power Sources* **2014**, *267*, 197.

[194] P. Vorwerk, S.-K. Hahn, C. Daniel, U. Krause, K. Keutel, *Batteries* **2022**, *8*, DOI 10.3390/batteries8050042.

[195] B. Rieger, S. Schlueter, S. V Erhard, J. Schmalz, G. Reinhart, A. Jossen, *J. Energy Storage* **2016**, *6*, 213.

[196] X. Zhang, J. He, J. Zhou, H. Chen, W. Song, D. Fang, *Sci. China Technol. Sci.* **2021**, *64*, 83.

[197] X. Yang, M. Zhang, *Nanotechnol. Precis. Eng.* **2021**, *4*, 25001.

[198] H. Sun, X. Fang, Z. Fang, L. Zhao, B. Tian, P. Verma, R. Maeda, Z. Jiang, *Microsystems Nanoeng.* **2022**, *8*, 111.

[199] T. Yang, D. Xie, Z. Li, H. Zhu, *Mater. Sci. Eng. R Reports* **2017**, *115*, 1.

[200] Z. Shen, Z. Zhang, N. Zhang, J. Li, P. Zhou, F. Hu, Y. Rong, B. Lu, G. Gu, *Adv. Mater.* **2022**, *34*, 2203650.

[201] X. A. Nguyen, S. Gong, W. Cheng, S. Chauhan, *IEEE Sens. J.* **2021**, *21*, 15269.

[202] X. Qu, Y. Wu, P. Ji, B. Wang, Q. Liang, Z. Han, J. Li, Z. Wu, S. Chen, G. Zhang, H. Wang, *ACS Appl. Mater. Interfaces* **2022**, *14*, 29167.

[203] Q. Li, T. Wu, W. Zhao, J. Ji, G. Wang, *ACS Appl. Mater. Interfaces* **2021**, *13*, 37433.

[204] S. Gong, D. T. H. Lai, B. Su, K. J. Si, Z. Ma, L. W. Yap, P. Guo, W. Cheng, *Adv. Electron. Mater.* **2015**, *1*, 1400063.

[205] D. Kim, A. Chhetry, M. A. Zahed, S. Sharma, S. Jeong, H. Song, J. Y. Park, *ACS Appl. Mater. Interfaces* **2023**, *15*, 1475.

[206] R. Texidó, G. Nieva-Esteve, J. Gilabert-Porres, G. Reyes, S. Borrós, *Adv. Electron. Mater.* **2023**, *9*, 2200717.

[207] D. Yao, L. Wu, S. Peng, X. Gao, C. Lu, Z. Yu, X. Wang, C. Li, Y. He, *ACS Appl. Mater. Interfaces* **2021**, *13*, 11284.

[208] J. Wang, J. Lin, K. Pan, K. Zhang, H. Zhang, J. Dong, D. Hu, Z. Jia, J. Luo, *Chem. Eng. J.* **2023**, *477*, 146759.

[209] J. Pan, B. Hao, W. Song, S. Chen, D. Li, L. Luo, Z. Xia, D. Cheng, A. Xu, G. Cai, X. Wang, *Compos. Part B Eng.* **2020**, *183*, 107683.

[210] X. Wu, H. Chen, X. Luo, D. Wang, P. Schaaf, G. Zhang, *Adv. Mater. Technol.* **2021**, *6*, 2100524.

[211] C. Farcau, N. M. Sangeetha, H. Moreira, B. Viallet, J. Grisolia, D. Ciuculescu-Pradines, L. Ressier, *ACS Nano* **2011**, *5*, 7137.

[212] Y. Chen, Y. Zhang, F. Song, H. Zhang, Q. Zhang, J. Xu, H. Wang, F. Ke, *Adv. Mater. Technol.* **2021**, *6*, 2100421.

[213] J. Guo, B. Zhou, R. Zong, L. Pan, X. Li, X. Yu, C. Yang, L. Kong, Q. Dai, *ACS Appl. Mater. Interfaces* **2019**, *11*, 33589.

[214] Y. R. Jeong, H. Park, S. W. Jin, S. Y. Hong, S.-S. Lee, J. S. Ha, *Adv. Funct. Mater.* **2015**, *25*, 4228.

[215] W. Zhong, C. Liu, C. Xiang, Y. Jin, M. Li, K. Liu, Q. Liu, Y. Wang, G. Sun, D. Wang, *ACS Appl. Mater. Interfaces* **2017**, *9*, 42058.

[216] M. B. Coskun, A. Akbari, D. T. H. Lai, A. Neild, M. Majumder, T. Alan, *ACS Appl. Mater. Interfaces* **2016**, *8*, 22501.

[217] F. Wang, J. Chen, X. Cui, X. Liu, X. Chang, Y. Zhu, *ACS Appl. Mater. Interfaces* **2022**, *14*, 30268.

[218] Q. Yu, R. Ge, J. Wen, T. Du, J. Zhai, S. Liu, L. Wang, Y. Qin, *Nat. Commun.* **2022**, *13*, 778.

[219] M. Zhang, C. Wang, H. Wang, M. Jian, X. Hao, Y. Zhang, *Adv. Funct. Mater.* **2017**, *27*, 1604795.

[220] T. He, C. Lin, L. Shi, R. Wang, J. Sun, *ACS Appl. Mater. Interfaces* **2018**, *10*, 9653.

Acknowledgments

This thesis and the research it embodies owe their existence to many individuals, particularly the scientists who taught me the craft of material science, guided my thought processes, and patiently entertained my myriad questions with great generosity.

My deepest appreciation goes to the exceptional Prof. Dr. Uli Lemmer, my supervisor and mentor, whose inspiration and unwavering support sustained me throughout the transformative and arduous journey of my PhD. His mentorship transcends the academic realm, profoundly influencing the skills I have acquired through the invaluable experience of being his student.

I extend my sincere gratitude to Prof. Dr. Gerardo Hernandez-Sosa for his invaluable mentorship and friendly support during challenging times. His contributions to discussions on the results of this work, as well as his careful revision and proofreading of the microfiber works, are deeply appreciated.

I am also exceedingly grateful to Prof. Dr. Jasmin Aghassi-Hagmann for her resolute support and encouragement from the day one. Her insightful guidance not only enriched deep research and scientific discussions but also provided abundant motivation helping me navigate difficult moments.

Additionally, I would also like to thank Prof. Dr. Wolfgang Kowalski for offering me the opportunity to pursue this PhD position at InnovationLab and for his ongoing encouragement.

The research presented in this thesis was conducted within the laboratories of InnovationLab GmbH in Heidelberg, home to the Printed Electronics research group led by Prof. Dr. Gerardo Hernandez-Sosa, as a part of the Light Technology Institute (at KIT). I consider myself fortunate and deeply grateful for the opportunity to collaborate at InnovationLab (iL) alongside remarkable colleagues and partners, who made my PhD journey exciting. I wish to extend my heartfelt gratitude to Dr. Christian Melzer and Dr. Johannes Zimmermann for their insightful scientific exchanges during the 2HORISONS project, and for their constant motivation and support throughout the highs and lows of my PhD journey.

Special appreciation goes to Rainer Bäuerle, a friend and a colleague without whose humor and support my entire PhD journey would have not been so joyful. I am also grateful to my

multi-lingual officemate and friend, Nassima Amroun, whose companionship during lunch breaks at iL enriched our discussions with wisdom, shared stories of life, cuisine, and culture. I wish to express my sincere thanks to Palak Gupta and Irene Brunetti, my dear friends and colleagues at iL, whose priceless support helped me extensively, especially during the writing process of this thesis in Chemnitz. Their companionship, immense motivation, and humor, and abundant contribution to this work are deeply appreciated and will always be cherished.

I hold fond memories of my time at iL, appreciating not only the knowledge gained from my esteemed colleagues but also the joyful moments fostered by the warm and friendly atmosphere. I am deeply grateful to Christian Willig, who offered his support right from the start. I extend my sincere gratitude to Thomas Rohland, Yannick Kraft, and Benjamin Obermayer for teaching me their expertise in screen-printing, ink-jet printing, and laser-cutting techniques. I am also indebted to Kevin Schmid for his steadfast support in the Electronics Lab, and to Alexey Sizov for patiently guiding me in working with Alluris. All of these individuals were always willing to address my endless stream of questions and supported me throughout my time there. I extend my sincere gratitude to Karl-Philipp Strunk and to Jean-Nicolas Tisserant for their willingness to engage in fruitful scientific discussions.

A special thanks to all my colleagues with whom I shared countless coffee/tea breaks and received unconditional support and invaluable guidance: Kai Xia, Roja Singh, Ozan Karakaya, Atefeh Amin, Peter Krebsbach, Mervin Arne Seiberlich, Manuel Pietsch, Christian Rainer, Luis Ruiz Preciado, Ali Tunc, Manuel Seifert, Surya Abhishek, and Xiaokun Huang.

I would like to express my gratitude to Jagadeesha Yogheesha, whom I supervised during his master's thesis, for the valuable lessons learned through guiding his research.

I am deeply thankful to my friends who have consistently supported my well-being through their presence: Taba, Nasrin, Mohamad, Saba, Sara, Ali, Amir, Mahsa, Shahrzad, Shahab, Shirin, Zahra, Klaudija, Qiaushuang, and Isabel.

I also wish to thank the external collaboration partners, Dr. Anna Smith, Christopher Schwab, and Steffen Jokisch for their solid collaboration and support on the Li-ion battery experiments. Our collaboration has significantly enriched my research.

I am deeply grateful for the multitude of invaluable scientific, professional, and personal development opportunities provided by the Karlsruhe Institute of Technology (KIT), the Karlsruhe House of Young Scientists (KHYS), the Karlsruhe School of Optics and Photonics (KSOP), and the 3D Matter Made to Order Excellence Cluster (3DMM2O). I extend sincere appreciation for the financial support and funding that made this work possible, including support from the "2HORISONS" project (03INT606) by the Federal Ministry of Education and Research (BMBF), as well as the support Uli patiently provided.

Special thanks are due to Nicole Klöfer, whose wonderful support and intelligence, along with her patience in managing last-minute paperwork at LTI were invaluable. Gratitude is also extended to Karsten Bensch and Thomas Peissig, whose efforts facilitated seamless work within the cleanrooms of iL.

I would like to thank the referees Prof. Uli Lemmer, Prof. Dr. Jasmin Aghassi-Hagmann for reviewing this thesis.

My deepest appreciation goes to Bahram. My husband, my mentor, and the cornerstone of all my achievements. As a scientist, he taught me priceless lessons on how to figure out answers to complex scientific problems, conducting cutting-edge research, and fostering innovation and ambition. I am infinitely grateful for his unparalleled support and visionary guidance, which have profoundly shaped my past, present, and future endeavors. His unconditional love and unwavering belief and confidence in me have have been my guiding light, empowering me to embrace my own potential.

والدین عزیزم که همیشه با عشق، درایت، و دعاهایشان، پشتیبان من بوده‌اند، باعث شده‌اند که همواره احساس بینهایت خوشبختی، شادی و قدردانی داشته باشم. واژه‌ها کافی نیستند تا ارزش این حمایت‌ها و این همراهی‌های گرانبها را بیان کنند. از مادرم، سرنوش کوهی، و پدرم، حمیدرضا نظری، که زندگی خود را به رشد و پیشرفت من اختصاص داده اند، صمیمانه قدردانی می کنم. همچنین، از خواهر عزیزم، پریسا، بخاطر رفاقت بی‌قیاس و و حمایت همیشگی‌اش تا ابد سپاس گزارم.

Lastly, I am grateful to all the individuals who, with every word they taught me, contributed to the person I am today.